

MSc Thesis

Modelling of Vortex Generators
within the Integral Boundary-
Layer Theory

Delphine De Tavernier

MSc Thesis

Modelling of Vortex Generators within the Integral Boundary-Layer Theory

by

Delphine De Tavernier

to obtain the degree of Master of Science in Aerospace Engineering
at the Delft University of Technology,
to be defended publicly on Thursday November 17, 2016 at 10:30 AM.

Student number: 4175719
Project duration: January 18, 2016 – November 17, 2016
Thesis committee: Dr. ir. C. Simao Ferreira, TU Delft, supervisor
Ir. D. Baldacchino, TU Delft, supervisor
Prof. Dr. ir. F. Scarano, TU Delft
Dr. ir. B. van Oudheusden, TU Delft

This thesis is confidential and cannot be made public until July 1, 2017.

Acknowledgement

This master thesis is the final work in order to obtain my master of science in Aerospace Engineering. I would like to express my gratitude to everyone who supported me throughout this project. Without them, the realisation of this project would not have been possible and therefore I would like to thank them all.

First of all, I want to thank Daniel Baldacchino. His enthusiasm, faith and positiveness have been extremely helpful. He was always available for my questions and gave generously of his time and knowledge to guide me through this project. His supervision and critical mindset helped me to strive for the best results possible. I could not have imagined to have a better supervisor for my master thesis.

Secondly, I am also very grateful to Dr. Carlos Simao Ferreira. He always knew where to look for the right answers in challenging situations and guided me to new insights, sources and theories. His support and tutorship brought a new perspective into my master thesis research. I also want to thank him for the valuable discussions and sharing his passion for scientific research.

My sincere thanks also goes to the university and the people who provided me with reference data of airfoils equipped with vortex generators. W.A. Timmer, M. Manolesos and the team behind the AVATAR project, allowed me to use their data. Without their generosity, this project would not have been possible.

Further, special appreciation goes to my parents and boyfriend for their support and unconditional encouragements. To my parents, I cannot express how grateful I am for all chances you gave me. Your loving care helped me through challenging phases of my education and you continuously inspired me to strive towards my goals. To my boyfriend, I want to thank you to always stand by my side and be there at all times. You supported me from day one through this adventure. Thank you for the patience you had and the joy and love you bring into my life.

I would also like to thank my friends. Together we shared unforgettable moments that I will carry in my heart forever. You were able to bring a laugh on my face in difficult times and were always open for a discussion no matter what the topic was. My time at university would not have been the same without you. I hope our friendships will last forever.

Finally, I want to thank all my former teachers and professors, to have challenged me to reach a higher level. They taught me valuable knowledge and also encouraged me to develop myself personally. They learned me to never give up and that with hard work, your dreams can come true.

Delft, November 2016

Delphine De Tavernier

Executive Summary

One of the most commonly used flow control techniques to trim the aerodynamic performance of wind turbine blades are vortex generators. This passive device, which does not require any active energy, is gaining an increasing interest in this sector especially due to the trend of increasing wind turbine size.

Vortex generators are a flow control technique used to prevent or at least lessen the severity of flow separation. The streamwise vortices shed at the free tips of the vortex generators increase the mixing between the high-energy flow in the outer part of the boundary-layer with the low energy regions near the walls. The shed vortices are defined by the strength of the vortices just downstream of the device, the streamwise decay of the vortex strength and the vortex trajectory. In order to assess and optimise the use of vortex generators, there is a need to accurately model the effect of this device in a cost and time efficient way. This could be achieved by modelling vortex generators using integral boundary-layer codes.

XFOIL and RFOIL are two well-known integral boundary-layer codes. These two codes rely on Prandtl's theory stating that a flow field around an object can be divided into two areas: the inviscid outer flow and the viscous inner flow. The inviscid part of the flow is solved using a streamfunction panel method while the viscous boundary-layer solution is prescribed by the boundary-layer equations and additional closure relations. Both solutions are strongly interconnected to each other.

A suitable methodology to model the effect of vortex generators into integral boundary-layer codes is the source term approach. This approach was already initiated by Kerho and Kramer¹ but is revised carefully in this thesis. The introduction of the streamwise vortices results in an increase in dissipation. To simulate this, the shear-lag equation is modified by introducing an additional source term to the equilibrium shear stress coefficient. The strength of this additional source term is varied over the chord to mimic the downstream decay of the shed vortex circulation. Implementing the source term into XFOIL and RFOIL allows to capture the expected effect of vortex generators on the boundary-layer properties.

The source term shape function is prescribed by three parameters: the source term strength, the decay rate and the location of the vortex generators. Because the source term depends on the vortex generator geometry and the local flow properties, its value is calibrated for different airfoil/vortex generator configurations using reference data. Afterwards, these calibrated source terms are related back to the vortex generator parameters and local boundary-layer properties to establish an empirical relation for the source term integral. To do so, a multiple variable linear regression is applied in which the independent variables are the vortex generator height, vortex generator length, inflow angle, local boundary-layer momentum thickness and edge velocity. The source term empirical relation is implemented in XFOIL and RFOIL.

Implementing the source term empirical relation led to the development of the foundations of the design tools XFOILVG and RFOILVG. These two codes are extensively validated to evaluate the performance and identify code limitations. Validating the source term empirical relation and its implementation, is realised by comparing the codes' predictions with reference data from the data base that was already used to set up the source term relation. To further validate the robustness and generality of the code with respect to airfoil selection and Reynolds number, external data sets adopted from literature are used. Based on the validation results, it is believed that the source term approach to model vortex generators within the integral boundary-layer theory is very promising. To further elaborate on this method, recommendations for further work are made. These recommendations concern the data base used to set up the source term empirical relation, the effect of vortex generators on the friction coefficient and the role and value of adding a transition model.

Contents

Contents

List of Figures

List of Tables

List of Symbols

Chapter 1 Introduction

1.1 Thesis Objective	1
1.2 Methods & Approach	1

Chapter 2 Vortex Generators

2.1 Flow Control Techniques	5
2.1.1 Historical Background	5
2.1.2 Definition	6
2.1.3 The Need for Flow Control	6
2.2 Working Principle of Vortex Generators	7
2.3 Configuration of Vortex Generators	8
2.4 Vortex Characteristics	9
2.4.1 Initial Vortex Strength.	9
2.4.2 Vortex Decay	10
2.4.3 Vortex Trajectory	11
2.4.4 Three-Dimensional Flowfield.	12

Chapter 3 Modelling Techniques for Vortex Generators

3.1 Modelling Techniques Using CFD	15
3.1.1 Fully Resolved CFD	15
3.1.2 BAY Model	15
3.1.3 jBAY Model	16
3.1.4 Vortex-Source Model.	16
3.1.5 Statistical Method.	16
3.1.6 Smith's Method	17
3.2 Modelling Techniques Using Integral Boundary-Layer Theory	17
3.3 Research Gap	19

Chapter 4 Boundary-Layer Theory

4.1 Boundary-Layer Concept.	21
4.2 Boundary-Layer Parameters	22
4.2.1 Definitions of Boundary-Layer Parameters	22
4.2.2 Blasius Solution for Flat-Plate Flow	24
4.2.3 Dissipation Coefficient	25
4.3 Boundary-Layer Equations.	26
4.3.1 Laminar Boundary-Layer Equations	27
4.3.2 Turbulent Boundary-Layer Equations	28

4.4	Boundary-Layer Codes	29
4.4.1	Inviscid Solution	29
4.4.2	Viscid Solution	29
4.4.3	Viscid/Inviscid Coupling	31
4.4.4	Xfoil and Rfoil	32
Chapter 5 Modifications to the Boundary-Layer Formulation		
5.1	Source Term Approach	35
5.2	Source Term Implementation	36
5.3	Source Term Shape Function	36
5.4	Laminar-Turbulent Transition	37
5.5	Verification of the Code Modifications	38
5.5.1	Expected Effect on the Boundary-Layer Properties.	38
5.5.2	Verification Xfoil.	39
5.5.3	Verification Rfoil	42
Chapter 6 Experimental and Numerical Reference Data		
6.1	Experimental Set-Up & Equipment	45
6.1.1	Wind Tunnel.	45
6.1.2	Airfoil Model.	46
6.1.3	Vortex Generators	46
6.1.4	Zig-Zag Tape	47
6.1.5	Pressure Measurement	47
6.1.6	Testing Procedure	47
6.1.7	Set-up Pictures	47
6.2	Experimental Results & Discussion	48
6.2.1	Height of the Vortex Generators	48
6.2.2	Chordwise Position of the Vortex Generators	49
6.2.3	Inflow Angle of the Vortex Generators.	49
6.2.4	Leading Edge Forced Transition	50
6.2.5	Three-Dimensional Flowfield.	51
6.3	Additional Reference Data	52
Chapter 7 Source Term Empirical Relation		
7.1	Source Term Calibration Process	53
7.1.1	Optimisation Approach	53
7.1.2	Target Lift Polar	56
7.1.3	Optimal Source Term.	57
7.1.4	Summary of the Calibration Process	58
7.2	Source Term Regression.	58
7.2.1	Multiple Variable Linear Regression Approach	59
7.2.2	Source Term Linear Regression	60
7.2.3	Results Source Term Regression	61
7.2.4	Discussion on Source Term Regression.	62
7.3	Implementation of the Source Term Empirical Relation	64
Chapter 8 Validation		
8.1	First Validation: Source Term Relation	67
8.1.1	LTT Data Set	67
8.1.2	AVATAR Data Set.	70
8.1.3	TUD Data Set.	75
8.2	Second Validation: Code Robustness.	78
8.2.1	Pechlivanoglou Data Set	78
8.2.2	Madani Data Set	80
8.3	Evaluation & Limitations	84

Chapter 9 Recommendations & Further Work

9.1 Enlarge Data Base	87
9.2 Friction Coefficient	87
9.3 Laminar-Turbulent Transition Model	88

Chapter 10 Conclusion

10.1 Part 1: Introduction	91
10.2 Part 2: Methodology	91
10.3 Part 3: Results	92
10.4 Part 4: Discussion	93

Appendix A Reference Data Base

A.1 Wind Tunnel Experiment (Experimental data).	95
A.2 TUD (experimental data).	95
A.3 AVATAR (CFD numerical data).	96
A.4 NTUA (experimental data)	96

Appendix B Influence Closure Relations on Source Term

Appendix C Clean Airfoil Modelling

C.1 DU97W300 Airfoil.	99
C.2 DU91W2250 Airfoil	100
C.3 DU93W210 Airfoil.	100
C.4 DU331 Airfoil	101
C.5 FFAW3333 Airfoil	101

Appendix D Validation Cases

Appendix E Modifications to the Xfoil Code

E.1 Subroutine VPAR	105
E.2 Subroutine MRCHDU	107
E.3 Subroutine BLVAR	109

Bibliography

List of Figures

1.1	Thesis outline.	3
2.1	Singular separation. ²	7
2.2	Ordinary separation. ²	7
2.3	Use of vortex generators to delay separation. ³	7
2.4	C_l vs C_d at a Reynolds number of 235000. Comparison of different vortex generator configurations and a glass bead transition strip. Separation bubbles are present in the clean airfoil case. ⁴	8
2.5	Different vortex generator configurations. ⁵	9
2.6	Generalised correlation of vortex strength against Reynolds number based on device effective height. ²	10
2.7	Vortex trajectory single vortex generator vane. ²	11
2.8	Projection of the the vortex trajectory in the frontal plane for counter-rotating vortex generator vane. ⁶	11
2.9	Projection of the the vortex trajectory in the frontal plane for co-rotating vortex generator vane. ⁶	12
2.10	Controlled (grey) and baseline (black) streamwise velocity profiles at different spanwise locations behind the VG pair. ⁷	12
3.1	Cell selection of BAY model. ⁸	16
3.2	Cell selection of jBAY model. ⁸	16
3.3	Comparison of modified XFOIL and experimental lift curve results for the EID75SR section with co-rotating 0.5δ VGs at $x/c = 0.75$, $Re = 0.7 \times 10^6$. ¹	18
3.4	Comparison of modified XFOIL and experimental lift-drag curve results for the EID75SR section with co-rotating 0.5δ VGs at $x/c = 0.75$, $Re = 0.7 \times 10^6$. ¹	18
3.5	Comparison of modified XFOIL and experimental pressure distribution results for the baseline NLF(1)-1015 and EID75SR section with and without co-rotating 0.5δ VGs at $x/c = 0.75$, $Re = 0.7 \times 10^6$. ¹	18
4.1	Boundary-layer concept. ⁹	22
4.2	Boundary-layer thickness. ⁹	23
4.3	Displacement thickness. ⁹	23
4.4	Shape factor. ¹⁰	23
4.5	Blasius velocity profile. ¹¹	24
4.6	Dissipation coefficient for self-similar flows. ¹²	26
4.7	Airfoil and wake panelling with vorticity and source distributions, with trailing edge detail. ¹³	29
4.8	Diagram viscid-inviscid interaction.	31
5.1	Source term with $\lambda = 20.0$, $x_{vg} = 0.3$ and varying strength	37
5.2	Source term with $\sigma_0 = 1.0$, $x_{vg} = 0.3$ and varying decay	37
5.3	Effect of vortex generators on boundary-layer properties. ¹	38
5.4	Source term versus chordwise position with $x_{vg} = 40\%$. Case 1: $\sigma_0 = 0.00$, $\lambda = 150.0$, Case 2: $\sigma_0 = 0.05$, $\lambda = 150.0$, Case 3: $\sigma_0 = 0.10$, $\lambda = 150.0$	39
5.5	Boundary-layer properties versus chordwise position for the DU93W200 airfoil at $\alpha = 5^\circ$ and $Re = 1E6$ with $x_{vg} = 40\%$ using XFOIL. Case 1: $\sigma_0 = 0.00$, $\lambda = 150.0$, Case 2: $\sigma_0 = 0.05$, $\lambda = 150.0$, Case 3: $\sigma_0 = 0.10$, $\lambda = 150.0$	40
5.6	Boundary-layer properties versus chordwise position for the DU93W200 airfoil at $\alpha = 11^\circ$ and $Re = 1E6$ with $x_{vg} = 40\%$ using XFOIL. Case 1: $\sigma_0 = 0.00$, $\lambda = 150.0$, Case 2: $\sigma_0 = 0.05$, $\lambda = 150.0$, Case 3: $\sigma_0 = 0.10$, $\lambda = 150.0$	40
5.7	Dissipation coefficient versus chordwise position for the DU93W200 airfoil at $\alpha = 5^\circ$ and $Re = 1E6$ with $x_{vg} = 40\%$. Case 1: $\sigma_0 = 0.00$, $\lambda = 150.0$, Case 2: $\sigma_0 = 0.05$, $\lambda = 150.0$, Case 3: $\sigma_0 = 0.10$, $\lambda = 150.0$	41

5.8	Dissipation coefficient versus chordwise position for the DU93W200 airfoil at $\alpha = 11^\circ$ and $Re = 1E6$ with $x_{vg} = 40\%$. Case 1: $\sigma_0 = 0.00$, $\lambda = 150.0$, Case 2: $\sigma_0 = 0.05$, $\lambda = 150.0$, Case 3: $\sigma_0 = 0.10$, $\lambda = 150.0$	41
5.9	Lift polar of the DU93W200 airfoil at $Re = 1E6$ with $x_{vg} = 40\%$. Case 1: $\sigma_0 = 0.00$, $\lambda = 150.0$, Case 2: $\sigma_0 = 0.05$, $\lambda = 150.0$, Case 3: $\sigma_0 = 0.10$, $\lambda = 150.0$	41
5.10	Drag polar of the DU93W200 airfoil at $Re = 1E6$ with $x_{vg} = 40\%$. Case 1: $\sigma_0 = 0.00$, $\lambda = 150.0$, Case 2: $\sigma_0 = 0.05$, $\lambda = 150.0$, Case 3: $\sigma_0 = 0.10$, $\lambda = 150.0$	41
5.11	Boundary-layer properties versus chordwise position for the DU93W200 airfoil at $\alpha = 5^\circ$ and $Re = 1E6$ with $x_{vg} = 40\%$ using RFOIL. Case 1: $\sigma_0 = 0.00$, $\lambda = 150.0$, Case 2: $\sigma_0 = 0.05$, $\lambda = 150.0$, Case 3: $\sigma_0 = 0.10$, $\lambda = 150.0$	42
5.12	Boundary-layer properties versus chordwise position for the DU93W200 airfoil at $\alpha = 11^\circ$ and $Re = 1E6$ with $x_{vg} = 40\%$ using RFOIL. Case 1: $\sigma_0 = 0.00$, $\lambda = 150.0$, Case 2: $\sigma_0 = 0.05$, $\lambda = 150.0$, Case 3: $\sigma_0 = 0.10$, $\lambda = 150.0$	42
5.13	Lift polar of the DU93W200 airfoil at $Re = 1E6$ with $x_{vg} = 40\%$. Case 1: $\sigma_0 = 0.00$, $\lambda = 150.0$, Case 2: $\sigma_0 = 0.05$, $\lambda = 150.0$, Case 3: $\sigma_0 = 0.10$, $\lambda = 150.0$	43
5.14	Drag polar of the DU93W200 airfoil at $Re = 1E6$ with $x_{vg} = 40\%$. Case 1: $\sigma_0 = 0.00$, $\lambda = 150.0$, Case 2: $\sigma_0 = 0.05$, $\lambda = 150.0$, Case 3: $\sigma_0 = 0.10$, $\lambda = 150.0$	43
6.1	Schematic representation of the Low Speed Low Turbulence wind tunnel ¹⁴	45
6.2	Cross section of the DU97W300 airfoil	46
6.3	Schematic of the vortex generators	47
6.4	Schematic of the zig-zag tape	47
6.5	Airfoil model within the wind tunnel section, wake rake visible in background	48
6.6	Strip of vortex generators with different configurations	48
6.7	Details of vortex generator strip	48
6.8	Vortex generators installed on airfoil model	48
6.9	Lift polar of the DU97W300 airfoil at $Re = 2E6$ with $x_{vg}/c = 0.4$, $\beta = 15^\circ$ and varying height	49
6.10	Drag polar of the DU97W300 airfoil at $Re = 2E6$ with $x_{vg}/c = 0.4$, $\beta = 15^\circ$ and varying height	49
6.11	Lift polar of the DU97W300 airfoil at $Re = 2E6$ with $h = 5\text{mm}$, $\beta = 15^\circ$ and varying position	49
6.12	Drag polar of the DU97W300 airfoil at $Re = 2E6$ with $h = 5\text{mm}$, $\beta = 15^\circ$ and varying position	49
6.13	Lift polar of the DU97W300 airfoil at $Re = 2E6$ with $h = 5\text{mm}$, $x_{vg}/c = 0.2$ and varying inflow angle	50
6.14	Drag polar of the DU97W300 airfoil at $Re = 2E6$ with $h = 5\text{mm}$, $x_{vg}/c = 0.2$, and varying inflow angle	50
6.15	Lift polar of the DU97W300 airfoil at $Re = 2E6$ with $h = 5$ and 10mm , $\beta = 15^\circ$, $x_{vg}/c = 0.4$ with free and forced transition	50
6.16	Drag polar of the DU97W300 airfoil at $Re = 2E6$ with $h = 5$ and 10mm , $\beta = 15^\circ$, $x_{vg}/c = 0.4$ with free and forced transition	50
6.17	Flow visualisation of the DU97W300 airfoil equipped with vortex generators at $Re = 2E6$ and $\alpha = 0^\circ$	51
6.18	Spanwise Pattern of the drag coefficient of the DU97W300 airfoil at $Re = 2E6$ with $h = 5\text{mm}$, $x_{vg}/c = 0.2$ and $\beta = 5^\circ$	51
7.1	Variation of lift coefficient for a range of strength and decay values.	54
7.2	Variation of drag coefficient for a range of strength and decay values.	54
7.3	Variation of the lift coefficient with the source term integral.	55
7.4	Variation of the drag coefficient with the source term integral.	55
7.5	Lift polar of a clean DU97W300 at $Re = 2.0E6$ calculated using XFOIL and measurement data and the measurement data of the vortex generator case.	56
7.6	Lift polar of the DU97W300 at $Re = 2.0E6$ with and without vortex generators as well as the introduction of the target lift polar.	57
7.7	Identification optimal source term.	58
7.8	Illustration of the brute-force solution of the source term problem.	58
7.9	The use of a weight matrix in a linear regression approach.	60
7.10	Range of interested angles of attack	61
7.11	Xfoil goodness of fit of source term regression line.	62
7.12	Xfoil error distribution between optimal source term and empirical source term.	62
7.13	Rfoil goodness of fit of source term regression line.	62
7.14	Rfoil error distribution between optimal source term and empirical source term.	62
7.15	Flow chart source term implementation.	65

8.1	Lift polar of the DU97W300 airfoil at $Re = 2E6$ with $h = 10\text{mm}$, $l = 30\text{mm}$, $\beta = 15^\circ$ and varying position originating from measurements, XFOIL and RFOIL	68
8.2	Drag polar of the DU97W300 airfoil at $Re = 2E6$ with $h = 10\text{mm}$, $l = 30\text{mm}$, $\beta = 15^\circ$ and varying position originating from measurements, XFOIL and RFOIL	68
8.3	Lift polar of the DU97W300 airfoil at $Re = 2E6$ with $l = 3h\text{mm}$, $\beta = 15^\circ$, $x_{vg}/c = 0.4$ and varying height originating from measurements, XFOIL and RFOIL	69
8.4	Drag polar of the DU97W300 airfoil at $Re = 2E6$ with $l = 3h\text{mm}$, $\beta = 15^\circ$, $x_{vg}/c = 0.4$ and varying height originating from measurements, XFOIL and RFOIL	69
8.5	Cross-section of the DU331 airfoil.	70
8.6	Cross-section of the FFAW3333 airfoil.	70
8.7	Lift polar of the DU331 airfoil at $Re = 15.8E6$ with $l = 3h\text{mm}$, $\beta = 20^\circ$, $x_{vg}/c = 0.4$ and varying height originating from measurements, XFOIL and RFOIL	71
8.8	Drag polar of the DU331 airfoil at $Re = 15.8E6$ with $l = 3h\text{mm}$, $\beta = 20^\circ$, $x_{vg}/c = 0.4$ and varying height originating from measurements, XFOIL and RFOIL	71
8.9	Lift polar of the FFAW3333 airfoil at $Re = 14.0E6$ with $l = 3h\text{mm}$, $\beta = 20^\circ$, $x_{vg}/c = 0.4$ and varying height originating from measurements, XFOIL and RFOIL	72
8.10	Drag polar of the FFAW3333 airfoil at $Re = 14.0E6$ with $l = 3h\text{mm}$, $\beta = 20^\circ$, $x_{vg}/c = 0.4$ and varying height originating from measurements, XFOIL and RFOIL	72
8.11	Lift polar of the DU331 airfoil at $Re = 15.8E6$ with $h = 10\text{mm}$, $l = 30\text{mm}$, $x_{vg}/c = 0.4$ and varying inflow angle originating from measurements, XFOIL and RFOIL	73
8.12	Drag polar of the DU331 airfoil at $Re = 15.8E6$ with $h = 10\text{mm}$, $l = 30\text{mm}$, $x_{vg}/c = 0.4$ and varying inflow angle originating from measurements, XFOIL and RFOIL	73
8.13	Lift polar of the FFAW3333 airfoil at $Re = 14.0E6$ with $h = 10\text{mm}$, $l = 30\text{mm}$, $x_{vg}/c = 0.4$ and varying inflow angle originating from measurements, XFOIL and RFOIL	74
8.14	Drag polar of the FFAW3333 airfoil at $Re = 14.0E6$ with $h = 10\text{mm}$, $l = 30\text{mm}$, $x_{vg}/c = 0.4$ and varying inflow angle originating from measurements, XFOIL and RFOIL	74
8.15	Cross-section of the DU91W2250 airfoil.	75
8.16	Cross-section of the DU93W210 airfoil.	75
8.17	Lift polar of the DU91W2250 airfoil at $Re = 2E6$ with $h = 5\text{mm}$, $l = 17\text{mm}$, $\beta = 16.4^\circ$ and varying position originating from measurements, XFOIL and RFOIL	76
8.18	Drag polar of the DU91W2250 airfoil at $Re = 2E6$ with $h = 5\text{mm}$, $l = 17\text{mm}$, $\beta = 16.4^\circ$ and varying position originating from measurements, XFOIL and RFOIL	76
8.19	Lift polar of the DU93W210 airfoil at $Re = 1E6$ with $h = 5\text{mm}$, $l = 17\text{mm}$, $\beta = 16.4^\circ$ and varying position originating from measurements, XFOIL and RFOIL	77
8.20	Drag polar of the DU93W210 airfoil at $Re = 1E6$ with $h = 5\text{mm}$, $l = 17\text{mm}$, $\beta = 16.4^\circ$ and varying position originating from measurements, XFOIL and RFOIL	77
8.21	Cross-section of the AH93W174 airfoil.	78
8.22	Lift polar of the AH93W174 airfoil at $Re = 1.3E6$ with $h = 9\text{mm}$, $l = 18\text{mm}$, $\beta = 18^\circ$ and varying position originating from measurements, XFOIL and RFOIL	79
8.23	Drag polar of the AH93W174 airfoil at $Re = 1.3E6$ with $h = 9\text{mm}$, $l = 18\text{mm}$, $\beta = 18^\circ$ and varying position originating from measurements, XFOIL and RFOIL	79
8.24	Cross-section of the NACA4415 airfoil.	80
8.25	Lift polar of the NACA4415 airfoil at $Re = 2E5$ with $h = 5\text{mm}$, $l = 15\text{mm}$, $\beta = 10^\circ$ and varying position originating from measurements, XFOIL and RFOIL	81
8.26	Drag polar of the NACA4415 airfoil at $Re = 2E5$ with $h = 5\text{mm}$, $l = 15\text{mm}$, $\beta = 10^\circ$ and varying position originating from measurements, XFOIL and RFOIL	81
8.27	Lift polar of the NACA4415 airfoil at $Re = 2E5$ with $l = 3h\text{mm}$, $\beta = 20^\circ$, $x_{vg}/c = 0.3$ and varying height originating from measurements, XFOIL and RFOIL	82
8.28	Drag polar of the NACA4415 airfoil at $Re = 2E5$ with $l = 3h\text{mm}$, $\beta = 20^\circ$, $x_{vg}/c = 0.3$ and varying height originating from measurements, XFOIL and RFOIL	82
8.29	Lift polar of the NACA4415 airfoil at $Re = 2E5$ with $h = 5\text{mm}$, $l = 15\text{mm}$, $x_{vg}/c = 0.3$ and varying inflow angle originating from measurements, XFOIL and RFOIL	83
8.30	Drag polar of the NACA4415 airfoil at $Re = 2E5$ with $h = 5\text{mm}$, $l = 15\text{mm}$, $x_{vg}/c = 0.3$ and varying inflow angle originating from measurements, XFOIL and RFOIL	83
8.31	Probability density function of the error in maximum lift coefficient obtained by XFOIL. Unshaded area indicated 90% confidence interval.	85
8.32	Probability density function of the error in maximum lift coefficient obtained by RFOIL. Unshaded area indicated 90% confidence interval.	85

9.1	Lift polar for three different skin friction multiplication factors for the DU97W300 airfoil at a Reynolds number of $2E6$ with fixed source term.	88
9.2	Drag polar for three different skin friction multiplication factors for the DU97W300 airfoil at a Reynolds number of $2E6$ with fixed source term.	88
B.1	Lift polar of the DU97W300 airfoil at a Reynolds number of $2E6$ with two different K_c expressions.	97
B.2	Drag polar of the DU97W300 airfoil at a Reynolds number of $2E6$ with two different K_c expressions.	97
B.3	Optimal source term versus the angle of attack found using XFOIL with two different K_c expressions.	98
C.1	Lift polar DU97W300 airfoil at $Re = 1E6$	99
C.2	Drag polar DU97W300 airfoil at $Re = 1E6$	99
C.3	Lift polar DU97W300 airfoil at $Re = 2E6$	99
C.4	Drag polar DU97W300 airfoil at $Re = 2E6$	99
C.5	Lift polar DU97W300 airfoil at $Re = 3E6$	100
C.6	Drag polar DU97W300 airfoil at $Re = 3E6$	100
C.7	Lift polar DU91W2250 airfoil at $Re = 2E6$	100
C.8	Drag polar DU91W2250 airfoil at $Re = 2E6$	100
C.9	Lift polar DU93W210 airfoil at $Re = 1E6$	100
C.10	Drag polar DU93W210 airfoil at $Re = 1E6$	100
C.11	Lift polar DU331 airfoil at $Re = 15.8E6$	101
C.12	Drag polar DU331 airfoil at $Re = 15.8E6$	101
C.13	Lift polar FFAW3333 airfoil at $Re = 14.0E6$	101
C.14	Drag polar FFAW3333 airfoil at $Re = 14.0E6$	101
D.1	Empirical source term integral plotted versus the optimal source term integral of XFOIL	103
D.2	Empirical source term integral plotted versus the optimal source term integral of RFOIL	103

List of Tables

7.1	Regression coefficients for XFOIL and RFOIL	62
8.1	Error XFOIL and RFOIL in Figure 8.1	68
8.2	Error XFOIL and RFOIL in Figure 8.3	69
8.3	Error XFOIL and RFOIL in Figure 8.7	71
8.4	Error XFOIL and RFOIL in Figure 8.9	72
8.5	Error XFOIL and RFOIL in Figure 8.11	73
8.6	Error XFOIL and RFOIL in Figure 8.13	74
8.7	Error XFOIL and RFOIL in Figure 8.17	76
8.8	Error XFOIL and RFOIL in Figure 8.19	77
8.9	Error XFOIL and RFOIL in Figure 8.22	79
8.10	Error XFOIL and RFOIL in Figure 8.25	81
8.11	Error XFOIL and RFOIL in Figure 8.27	82
8.12	Error XFOIL and RFOIL in Figure 8.29	83

List of Symbols

α	Angle of attack	C_f	Boundary-layer Skin-friction coefficient
α_{stall}	Tangential force coefficient	C_l	Two-dimensional lift coefficient
β	Inflow angle of the vortex generator	$C_{\tau EQ}$	Equilibrium shear stress coefficient
β	Pressure gradient parameter	$C_{l_{max}}$	Maximum two-dimensional lift coefficient
χ	Back-flow coefficient	C_m	Moment coefficient
δ	Boundary-layer thickness	C_n	Normal force coefficient
δ^*	Displacement thickness	C_t	Tangential force coefficient
δ^{**}	Density flux thickness	C_{VG}	Relaxation parameter
ϵ	Error	D	Dissipation integral
η	Dimensionless similarity variable	D	External vortex generator pair distance
γ	Strength vortex sheet	d	Internal vortex generator pair distance
Λ	Vortex strength	G	Shape parameter of the velocity-defect profile
λ	Source term decay factor	H	Boundary-layer shape factor
\mathcal{D}'	Drag over span	h	Height of the vortex generator
μ	Dynamic viscosity	h^+	Device effective height
ν	Kinematic viscosity	H^*	Kinematic energy shape parameter
ω	Vorticity	H^{**}	Density flux shape parameter
$\overline{I_{ST}}$	Empirical source term integral	H_k	Kinematic shape factor
∂	Partial derivative	h_s	Distance between the limiting streamlines
Ψ	Velocity gradient	I_{ST}	Source term integral
ρ	Density	k	Constant
σ_0	Source term strength	K_c	Shear-lag coefficient
τ	Shear stress	L	Body length
τ_w	Wall shear stress	l	Length of the vortex generator
θ	Momentum thickness	L_i	BAY lift force
θ^*	Dissipation thickness	M	Free stream Mach number
A_{VG}	Plan-parallel area of the vortex generator	p	Pressure
AR	Aspect ratio of vortex generator	Re	Free stream Reynolds number
c	Airfoil chord length	Re_θ	Momentum thickness Reynolds number
C_0, \dots, C_4	Regression constants	S_{VG}	Source term magnitude
C_τ	Shear stress coefficient	u, v	Tangential and normal velocity component
C_D	Dissipation coefficient	U_∞	Tangential free stream velocity component
C_d	Two-dimensional drag coefficient	u_e	Velocity at the edge of the boundary-layer

U_s	Normalized wall slip velocity	2D	Abbreviation two-dimensional
U_{VG}	Velocity at location of the vortex generator	3D	Abbreviation three-dimensional
V_∞	Normal free stream velocity component	AEP	Abbreviation annual energy production
x	Chordwise direction	CFD	Abbreviation computational fluid dynamics
x_{VG}	Chordwise position of the vortex generator	IBL	Abbreviation integral boundary-layer
y	Wall-normal direction	VGs	Abbreviation vortex generators
z	Spanwise direction		

1

Introduction

For the next generation of wind turbines, manufacturers aim to design multi-megawatt wind turbines in order to improve the competitiveness of wind energy technologies. To up-scale wind turbines, novel technologies will be required and new design challenges will appear. One of the major aerodynamic challenge is flow separation. Preventing or at least delaying separation of the flow, can positively affect the annual energy production (AEP). On top of that, the magnitude and severe variations of the aerodynamic loads associated with dynamic stall can be reduced, leading to smaller structural fatigue issues. In the wind energy industry, separation control is often realised by using vortex generators, mainly due to their effectiveness, simplicity and reliability.

Vortex Generators (VGs) improve the resistance against flow separation by re-energising the flow close to the surface. The streamwise vortices shed at the free tips of the vortex generators increase the mixing between the high-energy flow in the outer part of the boundary-layer with the low-energy regions near the walls. For the next generation of wind turbines, it will become necessary to evolve towards a multi-disciplinary design process where vortex generators are already incorporated early in the design phase. In order to assess and optimise the use of these vortex generators, there will be a need to accurately model these devices in a cost and time efficient way. One way to do so, would be to extend integral boundary-layer codes (e.g. XFOIL and RFOIL) such that the aerodynamic performance of airfoils equipped with vortex generators can be predicted. The goal of this master thesis is to work towards the realisation of this and to develop the foundations of the design tools XFOILVG and RFOILVG.

1.1 Thesis Objective

In this master thesis research, steps will be made towards the modelling of vortex generators within the integral boundary-layer theory. The research objective is defined as:

Main Objective: The objective of the research is to model the effect of vortex generators in two-dimensional integral boundary-layer codes (XFOIL or RFOIL) by modifying the closure relations with an additional source term and identifying trends in the relationship for that source term with respect to the vortex generator geometry and boundary-layer properties using aerodynamic properties obtained from CFD and experiments of wind turbine dedicated airfoils.

- **Sub Objective 1:** Adapt XFOIL or RFOIL to imitate the effect of a vortex generator by including an additional source term in the closure relations and changing the transition formulation.
- **Sub Objective 2:** Determine the magnitude of the source term by calibrating the term using detailed lift and drag data obtained from CFD and experiments of wind turbine dedicated airfoils.
- **Sub Objective 3:** Define the dependency of the source term with respect to the vortex generator geometry and boundary-layer properties by setting up an empirical relation for the source term.
- **Sub Objective 4:** Develop XFOILVG and RFOILVG by implementing the source term empirical relation in the integral boundary-layer codes and validate it.

1.2 Methods & Approach

The method and approach used to realise this objective will be presented in this report. The report is structured into four main sections namely: Introduction, Methodology, Results and Discussion. The introduction section is used to present the field of study. Important concepts and theories are introduced and existing research on the subject is presented. This led to an evaluation of the current situation through which the research gap is identified. The next section of this report is the methodology. In this

section, the approach used to arrive to the results is discussed. The different steps taken to achieve the objectives are described and the used material is handled. The novelties of the research are highlighted in this part of the report. The result section is the essence of the work. In this section, the findings are presented and the results are assessed and evaluated. From this, a critical discussion of the results of the research project follows and recommendations for further work are presented. At the end of the report, a conclusion is made.

To navigate the reader through this thesis work, the different chapters of this report will be introduced. Also a schematic thesis outline is provided in Figure 1.1.

- **Chapter 2: Vortex Generators** Vortex generators will play a dominant role in the upcoming research. Chapter 2 deals with a review of this device. First of all, vortex generators will be discussed from a broader view. A short historical background of flow control techniques in general is given as well as the need for flow control. Further details are provided on the working principle of vortex generators and different configurations are highlighted. At the end of this Chapter, the characteristics of the shed vortex and its influence on the flowfield are discussed.
- **Chapter 3: Modelling Techniques for Vortex Generators** In this Chapter, the state-of-the-art of the currently available modelling techniques for vortex generators is described. Different techniques presented in literature are discussed. Most developed modelling techniques are based on computational fluid dynamics, however, an attempt is already made to model vortex generators using the integral boundary-layer theory. Based on this literature review, a scientific gap is recognised and the motivation for this research is presented.
- **Chapter 4: Boundary-Layer Theory** Many complex problems in aerodynamics have been clarified by the introduction of the boundary-layer concept. Chapter 4 has the purpose to introduce this concept to the reader. The well-known boundary-layer equations are presented and two codes that are based on this theory are discussed. At the end of this Chapter, a good understanding of this subject should be reached.
- **Chapter 5: Modifications to the Boundary-Layer Formulation** To extend integral boundary-layer codes to model the effect of vortex generators, modifications need to be made to the boundary-layer formulation. These modifications are presented in Chapter 5. The methodology relies on a source term approach in which an additional term is introduced to the closer relations. This methodology is explained in detail and the code modifications are consequently verified.
- **Chapter 6: Experimental and Numerical Reference Data** To be able to further elaborate the source term approach, reference data is gathered for different airfoil/vortex generator configuration. The reference data base originates from experimental and numerical campaigns that are either performed during this thesis or adopted from external sources. The experiments performed during this thesis are discussed in Chapter 6 as well as the origin of the external reference data.
- **Chapter 7: Source Term Empirical Relation** In Chapter 7, the exact value of the source term for a specific airfoil/vortex generator configuration is determined. To do so, a source term calibration process is presented. Further, an empirical relation is set up for that source term depending on vortex generator geometry parameters and boundary-layer variables. The resulting source term empirical relation is critically reviewed after which it is implemented into two integral boundary-layer codes. At the end of this Chapter, the newly developed XFOILVG and RFOILVG codes are presented.
- **Chapter 8: Validation** The developed airfoil tools XFOILVG and RFOILVG need to be validated to judge whether the codes are performing properly. This validation process is presented in Chapter 8. The simulated aerodynamic properties of an airfoil equipped with vortex generators are compared to reference data. The capability to predict lift and drag is analysed and the codes' performances are evaluated by reflecting back to the assumptions made. Also the code limitations are established.
- **Chapter 9: Recommendations & Further Work** Although great steps are taken in this master thesis towards the modelling of vortex generators within the integral boundary-layer theory, some improvements can still be proposed. Chapter 9 presents some recommendations that may be worth studying further.

- **Chapter 10: Conclusion** In this last Chapter, the conclusions of this research are presented.

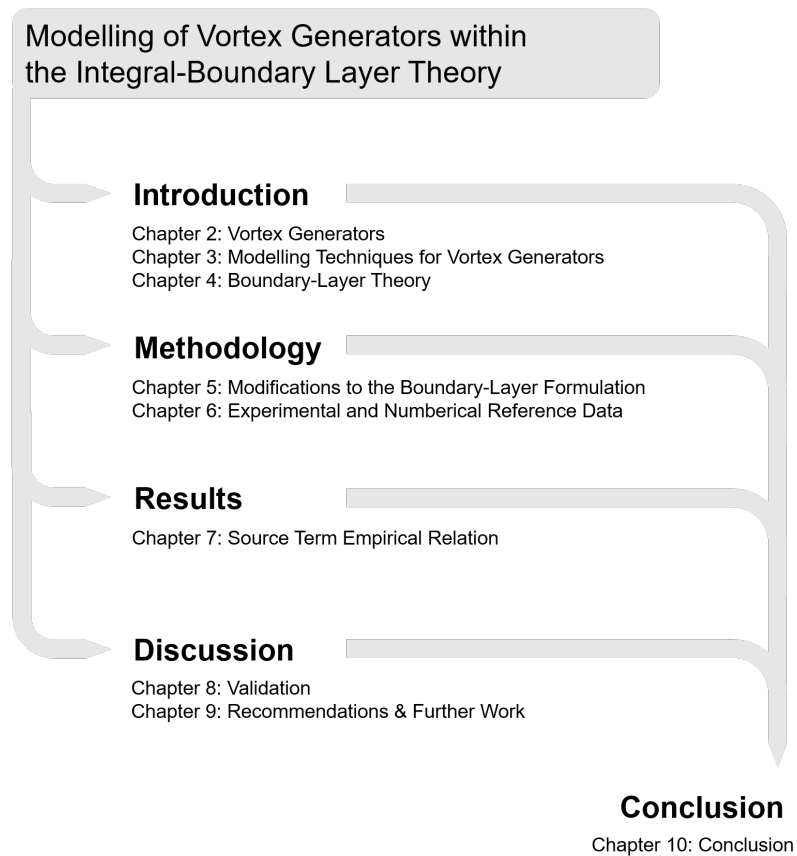


Figure 1.1: Thesis outline.

2

Vortex Generators

One of the most commonly used flow control techniques to trim the aerodynamic performance of wind turbine blades are vortex generators. Vortex generators will play a dominant role in the upcoming research so it is essential to fully understand this subject. In this chapter, various topics regarding this passive flow control technique will be reviewed. In the first section, vortex generators will be discussed from a broader view, within the field of flow control techniques. A short historical background is given, a flow control definition is set up and the section ends with a discussion of the flow that needs to be controlled by flow control techniques. In section 2.2, the working principle of vortex generators is explained while in section 2.3, different vortex generator configurations are highlighted. Consequently, findings dealing with the flow field characteristics behind vortex generators are presented in section 2.4. This subject will be approached by dealing with the induced vortex and its three dimensional effect on the flowfield.

2.1 Flow Control Techniques

Flow control is an interesting topic in fluid dynamics that has been studied for years. In this section, the historical background of flow control is presented. Also, the concept 'flow control' will be defined. Finally, a discussion is provided that deals with the flow phenomena that is to be controlled.

2.1.1 Historical Background

Already before the first manned flight, scientists discovered flow control, even before the full physical mechanism was understood. It is only one year after the Wright brother's did their first flight that Prandtl presented his boundary-layer theory, which is according to Gad-el-Hak¹⁵ the origin of the science of flow control. The use of boundary-layer control for aviation has started to be explored within the next 20 years.¹⁶

The first attempt to use flow control to prevent separation can be dedicated to Prandtl. He experimented with steady suction flow control to remove the boundary-layer on the walls of diffusers.¹⁶ He was the first one to really understand the flow physics behind boundary-layer control, and mainly focused on the prediction of flow resistance. In the beginning of the 1920s, the concept of boundary-layer control for lift enhancements were explored. Baumann¹⁷ introduced air jets and airfoils using suction were investigated by Ackeret et al¹⁸ and Schrenk^{19,20}. These suction techniques played an important role during the Second World War where the aircraft industry received a push and the technology shifted towards high-speed, supersonic aircrafts with small wing areas and higher wing loading.¹⁶ In the late 1940s and 1950s, the NACA research studied the use of distributed suction near the leading edge of the airfoil in the attempt to control the laminar separation bubble.¹⁶ By the late 1960s, active control techniques, meaning that they are internally driven, were no longer the preference of aircraft designers due to their complexity, cost and issues with plumbing and maintenance which are all limiting the reliability.¹⁶ These are some of the reasons why passive flow control techniques are often preferred in the aerospace industry. As stated by the book 'Fundamentals and applications of modern flow control'¹⁶, written by Joslin, examples of passive flow control are vortex generators on aircraft wings and rudders to delay stall^{21,22}, the greatly designed airfoil shapes to delay separation as much as possible²³, spoilers on the leading edges of cavities to suppress resonant tones²⁴ and riblets on wing surfaces to reduce friction drag²⁵. Nowadays, flow control is still a hot topic in fluid dynamics where still a lot of research is performed. One of the novel flow control techniques used to improve aerodynamic characteristics are for example plasma actuators and synthetic jets with flexible membranes.

Joslin¹⁶ describes the evolution of flow control over the last century very well. "We have seen flow control concepts evolve from purely empirical trial-and-error approaches, to techniques of boundary-layer control based on modifying the boundary-layer, to modern flow control techniques structured

around our understanding of fluid flow instabilities." Note that it was only after the Second World War and the oil crisis of 1973 that public interest has grown in flow control techniques which boosted the technology significantly.²

2.1.2 Definition

To be able to thoroughly understand flow control, a clear definition should be given for this concept. Flow control has been described in several ways but Flatt summarised it in 1961 as "boundary-layer control including any mechanism or process through which the boundary-layer of a fluid flow is chased to behave differently than it normally would were the flow developing naturally along a smooth straight surface."¹⁵ In short, this means that flow control is about everything that can be done to manipulate the flow.

Ashill² described that flow control can be seen in two different ways. First of all it can be seen as a way to "provide a fix to cure problems that were not foreseen in the original design and that only emerged later on in the development process". Or secondly, the application of flow control can be part of "a multi-disciplinary design process". This last manner to use flow control gives many opportunities.²

2.1.3 The Need for Flow Control

In the opinion that it is important to understand what flows can profit from some kind of flow control, this section is provided. One particular flow feature will be highlighted, namely flow separation, since this is a flow phenomenon that wants to be prevented very often. Much effort and research has been done to delay flow separation and thus to keep the flow attached to the surface as long as possible. When the boundary-layer separates, a large amount of energy may be lost.¹⁵

The concept of flow separation is clearly described by Gad-El-Hak¹⁵. "Fluid near the surface is decelerated by wall friction and by any adverse pressure gradient present in the freestream. If the near-wall fluid has insufficient momentum for it to continue its motion, it will be brought to rest at the separation point. Further downstream, the adverse pressure forces will even cause reversal flow." When the boundary-layer continuously separates, the boundary-layer will thicken, and this will modify the potential flow outside the boundary-layer and the corresponding pressure field. The normal component of the velocity in the separated flow region will increase and therefore, the approximations assumed to be valid in the boundary-layer break through. The fluid flow will detach from the object's surface and instead forms vortices and large scale eddies. Flow separation results in a drag increment, which is mainly pressure drag. Also a loss of lift and eventually stall can be an undesirable result.

Many scientists have tried to establish a proper definition for flow separation. Ashill² states that the principle of separation is given by "a relationship between the volume flow of the stream tube ϵ , the distance between the limiting streamlines forming the base of the streamtube h_s , the variable height of the streamtube z and the magnitude of the spanwise vorticity at the wall ω_w ", as given in Equation 2.1 derived by Maskell²⁶ and Lighthill²⁷.

$$\frac{1}{2}\omega_w z^2 h_s = \epsilon \quad (2.1)$$

This equation reveals that flow separation may be caused due to two different mechanisms. The first mechanism takes place when the vorticity at the wall vanishes away. This form of separation will result in a bubble. This bubble, formed by the separation surface, isolates a part of the fluid from the main stream. The surface of separation either reattaches itself onto the solid surface or is closed downstream of the body.²⁸ To prevent this type of flow separation, the magnitude of the vorticity at the wall near the singular point can be increased. This type of separation is called singular separation and is shown in Figure 2.1. The second mechanism for flow separation occurs when two streamlines approach each other and the distance between them reduces significantly.² This type of separation has an open structure. At the separation point, the orientation of the two streamlines are the same and they are tangent to each other in the plane of the wall.²⁹ A classical example of this type of separation is the case of a sharp edged delta wing under incidence. In this example, the flow separates from the leading edge and a roll-up vortex sheet will be formed.³⁰ This second type of separation is visualised in Figure 2.2. To prevent this sort of separation, referred to as ordinary separation, it is necessary to prevent that the distance between the streamlines decreases, especially right upstream the separation. Taking this into account, the following ways can be proposed to prevent separation: increasing the

mixing between the flow at the outer part of the boundary-layer and close to the wall, decreasing the adverse pressure gradient, increasing the energy near the wall directly or by introducing vorticity.²

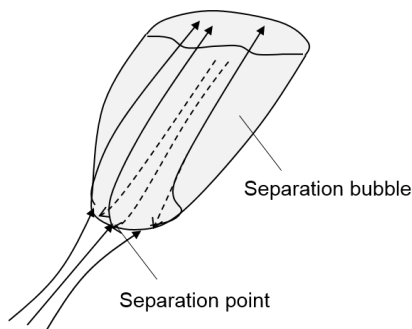


Figure 2.1: Singular separation.²

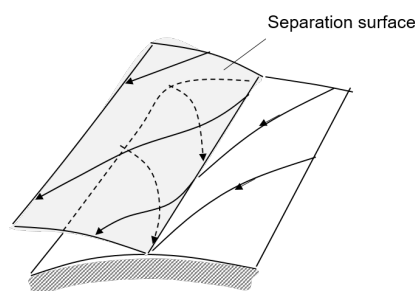


Figure 2.2: Ordinary separation.²

2.2 Working Principle of Vortex Generators

Vortex generators are one of the flow control techniques that have been in use for many years to prevent or at least lessen the severity and delay flow separation.¹ In general, they are assumed to be passive flow control techniques. However, vortex generators may also be active through for example wall jets. The very first experiments with vortex generators are reported by Taylor³¹ already in 1947 where he studied the behaviour of plates glued to an object under an incidence angle with respect to the main flow to prevent separation in diffuser ducts.⁵ The first study describing the effect of vortex generators on the boundary-layer were performed by Schubauer and Spangenberg³² in 1959. They investigated experimentally the effect of increasing the mixing rate in two dimensional turbulent boundary-layers formed on a flat wall. Their major conclusions were that the effect of forced mixing on the boundary-layer is very identical to the effect of reducing the pressure gradient and that an increase in forced mixing causes the displacement and momentum thickness to grow. After the work of Schubauer and Spangenberg was published, more and more research has been performed to fully understand the working principle and flow field behind vortex generators.

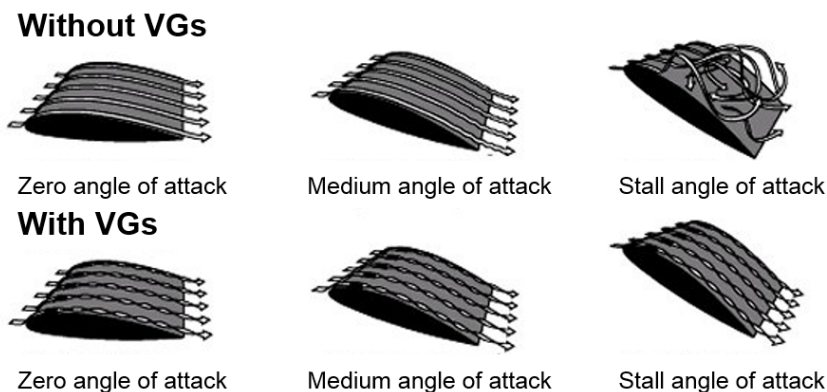


Figure 2.3: Use of vortex generators to delay separation.³

As Manolesos³³ points out, many articles are written by various researchers such as Rao and Kariya³⁴, Pauley and Eaton³⁵ and Lin⁵, about the working principle and underlying mechanisms of vortex generators. A schematic explanation of the use of vortex generators is shown in Figure 2.3. Most researchers are rather consistent to describe that the main function of vortex generators is to increase the mixing between the high-energy layers in the outer part of the boundary-layer and the low-energy regions near the walls by generating streamwise vortices at the free tips of the vortex generators. The energetic, rapidly moving air from outside is drawn into the slow-moving boundary-layer and increases so the near-wall momentum. This re-energising process can make the boundary-layer turbulent (if the vortex generator is operating in a laminar boundary-layer) which is in general more able to handle steeper and larger adverse pressure gradients and is thus more resistant to flow separation than laminar ones.¹

In general it is said that vortex generators reduce drag. However, to discuss this statement, a distinction

should be made between a flow situation where turbulent separation occurs and one where a laminar separation bubble is present. First consider the case of turbulent separation. Without the presence of vortex generators the flow would separate from the wall at high angles of attack. Now, due to the introduction of vortex generators, the flow will be able to remain attached for a larger angle of attack range which will result in a drag reduction at these high angles. However, the effect of the vortex generators is also present at low angles of attack. At these angles the flow is still attached so the increased mixing will result in a drag increase. For the second case where separation bubbles are formed over the airfoil, this observation is slightly different. The mixing effect of vortex generators is able to eliminate or at least reduce the size of separation bubbles. This might result in a drag reduction also at low angles of attack. This is studied by for example Kerho et al.⁴. In Figure 2.4, an example of experimental results is provided, which is obtained by Kerho for three different vortex generator configurations over the entire mid-range of C_l values at a Reynolds number of 235000. Here it is clearly visible that the drag is reduced at almost all lift coefficient with the presence of the flow control accessories because the laminar separation bubbles are suppressed.

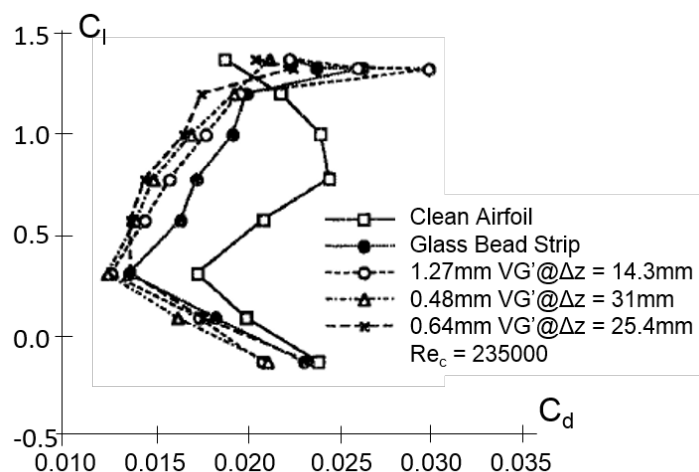


Figure 2.4: C_l vs C_d at a Reynolds number of 235000. Comparison of different vortex generator configurations and a glass bead transition strip. Separation bubbles are present in the clean airfoil case.⁴

2.3 Configuration of Vortex Generators

Vortex generators come in different shapes and sizes with as most important parameters the device geometry, size, orientation and location for effective flow control.⁵ Several studies deal with the design guidance under various flow conditions to find the most effective configuration. Studies of for example Taylor³⁶, Schubauer and Spangenberg³², Pearcey⁶, Lin³⁷ and Wendt³⁸ focused mainly on zero- and adverse pressure gradient flows on a flat plate.³³ It should be noted that research of vortex generators on airfoils is still rather limited. To go a little into the different device geometries, the most general vortex generator is the vane-type. It consists of a small plate (often rectangular or triangular) or an airfoil³⁹ projected normal to the surface and set at an incidence angle β with respect to the mean incoming flow.⁵ Other vortex generator geometries are for example wishbones, doublets and forward and backwards wedges. These different vortex generator types are visualised in Figure 2.5.

There are two basic vortex configurations, the difference being in their inclination with respect to the incoming flow. In the first configuration all generators are positioned under the same inflow angle with respect to the incoming flow. In the second configuration, the vortex generators are assembled in pairs and they are inclined with an opposing orientation. Depending on the case, the shed vortices are rotating in the same direction (co-rotating vortex generators) or in the opposite direction to each pair (counter-rotating vortex generators).⁴⁰ A sketch of the two configurations is provided in Figure 2.5.

Until 1980, the device height was commonly in the same order as the boundary-layer thickness. However, several researchers such as Ashill² and Lin⁵ have shown that low-profile vortex generators with the device height only a fraction of the conventional vortex-generators can still provide sufficient momentum transfer towards the wall over a distance that is several times their own height and as such also serve as a way to effectively control separation. These low-profile vortex generators have as main

advantage that they yield less parasitic drag penalty.

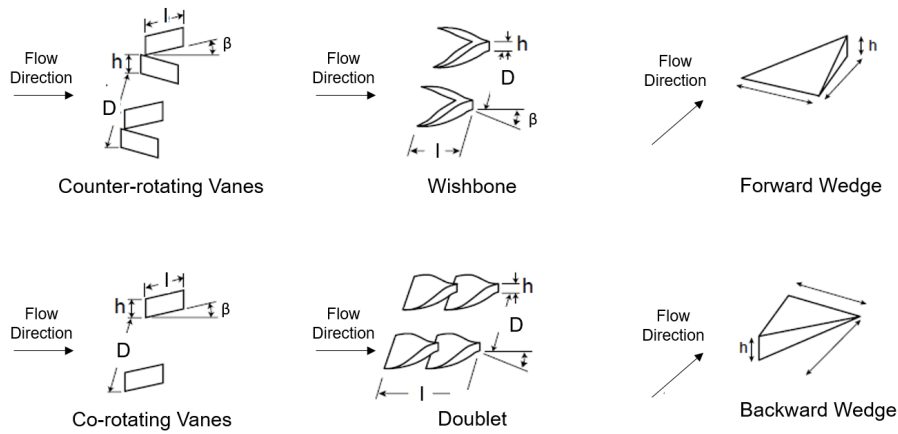


Figure 2.5: Different vortex generator configurations.⁵

2.4 Vortex Characteristics

Besides the mechanism and design guidance, a lot of effort has been done in understanding the flow field behind vortex generators. As already mentioned, vortex generators generate a streamwise vortex which influence the flow field behind the vortex generators significantly. In this section, the vortex characteristics will be highlighted.

It can be expected that the shed vortices downstream the vortex generators affect the boundary-layer and are very important to be able to understand the flow field characteristics. The parameters defining the vortices are the strength of the vortices just downstream of the device, the streamwise decay of vortex strength and the vortex trajectory.² The initial vortex strength is of large importance since it determines the mixing effectiveness just downstream the vortex generator. The decay and trajectory determine the streamwise extent of the effectiveness of the device.

2.4.1 Initial Vortex Strength

The strength of the vortex depends on the vortex generator geometry and the flow field of the undisturbed or uncontrolled flow. This dependency is expressed by Equation 2.2. x_{VG} is the position of the vortex generator measured from the trailing edge, l and h are the length and height of the vortex generator, β is the orientation of the vortex generator with respect to the incoming flow, δ is the boundary-layer thickness of the impinging stream, M is the freestream or core Mach number and Re is the Reynolds number.⁴¹

$$\Lambda = f(x_{VG}, l, h, \beta, \text{profile}, \delta, M, Re, \dots) \quad (2.2)$$

Wendt et al.⁴¹ established as one of the pioneers, a study to define the dependency of vortex generator geometry and flow conditions on the shed vortex. Wendt performed several parametric studies^{38 41} on vortices that are shed from the vortex generators. He has developed a semi-empirical relationship that prescribes the strength of the shed vortices Λ . Using Prandtl's theory of elliptical wings⁴² defining the amount of circulation developed around that cross-sectional profile, and assuming that this circulation is turned into the stream, Wendt derived Equation 2.3⁴¹, and later updated it to Equation 2.4³⁸ where k_1 to k_6 were determined using least-squares regression of experimental data.

$$\Lambda = \frac{k_1 \beta U_\infty c}{1 + k_2 / AR} (h/\delta)^{1/7} \quad (2.3)$$

$$\Lambda = \frac{k_3 \beta U_\infty c}{1 + k_4 / AR} \tanh \left[k_5 (h/\delta)^{k_6} \right] \quad (2.4)$$

Besides Wendt, Ashill⁴³ explained that a dimensional analysis suggested that the circulation correlates with the height of the device and the wall friction velocity in the absence of the device. From this, Equation 2.5 is introduced where U_e is the streamwise velocity at the outer edge of the boundary-layer,

C_f is the local skin friction coefficient of the undisturbed boundary-layer and h^+ is the device effective height also called the device Reynolds number.

$$\frac{\Lambda}{u_\tau h} = f(h^+) \quad (2.5)$$

$$\text{where: } u_\tau = U_e \sqrt{C_f/2} \quad (2.6)$$

$$h^+ = \frac{u_\tau h}{\nu} \quad (2.7)$$

Note that the effective height h^+ does not represent any physical dimension but is only introduced to combine a family of circulation curves for various vortex generator types into a single curve.⁵ The effective heights of the devices are selected by ensuring that the maximum value of non-dimensional circulation based on effective height is independent of geometry.² The curve showing the relation between the non-dimensional circulation based on effective height as a function of non-dimensional effective height is given in Figure 2.6. This relationship is of large value since it provides a framework to predict the vortex strength just downstream the vortex generator of devices for a wide range of Reynolds number.⁵

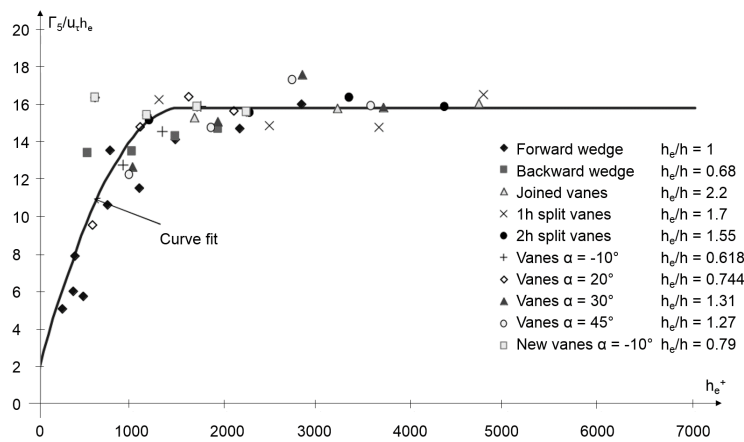


Figure 2.6: Generalised correlation of vortex strength against Reynolds number based on device effective height.²

Other attempts are done to suggest a way to obtain a parametrised model of the initial strength of the shed vortex. A study by Angele and Muhammad-Klingmann⁴⁴ found that for a paired vortex generator configuration, the vortex circulation can be estimated using Equation 2.8 where U_{VG} represents the mean velocity at the location of the vortex generator and k is a coefficient which is a function of the vortex generator velocity.

$$\Lambda = 2k \frac{h}{\delta} U_{VG} \quad (2.8)$$

2.4.2 Vortex Decay

In the inviscid case, the vortex strength would, according to Kelvin's theorem, remain constant in streamwise direction. However, this is not the case in a viscous situation. The strength of vortices generated by vortex generators will decay as they are travelling downstream.

In an ESDU paper⁴⁵, it is tried to define a relation for the decay of the vortex strength. According to this paper, the shed vortex decays under the effect of wall friction. Therefore, it is proposed that the decay rate should be proportional to the local skin friction coefficient C_f in the uncontrolled flow, which is a representation of the viscous shearing effect of the wall. The closer the vortex core is to the surface, the stronger the wall friction effects will be. This is taken into account by stating that the decay rate is inversely proportional to the height of the vortex above the wall h ⁴⁵. By now assuming that the flow in lateral planes is two-dimensional, Equation 2.9 is set up, where k is an empirical constant.

$$\frac{d\Lambda}{dx} = -kC_f \frac{\Lambda}{h} \tag{2.9}$$

From this equation, it can be derived that the vortex strength will decay exponentially with respect to the downstream position measured from the vortex generator position.² A drawback of this approximation is that it only accounts for the effect of wall shear stress. However, the strength of the shed vortices will also decay under the action of boundary-layer turbulence and mutual interference between vortices if they are sufficiently close together.

2.4.3 Vortex Trajectory

A small word should be said about the vortex trajectory. The vortex trajectory is highly influenced by the vortex configuration in spanwise direction. When first considering a single vortex generator vane, it can be said that the vortex core tend to rise with streamwise direction. This vortex trajectory can be explained by the fact that the vortex itself induces a vorticity layer at the wall. The vorticity at the wall is of opposite sign compared to that of the vortex due to the no-slip condition. The vorticity layer will introduce a vertical velocity and will move the vortex away from the wall. The increasing vortex height can thus basically be associated with the interaction between the vortex and the wall.² This is shown in Figure 2.7. How much a vortex is lifted from the wall depends significantly on the vortex configuration. Some references such as the ESDU transonic data memorandum⁴⁵ even suggest that since the height varies only slowly with the streamwise distance, it can be assumed constant.

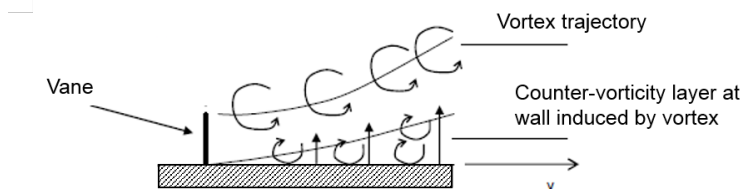


Figure 2.7: Vortex trajectory single vortex generator vane.²

In more practical cases, vortex generators are placed over the whole spanwise direction. In these cases, the neighbouring vortices dictate the trajectory and dynamics. One regularly used configuration is the counter-rotating vortex generator configuration. If the paired vortex generators are closer to each other than two adjacent pairs, the paired vortices will transport one another towards the surface. Then, each vortex will become closer to its image than to its neighbour and so is transported towards the other neighbour. The previous two stages will inevitably lead to the grouping of new pairs in which the vortices transport one another away from the surface. Remember that the vortices are the most effective during the second stage since the vortices are then the closest to the wall.⁶ The process for a pair of initially common downwash vortices is visualised in Figure 2.8.

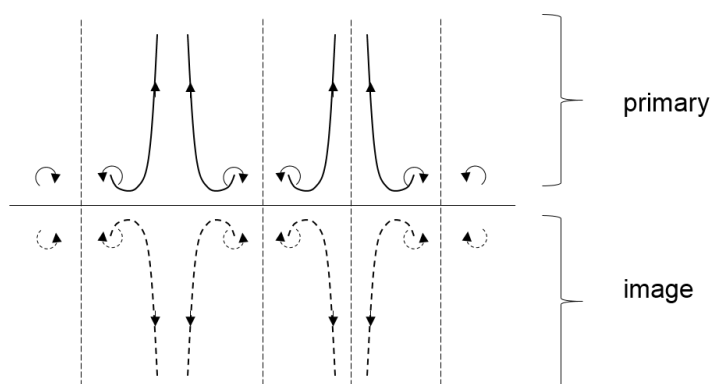


Figure 2.8: Projection of the the vortex trajectory in the frontal plane for counter-rotating vortex generator vane.⁶

For a co-rotating vortex generator configuration, the established vortices will remain undisturbed as the vortices trail downstream. The velocities induced on any vortex is equal and opposite to the one of

its neighbour. Vortices are only displaced laterally under the velocity induced by the imaging vortex in the surface.⁶ This phenomenon is visualised in Figure 2.9.

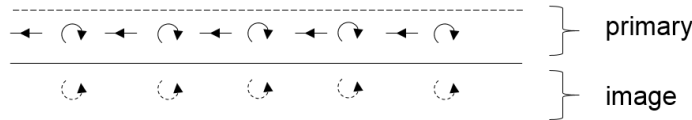


Figure 2.9: Projection of the the vortex trajectory in the frontal plane for co-rotating vortex generator vane.⁶

2.4.4 Three-Dimensional Flowfield

Due to the presence of the shed vortices, the flowfield closely behind a row of vortex generators is fully three-dimensional. The flow properties downstream the vortices are varying in spanwise direction. To demonstrate this, Figure 2.10 adopted from a research paper of D. Baldacchino⁷ is provided.

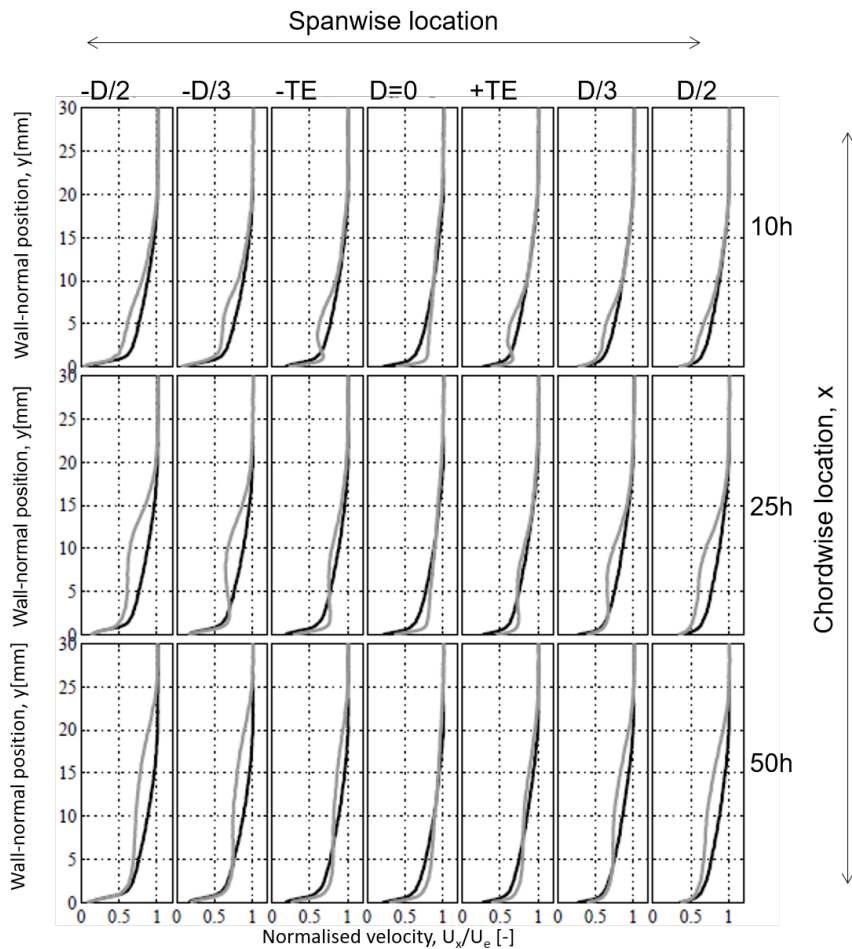


Figure 2.10: Controlled (grey) and baseline (black) streamwise velocity profiles at different spanwise locations behind the VG pair.⁷

In this figure, experimentally gathered streamwise velocity profiles behind a row of rectangular vortex generators for the case of a zero pressure gradient boundary-layer is presented. Different velocity profiles are shown corresponding to different spanwise and chordwise locations. When comparing the velocity profiles of different spanwise positions, it can be said that at the plane of symmetry, in the middle of a vortex generator pair ($D = 0$), the velocity profile is fuller than compared to the profile right between two vortex generator pairs. This is because it is directly under the influence of the strong downwash coming from the vortices. Following from this, note that the displacement thickness, momentum thickness and shape factor are also lower at the plane of symmetry, in between a vortex generator pairs.⁷

Although, the flow field up to 50 VG heights behind the vortex generator still shows a clear three dimensional behaviour, it seems that a quasi two-dimensional flow field could be expected further downstream. Studies⁴⁴ have shown that as you go even further downstream (up to 128 VG heights), the velocity profiles at different spanwise positions, within and outside the vortex generator pair, approach each other. The viscous diffusion causes the vortices to grow, the swirling velocity component to decrease and the boundary-layer to develop towards a two-dimensional state.⁴⁴

To deal with the three-dimensionality of the flowfield in the spanwise sense, especially close to the vortex generators, all provided boundary-layer properties and lift/drag coefficients will refer to spanwise averages.

3

Modelling Techniques for Vortex Generators

To be able to integrate vortex generators as part of a multi-disciplinary design process, there is a strong need to develop reliable and still computationally affordable tools that can predict the aerodynamic characteristics and aeroelastic performance of airfoil designs equipped with these passive flow control devices.⁴⁰ Besides the costly full-scale experiments, different modelling techniques are already presented in literature. Mainly CFD modelling techniques but also already integral boundary-layer techniques are presented. In this Chapter, the state-of-the-art of the currently available modelling techniques for vortex generators will be described.

3.1 Modelling Techniques Using CFD

In this Section, an overview will be given of the modelling techniques to model vortex generators using computational fluid dynamics. Six different techniques, found in literature, will be handled namely the full CFD model, the BAY model, the jBAY model, the vortex-source model, the statistical method and finally Smith's model.

3.1.1 Fully Resolved CFD

The effect of vortex generators, seen as a local geometrical protrusion on for example lifting surfaces, can be modelled using advanced computational fluid dynamics methods. This is a very direct and intuitive approach. Complete flow modelling of blade sections equipped with vortex generators requires a fully three-dimensional treatment due to the complicated flow patterns.⁴⁰ Vortex generators are sized in the same order as the boundary-layer thickness, and this brings problems from a CFD point of view. For every new setting, the mesh around the vortex generators need to be re-determined to be able to obtain an accurate solution. This requires a significant amount of time.^{46,47} Although full CFD calculations deliver accurate results, the time and computer resources required to numerically simulate the full flow, and thus also the large costs accompanied with it, remains a large disadvantage of full computational fluid dynamics methods.

3.1.2 BAY Model

To cope with the issues of the fully resolved CFD, significant progress is made in the last two decades to develop new simplified techniques to model the presence of vortex generators. In 1999, Bender et al.⁴⁸ developed one of the first models. His technique models the effects of vortex generators without including their geometry explicitly in the computational mesh.⁴⁶ His method is based on adding a lateral lift force as a source term to the momentum and energy equation which basically introduces and simulates the swirl in the flow giving rise to the formation of vortices produced by the vortex generators⁴⁹ A number of rows of cells are selected at which a source term will be added and they make a total cell volume about equal to the volume of the vortex generator (shown in Figure 3.1).⁸ The Bender Anderson Yagle model, abbreviated as BAY model, is based on Prandtl's lifting line theory to estimate the lift force that adjusts the local flow velocity with the vortex generator, depending on an empirical model constant.⁴⁷ The magnitude of the lift force depends on local flow quantities and the vortex generator shape and is approximated by Equation 3.1. A_{VG} is the planparallel area of the vortex generator, ΔV_i is the volume of the cell where the force is calculated, V_m is the sum of the volumes of cells where the force term is applied, β is the angle of the local velocity U_{VG} to the vortex generator, and l is the unit vector on which the side force acts. The constant C_{VG} is a relaxation parameter which controls the strength of the side force and consequently the intensity with which the local velocities align with the vortex generator.⁴⁹

$$L_i = C_{VG} A_{VG} (\Delta V_i / V_m) \beta \rho U_{VG}^2 l \quad (3.1)$$

When using the BAY method, the user needs to specify the position and orientation of the vortex generator, as well as the vortex generator model constant. This brings two main difficulties. First of all, because vortex generators are often flat plates with almost negligible thickness, it might be difficult to identify the grid points laying inside the vortex generator. Secondly, correctly determining the vortex generator constant is difficult. It depends on the vortex generator installation in particular in the case of a row of vortex generators. All of this together makes, according to Jirasek⁴⁶, the BAY model, to a certain extent grid dependent.

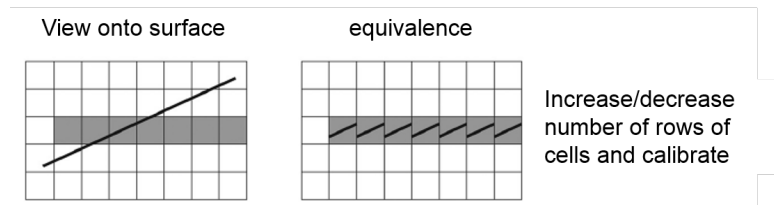


Figure 3.1: Cell selection of BAY model.⁸

3.1.3 jBAY Model

To overcome the shortcomings of the original BAY model, Jirasek suggested an improved BAY model, called the jBAY model. Jirasek⁴⁶ himself explains that in his model, the vortex generator is replaced by a mean surface with zero thickness as in potential theory. Points where the side force is calculated are then determined by the intersection of this mean surface with grid edges (see Figure 3.2). The values of velocity and density needed in the vortex generator model source term are interpolated to these points from grid nodes and the resulting side force is then redistributed back to the nodes and added to the flow equations. Both the BAY as the jBAY approaches use the same meshes and side force expressions, however, the jBAY approach does not require the geometrical structure of the vortex generator any more and is independent of the vortex generator constant. This new model requires minimal user input but keep in mind that the computational grid needs to be sufficiently dense to capture the region downstream of the forcing region where the generated vortex structures need to be resolved. Apart from that sense, it can be said that the jBAY model is grid independent.⁴⁶

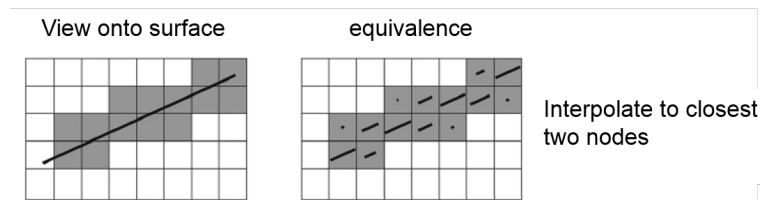


Figure 3.2: Cell selection of jBAY model.⁸

3.1.4 Vortex-Source Model

Besides adding a source term based on a lateral lift force, it is also possible to construct the source term on either a specific circulation or on the velocity induced by this specific circulation according to the Biot-Savart law. This method is referred as vortex-source model.⁴⁹ The key problem of this kind of models is that the initial circulation introduced by the vortex generator needs to be known beforehand. As already pointed out before, different attempts are done to link this circulation as well as other characteristics of it to different vortex generator geometries. There are a number of empirical relations set up such as given by for example Angele et al.⁴⁴. Research based on this method are the spanwise averaged CFD method of Nikolaou⁴⁰ and the three dimensional CFD method by Zhang⁵⁰.

3.1.5 Statistical Method

The statistical approach is another method found in literature towards a simplification of the application of vortex generators within CFD. Tornblom and Johansson⁵¹ presented in 2007 their statistical method. In this method, a Reynolds stress approach is used in a statistical sense. Additional stresses that originate from the modelled vortex generators and their additional vortex velocity field are added to the differential Reynolds stress transport model equations.⁵² This mimics the increased mixing due

to the vortex generators. Within this model, the vortices are approximated by the Lamb-Oseen vortex model.⁵¹ Additionally, the lifting line theory is used to account for the vortex generator geometry effects such as drag. The original proposal of the statistical vortex generator model by Tornblom and Johansson did not account for the vortex-stress components. Improvements are proposed such as extending the Lamb-Oseen vortex model by a streamwise velocity component which improved the flow-separation control compared to the original model.⁵²

3.1.6 Smith's Method

Smith⁵³ presented in 1993 an intermediate approach, combining integral boundary-layer and CFD elements to model the integral effects of vortex generators on a turbulent boundary-layer. His model is built on a theoretical study on the three dimensional turbulent flow created by an array of vortex generators. The goal of Smith's study was to address vortex generators systematically such that the parametric dependency could be investigated. By assuming slender vortex generators with a relatively low profile and a spanwise length scale comparable with the boundary-layer thickness, and a large Reynolds number, Smith reduced the governing equations to a forward-marching three dimensional vortex system. This reduction allows a relatively fast and accurate computation for spanwise periodic vortex generator arrays. The model is mainly appropriate for low-profile vortex generators since in that case most flow effect occur in the logarithmic part of the boundary-layer where the turbulence model seems most representative. The model predicted experimental data well. Positive aspects of this theory are its incorporation of the turbulent stresses, the presence of the logarithmic profile, the flexibility of the formulae and the capturing of major parameters. However, more research is required on the influence of non-linear effects, separation from the vortex generator and the upper edge of the boundary-layer.

3.2 Modelling Techniques Using Integral Boundary-Layer Theory

Most vortex generator modelling efforts are focused on CFD solutions, however also other approaches are described in literature. One academic work is found that deals with the integration of vortex generators into the integral boundary-layer theory. This paper is written in 2003 by Michael Kerho and Brian Kramer¹. The purpose of the study was to incorporate the enhanced mixing effect of boundary-layer mixing devices into an existing airfoil design code, namely the viscous-inviscid program XFOIL to promote the benefits of vortex generators and encourage integrated aerodynamic design.¹

In order to include the mixing effect of vortex generators in the XFOIL code, Kerho and Kramer modified the boundary-layer formulation. In particular, they enhanced the turbulence production in the turbulent boundary-layer formulation by modifying the stress transport formulation. The rate equation is modified at the location of the vortex generators by introducing a step input which decreases exponentially downstream of this location. The decay in amplification was chosen to mimic the downstream decay in shed vorticity generated by a mixing device. In that way, they force the local displacement thickness to decrease and the momentum thickness and skin friction to increase, at least in a spanwise average sense.¹

In the article of Kerho and Kramer¹, it is chosen to calibrate the model for a single row of co-rotating vortex generators with a height to length ratio of 4, local vortex angle of attack of 20 degrees and a spanwise spacing of 8 vortex generator heights. The modified code also includes a transition prediction model based on the roughness based Reynolds number which determines if the vortex generator height with respect to the boundary-layer is sufficient for the vortex generator to promote a bypass transition. If so, transition is fixed to be at the vortex generator location and the mixing effect is included in the boundary-layer model. If the height is insufficient to promote transition, no modification to the transition boundary-layer model is made.¹

Several airfoil sections were designed and tested with the modified XFOIL code. Overall, the modified code predicted the vortex generator behaviour quite well compared to experimental data. Polars proving this statement can be found in Figure 3.3 to Figure 3.5. In the first figure, a comparison is made between the modified XFOIL and experimental lift curves for an NLF airfoil section (i.e EID76SR) equipped with co-rotating vortex generators at 75% of the chord length. The maximum lift coefficient is slightly under predicted by the code compared to the measurement data. Figure 3.4 compares the predicted lift-drag polars with the experimentally obtained ones. Overall, the modified code predicted the behaviour of the vortex generator quite well, however, the minimum point of the drag bucket is slightly underestimated by the new XFOIL code. Finally, in Figure 3.5, the pressure distributions are

compared. Since the Reynolds number is rather low (i.e. 0.7×10^6) separation bubbles were created over the clean airfoil. Using vortex generators prevents this to happen and the flow remains now fully attached over the airfoil.¹

An obvious limitation of this approach is that the fully three-dimensional flow field induced by an array of vortex generators is represented and modelled by a two-dimensional integral boundary-layer formulation. In the close proximity of the vortex generator, the shed vortices create a fully three-dimensional flow field. Further downstream from the vortex-generator position, this flowfield can become two-dimensional again. Although vortex generators yield a locally 3D flowfield, 2D design codes can still be applicable to model the effect of vortex generators. 2D codes could be used to model the global effect of airfoils equipped with vortex generators. If the vortex generators are properly spaced along the airfoil span, the flow field properties in spanwise direction will be periodic. This means that the global effect can be represented by the spanwise average of this periodic behaviour.

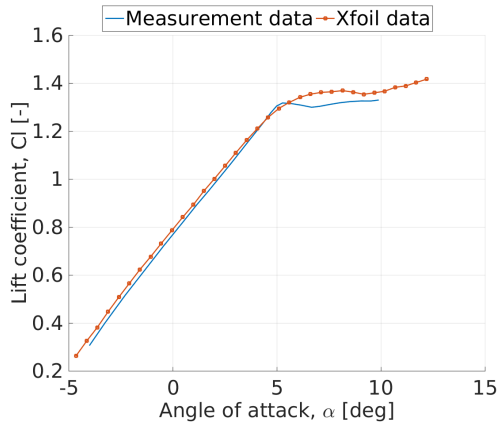


Figure 3.3: Comparison of modified XFOIL and experimental lift curve results for the EID75SR section with co-rotating 0.5δ VGs at $x/c = 0.75$, $Re = 0.7 \times 10^6$.¹

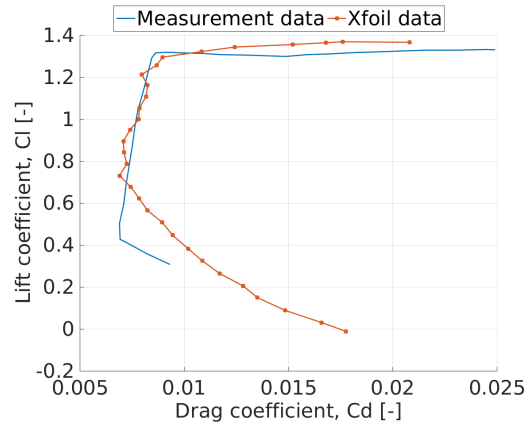


Figure 3.4: Comparison of modified XFOIL and experimental lift-drag curve results for the EID75SR section with co-rotating 0.5δ VGs at $x/c = 0.75$, $Re = 0.7 \times 10^6$.¹

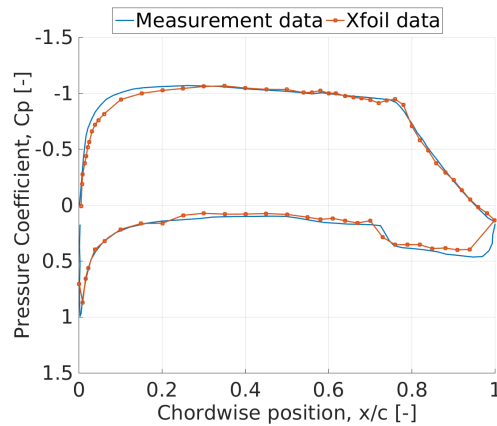


Figure 3.5: Comparison of modified XFOIL and experimental pressure distribution results for the baseline NLF(1)-1015 and EID75SR section with and without co-rotating 0.5δ VGs at $x/c = 0.75$, $Re = 0.7 \times 10^6$.¹

Integrating flow control devices into the integral boundary-layer theory is not a new idea. Several other control devices have already been implemented successfully in viscous-inviscid codes such as XFOIL or RFOIL. However, note that both techniques discussed below have a more two-dimensional behaviour than vortex generators have. One example is boundary-layer suction. The thesis of Merchant⁵⁴ (a student of Drela), Ferreira⁵⁵ and later de Oliveira⁵⁶ studied and adapted the original closure relations of Drela to account for mass transfer. From these last two studies, the codes XFOILSUC and RFOILSUCV2 are developed at Delft University of Technology. As another example, de Oliveira et al.⁵⁷, modelled DBD plasma actuators in integral boundary-layer formulation. An asymptotic expansion to the Navier-Stokes equations is performed by introducing an additional force term, as to obtain

a generalised form of the von Karman integral equations. New closure relations were derived and the modelling approach is validated. The results were very encouraging for further research.

3.3 Research Gap

The flow field behind vortex generators is reasonably well understood. Although remarkable advances are made in the modelling of vortex generators using computational fluid dynamic techniques, these techniques are still very expensive and impractical to use in iterative design processes. In addition to that, it is known that CFD techniques in general do not achieve the same accuracy and consistency as integral boundary-layer models for undisturbed flows.⁷ Therefore, it would be of great value to extend integral boundary-layer codes such that they can analyse the influence of flow mixing devices on airfoil performance.

Kerho and Kramer¹ already made big advances towards the modelling of vortex generators within the integral boundary-layer theory. However, their article is still very qualitative and gives a rather vague description of the modifications applied to XFOIL. No clear approach and methodology is presented such that their method can be easily reproduced.

Also, their model is calibrated for one specific case with a single row of co-rotating vortex generators. No attempts are made to calibrate their model for different vortex generator geometries and local flow conditions and to extend their approach such that the aerodynamic behaviour of different vortex generator configurations and flow conditions could be predicted.

The region of interest of Kerho and Kramer¹ is also different than the one aimed for in the wind energy industry. They studied natural-laminar-flow airfoils at relatively low operational Reynolds numbers. For wind energy applications, different airfoil families are used often at much larger Reynolds numbers. Also, it is remarkable that Kerho and Kramer only studied cases where vortex generators are installed far downstream. In most applications, vortex generators are installed closer to the leading edge. No results are reported that analysed the code robustness regarding airfoil choice, Reynolds number and vortex generator location.

It is noteworthy that no articles were found that are building on the Kerho-Kramer approach. Based on the very preliminary results described in the article¹, it is believed that further work can be promising. A lot of work can still be performed to improve their methodology, especially towards the source term calibration and code robustness. This is where a scientific gap is recognised. The main research objective is defined as:

Main Objective: The objective of the research is to model the effect of vortex generators in two-dimensional integral boundary-layer codes (XFOIL or RFOIL) by modifying the closure relations with an additional source term and identifying trends in the relationship for that source term with respect to the vortex generator geometry and boundary-layer properties using aerodynamic properties obtained from CFD and experiments of wind turbine dedicated airfoils.

- **Sub Objective 1:** Adapt XFOIL or RFOIL to imitate the effect of a vortex generator by including an additional source term in the closure relations and changing the transition formulation.
- **Sub Objective 2:** Determine the magnitude of the source term by calibrating the term using detailed lift and drag data obtained from CFD and experiments of wind turbine dedicated airfoils.
- **Sub Objective 3:** Define the dependency of the source term with respect to the vortex generator geometry and boundary-layer properties by setting up an empirical relation for the source term.
- **Sub Objective 4:** Develop XFOILVG and RFOILVG by implementing the source term empirical relation in the integral boundary-layer codes and validate it.

4

Boundary-Layer Theory

Many complex problems in aerodynamics have been clarified by the introduction of the boundary-layer concept. A good understanding of this concept is essential for the further research, and therefore this chapter is provided. In the first section, a general description of the boundary-layer concept will be given. Then, the boundary-layer parameters will be introduced. In section 4.3, the well-known boundary-layer equations will be presented by highlighting the major steps of the derivation. The boundary-layer theory is the basis of two well-known airfoil performance codes. How these boundary-layer codes are solving a viscous boundary layer routine is discussed in section 4.4

4.1 Boundary-Layer Concept

In fluid dynamics, the concept of a perfect fluid is often adopted. In that case, friction and compressibility are neglected with the consequence that two layers only experience normal pressure forces and no tangential shearing forces. Although the theory of perfect fluids is very well understood, it fails to compute any drag forces. Also, the molecular attraction causes the fluid to adhere to a solid wall, which contradicts with the slip condition in the absence of tangential forces. These two statements imply that tangential forces are of large importance and cannot be neglected as such. The tangential or friction forces are strongly connected to one particular property, called viscosity.⁵⁸

The effect of viscosity at high Reynolds number flows is restricted to a very thin region in proximity to the wall. Within that layer, the flow velocity rises from zero at the wall (no-slip condition) to its full value which corresponds to the external frictionless flow. This layer is called the 'boundary-layer'.⁵⁹ The concept of the boundary-layer is firstly introduced by Ludwig Prandtl in 1904. He reasoned based on experimental results that for a sufficiently large Reynolds number, a thin region exists near the wall where viscous effects are at least as important as inertial effects, even for very small viscosities.⁵⁸

A fluid flow can thus be divided in two regions: the outer inviscid flow and the inner viscid flow. In Figure 4.1, a schematic representation of the boundary-layer concept is given. Two velocity profiles are shown at two different points along the surface. The first one represents a laminar boundary-layer while the second one is positioned after transition and represents a turbulent boundary-layer velocity profile. The thickness of the viscid region rises in downstream direction, but it remains thinner compared to the outer inviscid region. Within the boundary-layer, the streamwise tangential velocity changes rapidly normal to the surface meaning that the velocity gradient is large in this region. According to Newton's shear-stress law, stating that the shear-stress is linearly proportional to the velocity gradient (see Equation 4.1), the local shear stress may be rather high within the boundary-layer. As a result, the skin-friction drag force exerted on the body may not be neglected, contrary to what was believed by earlier scientists.⁶⁰ In viscid flows, the Reynolds number becomes an essential parameter to define a flow since it represents the ratio between inertia and viscous forces.

$$\tau = \mu \frac{\partial u}{\partial y} \quad (4.1)$$

That the boundary-layer flow was not necessarily laminar but could also become turbulent was pointed out in early experiments by Froude, Eiffel and Prandtl.⁶¹ The smooth laminar boundary-layer introduces a low skin friction, but is at the same time less stable. As soon as the laminar flow breaks down, the flow undergoes a transition and becomes a turbulent flow which is characterised by eddies and fluid mixing. The turbulent boundary-layer introduces a larger velocity gradient and consequently a larger skin friction than the laminar boundary-layer, but is on the same time more stable. The turbulent boundary-layer has irregular fluctuations in velocity magnitude and direction. The change from a lami-

near to a turbulent state can be triggered by the pressure gradient, the roughness of the surface or the influence of external disturbances such as noise or turbulence intensity.^{11 12}

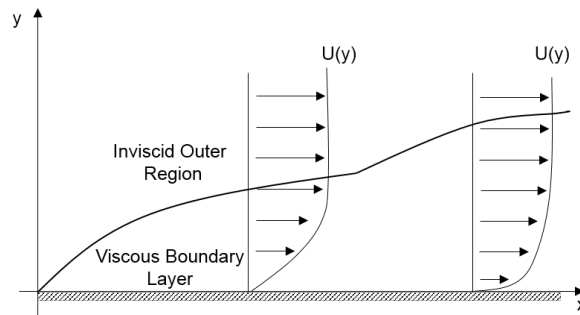


Figure 4.1: Boundary-layer concept.⁹

Prandtl also remarked on flow separation. Separation occurs when the boundary-layer needs to overcome a too large adverse pressure gradient. In that case the flow separates from the surface and takes the forms of eddies. Strictly speaking, separation can be defined as being a phenomenon where the slope of the velocity profile at the surface becomes zero, and thus consequently also the wall shear stress is zero. The boundary-layer will become thicker and if there is no further adverse pressure gradient in the flow direction to overcome, the main flow will reattach to the surface. This is referred to as a separation bubble and is basically a bounded area of backwards flow. The location where separation occurs is not stable, especially not in turbulent flows, but moves back and forth in all directions on the surface of the object in question. To be able to describe the fluctuating nature of a separated region in turbulent flow, the back-flow coefficient χ is introduced by Simpson. This coefficient is the fraction of the time that the local flow direction is against the free-stream.⁶² In the free stream and in zero or even negative pressure gradient boundary-layers, the back-flow coefficient will be close to zero. Further, if a strong adverse pressure gradient is present, the coefficient increases. The back-flow coefficient can maximum reach the value 1 which indicates that the flow is constantly directed in upstream direction and thus that the flow is completely separated.⁶³

4.2 Boundary-Layer Parameters

Some important boundary-layer parameters need to be introduced. The primary boundary-layer variables of interest are the boundary-layer thickness, displacement thickness, momentum thickness, shape factor and skin friction coefficient.¹ In the first part of this Section, the definitions of these boundary-layer parameters are given. Then, to give a better physical understanding, the simplified definitions of the Blasius solution of a flat plate will be discussed. At the end of this section, additional attention is given a one non-dimensional parameter in particular, namely the dissipation coefficient. It is of large importance that this parameter is properly understood since it will play an important role in upcoming discussions.

4.2.1 Definitions of Boundary-Layer Parameters

The boundary-layer thickness, often described by δ , represents the thickness of the viscous boundary-layer region. In a boundary-layer, the fluid asymptotically approaches the outer velocity as you move away from the wall. Therefore, it is conventional to define the edge of the boundary at the point where the fluid velocity equals 99% of the outer velocity.⁶⁴ In Figure 4.2, a schematic representation is given explaining the boundary-layer thickness.

The displacement thickness, symbolised by δ^* , is a measure of the amount the outer inviscid flow field is displaced by the presence of the viscous boundary-layer.¹ In other words, it gives a measure for the defect in mass flow due to the presence of the boundary-layer.¹⁰ If the velocity distribution within the boundary-layer is known, then the displacement thickness can be easily calculated by using Equation 4.2, where u is the velocity in the boundary-layer and u_e represents the fluid velocity outside the boundary-layer. In Figure 4.3, a schematic representation of the displacement thickness is provided. Note that the areas enclosed by the shaded triangular surfaces are equal.

$$\delta^* = \int_0^{\infty} \left(1 - \frac{u}{u_e}\right) dy \approx \int_0^{\delta} \left(1 - \frac{u}{u_e}\right) dy \quad (4.2)$$

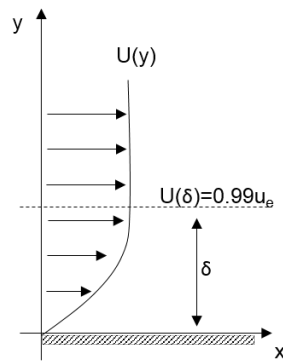


Figure 4.2: Boundary-layer thickness.⁹

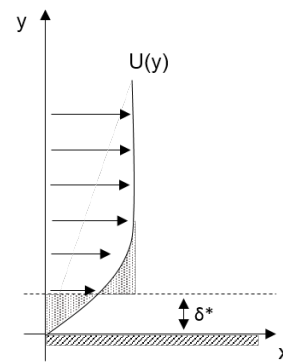


Figure 4.3: Displacement thickness.⁹

Analogue to the displacement thickness definition, the momentum thickness, named by the symbol θ , is a measure of the amount of momentum lost by the flow due to the presence of the viscous boundary-layer.¹⁰ The momentum thickness is described by Equation 4.3. It can be visualised similarly to the displacement thickness except the specific momentum flux distribution $u(y)^2$ replaces the velocity distribution.

$$\theta = \int_0^{\infty} \frac{u}{u_e} \left(1 - \frac{u}{u_e}\right) dy \approx \int_0^{\delta} \frac{u}{u_e} \left(1 - \frac{u}{u_e}\right) dy \quad (4.3)$$

The shape factor, H , is the ratio of the displacement thickness over the momentum thickness, as given by Equation 4.4. It gives an indication of the state of the boundary-layer. In Figure 4.4, a visualisation of a low and high shape factor is given. The shape factor proves its importance in the prediction of for example transition and separation. Typical values for laminar flows are $H = 2.4 - 2.6$ while for turbulent flows the shape factor is typically around $H = 1.3 - 1.4$. It is difficult to specify an exact value of H that corresponds to separation. Vos¹⁰ states that the onset of separation starts at a shape factor of around $H = 3$. In a paper written by Cebeci⁶⁵, it is said that separation exists when H is between 1.8 and 2.4. It is expected that the first value corresponds to laminar separation while the second one refers to turbulent separation.

$$H = \frac{\delta^*}{\theta} \quad (4.4)$$

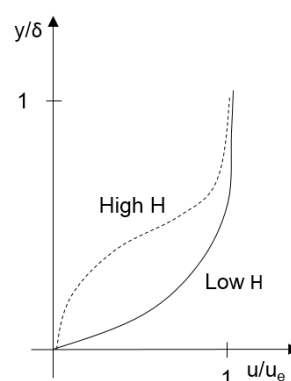


Figure 4.4: Shape factor.¹⁰

The displacement thickness, momentum thickness and shape factor are called the integral boundary-layer parameters and these three parameters allow to examine the state of the boundary-layer and the effect of mixing on the mean flow without becoming involved with detailed flow processes.¹

As last primary boundary-layer variables, the skin friction will be introduced. The skin-friction coefficient is the non-dimensional form of the wall shear stress. The wall shear stress is given by the slope of the

velocity profile of the boundary-layer at the wall. In Equation 4.5 and Equation 4.6, both parameters are prescribed by an equation.

$$C_f = \frac{2\tau_w}{\rho u_e^2} \quad (4.5)$$

$$\text{where: } \tau_w = \mu \left(\frac{\partial u}{\partial y} \right)_{y=0} \quad (4.6)$$

Next to the previously mentioned parameters, also the dissipation integral, dissipation coefficient and dissipation thickness should be defined for later use, as given in Equation 4.7, Equation 4.8 and Equation 4.9 respectively. The density flux thickness, kinetic energy shape parameter and density flux shape parameter are given by Equation 4.10, Equation 4.11 and Equation 4.12.¹²

$$D = \int_0^\infty \tau \frac{\partial u}{\partial y} dy \quad (4.7)$$

$$C_D = \frac{D}{\rho u_e^3} \quad (4.8)$$

$$\theta^* = \int_0^\infty \frac{u}{u_e} \left(1 - \frac{u^2}{u_e^2} \right) dy \quad (4.9)$$

$$\delta^{**} = \int_0^\infty \frac{u}{u_e} \left(1 - \frac{\rho}{\rho_e} \right) dy \quad (4.10)$$

$$H^* = \frac{\theta^*}{\theta} \quad (4.11)$$

$$H^{**} = \frac{\delta^{**}}{\theta} \quad (4.12)$$

4.2.2 Blasius Solution for Flat-Plate Flow

One of the most celebrated solutions for a laminar boundary-layer flow past a flat plate is the one found by Blasius⁶⁶ in 1908. The Blasius solution is a similar solution where the dimensionless similarity variable η is given by Equation 4.13 and the non-linear Blasius equation is given by Equation 4.14. In this equation, the prime denotes the differentiation with respect to η . The solution of the Blasius equations can be used to study how the boundary-layer parameters behave.¹¹ The Blasius solution is visualised in Figure 4.5.

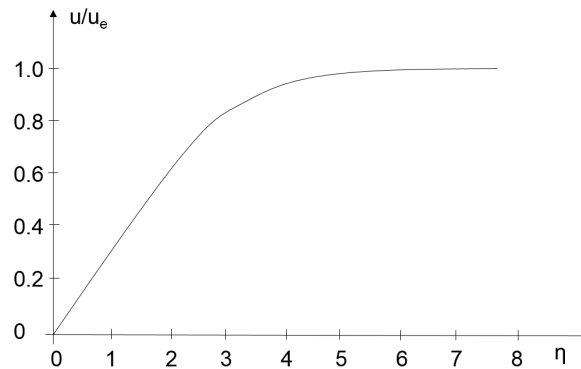


Figure 4.5: Blasius velocity profile.¹¹

$$\eta = y \sqrt{\frac{u_e}{2\nu x}} \quad (4.13)$$

$$f''' + f f'' = 0 \quad (4.14)$$

$$\text{where: } \Psi = \sqrt{2\nu u_e x} f(\eta) \quad (4.15)$$

Since the viscous forces balance the inertia forces (condition of equality) within the boundary-layer, it can be said that Equation 4.16 is true for a laminar boundary-layer over a flat plate. In this equation u_e

denotes the velocity outside the boundary-layer and L is the plate length. From this, it can be derived that the boundary-layer thickness is reversed proportional to the square root of the Reynolds number. This means that the larger the Reynolds number will be, the thinner the boundary-layer becomes.⁵⁸

$$\mu \frac{\partial^2 u}{\partial y^2} \sim \rho u \frac{\partial u}{\partial x} \quad (4.16)$$

$$\mu \frac{u_e}{\delta^2} \sim \frac{\rho u_e^2}{L} \quad (4.17)$$

$$\delta \sim \frac{1}{\sqrt{Re}} \quad (4.18)$$

The numerical factor can be deduced from the exact solution of the Blasius flow. The boundary-layer thickness will be given by Equation 4.19 for a laminar flow, where x is the downstream position measured from the leading edge.¹¹

$$\delta = \frac{5x}{\sqrt{Re_x}} \quad (4.19)$$

Also the momentum and displacement thickness can be derived using the Blasius solution. For a flat plate, the boundary-layer parameter definitions simplify to Equation 4.20 and Equation 4.21. This result says that the displacement thickness is about 3 times smaller than the boundary-layer thickness. Both parameters decrease with increasing Reynolds number.¹¹ For derivations of these equations, the reader is referred to general fluid dynamics literature such as 'Viscous Fluid Flows'¹¹.

$$\delta^* = \frac{1.7208x}{\sqrt{Re_x}} \quad (4.20)$$

$$\theta = \frac{0.664x}{\sqrt{Re_x}} \quad (4.21)$$

Finally the skin friction coefficient and shape factor are given by Equation 4.22 and Equation 4.23. This shows that with increasing Reynolds number, the skin friction coefficient of the plate decreases. On the other hand, the shape factor is independent of the Reynolds number.¹¹

$$C_f = \frac{0.664}{\sqrt{Re_x}} \quad (4.22)$$

$$H = 2.59 \quad (4.23)$$

4.2.3 Dissipation Coefficient

Because the dissipation coefficient will be of major importance in the upcoming work, a deeper discussion will be given about this particular non-dimensional parameter.

To start, the Reynolds-averaged Navier-Stokes equation should be recapped. The dependent field quantities are Reynolds decomposed meaning that they are divided into a component representing the mean and a part representing the deviation from the mean. Using this decomposition, the averaged momentum equation can be derived for a 2D steady, incompressible flow, as given in Equation 4.24.

$$\bar{u} \frac{\partial \bar{u}}{\partial x} + \bar{v} \frac{\partial \bar{u}}{\partial y} = \frac{-1}{\rho} \frac{\partial p}{\partial x} + \frac{1}{\rho} \frac{\partial \bar{u}}{\partial y} \left(\mu \frac{\partial \bar{u}}{\partial y} - \rho \overline{u'v'} \right) \quad (4.24)$$

The last term is better known as the shear stress consisting of two parts: the first part being the laminar part while the second part is the Reynolds stress and accounts for the turbulent fluctuations.⁶⁷ (Equation 4.25)

$$\tau = \mu \frac{\partial \bar{u}}{\partial y} - \rho \overline{u'v'} \quad (4.25)$$

From this point on, the dissipation integral can be introduced. The dissipation integral D is an integral property which measures the local rate of flow kinetic energy dissipation into heat by the shear stress τ acting on the fluid which is deforming at the shear strain rate $\partial u / \partial y$.¹² This is given in Equation 4.26.

$$D = \int_0^{\infty} \tau \frac{\partial \bar{u}}{\partial y} dy \quad (4.26)$$

$$= \int_0^{\infty} \left(\mu \frac{\partial \bar{u}}{\partial y} - \rho \overline{u'v'} \right) \frac{\partial \bar{u}}{\partial y} dy \quad (4.27)$$

The dissipation coefficient, being the non-dimensional form of the dissipation integral, depends on the boundary-layer parameters. For self-similar flows the relation between the dissipation coefficient, shape factor and Reynolds number is given in Figure 4.6. For any given local Reynolds number, the minimum dissipation occurs very close to the zero pressure gradient H value corresponding to the flat plate case.¹² It is also immediately clear that the laminar dissipation coefficient is almost independent of pressure gradient and inverse dependent on Reynolds number. The turbulent dissipation coefficient varies significantly with pressure gradient while the dependency with respect to Reynolds number is much softer.

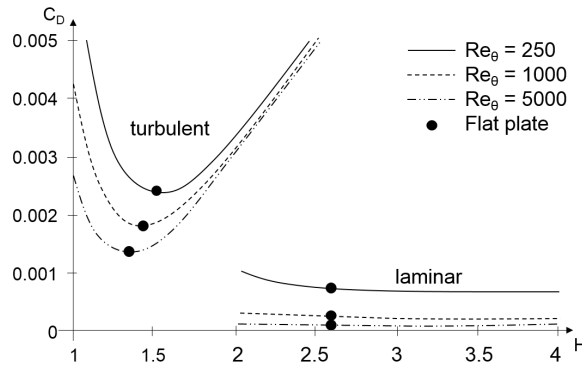


Figure 4.6: Dissipation coefficient for self-similar flows.¹²

It can easily be shown that the viscous dissipation is responsible for the total profile drag ($\mathcal{D}'_{friction} + \mathcal{D}'_{pressure}$), including the pressure drag component, as derived in a book of Drela¹². Equation 4.28, where \mathcal{D}' denotes drag/span and D refers to the dissipation integral, has a power balance interpretation. The drag must be balanced by an external thrust force which moves at speed U_{∞} relative to the airmass, and thus exerts a power of $\mathcal{D}'U_{\infty}$ which is all dissipated in the viscous layers. The profile drag is thus related to viscous stresses as quantified by the distribution of the dissipation integral. Basically, the larger the dissipation factor, the larger the drag will be. In that sense it might be desirable to minimise the dissipation quantity.¹²

$$\mathcal{D}'_{friction} + \mathcal{D}'_{pressure} = \frac{1}{U_{\infty}} \int_{airfoil+wake} D dx \quad (4.28)$$

However, another important role of the dissipation coefficient is that it controls the maximum tolerable adverse pressure gradient which a boundary-layer can sustain with a constant margin from separation, or equivalently with a nearly constant H and H^* . Equation 4.29 defines the most negative tolerable velocity gradient Ψ_{min} . Note that the second approximate value in this equation is only valid for turbulent flow in very strong adverse pressure gradients near separation. By increasing the dissipation, the boundary-layer will be able of better sustaining very strong adverse pressure gradients.¹²

$$\Psi_{min} = \left(\frac{\theta}{u_e} \frac{du_e}{dx} \right)_{min} = \frac{1}{H-1} \left(\frac{C_f}{2} - \frac{2C_D}{H^*} \right) \approx -0.65C_D \quad (4.29)$$

4.3 Boundary-Layer Equations

To model the flow in the vicinity of the body surface where viscosity plays an important role, the boundary-layer equations are set up. The boundary-layer equations are a deduction of the well-known Navier-Stokes equations of viscous fluid flows and are derived in several books such as 'Viscous Fluid Flows'¹¹, 'Computational Fluid Dynamics'⁶⁸ and 'Modelling and Computation of Boundary-Layer Flows'⁶⁹. The boundary-layer equations are valid within the boundary-layer but also for other shear layer flows such as jets, wakes and mixing layers. In this Section the boundary-layer equations for a laminar boundary-layer flows as well as a turbulent boundary-layer equations will be introduced.

4.3.1 Laminar Boundary-Layer Equations

The continuity and Navier-Stokes equations for a two-dimensional steady incompressible flow is given by Equation 4.30a to Equation 4.30c where u and v are the tangential and normal velocity components, ρ is the density, p is the pressure and ν is the kinematic viscosity of the fluid at a point. This set is a parabolic system of ordinary differential equations. The complete derivation of these equation of motions will not be repeated in this report, the reader is referred to general fluid dynamics books for detailed information.

$$\text{Continuity equation: } \frac{\partial u}{\partial x} + \frac{\partial v}{\partial y} = 0 \quad (4.30a)$$

$$\text{X-momentum equation: } u \frac{\partial u}{\partial x} + v \frac{\partial u}{\partial y} = \frac{-1}{\rho} \frac{\partial p}{\partial x} + \nu \left(\frac{\partial^2 u}{\partial x^2} + \frac{\partial^2 u}{\partial y^2} \right) \quad (4.30b)$$

$$\text{Y-momentum equation: } u \frac{\partial v}{\partial x} + v \frac{\partial v}{\partial y} = \frac{-1}{\rho} \frac{\partial p}{\partial y} + \nu \left(\frac{\partial^2 v}{\partial x^2} + \frac{\partial^2 v}{\partial y^2} \right) \quad (4.30c)$$

For convenience, this set of second order differential equations is made non-dimensional. The non-dimensional variables are prescribed by Equation 4.31 to Equation 4.35 and use scaling factors such as body length L and free stream velocity U_∞ . Note that the corresponding order of magnitude is added to the equations. In Equation 4.36 the Reynolds number equation is shown.⁶⁸

$$u^* = \frac{u}{U_\infty} = \mathcal{O}(1) \quad (4.31)$$

$$v^* = \frac{v}{U_\infty} = \mathcal{O}(\delta) \quad (4.32)$$

$$p^* = \frac{p}{\rho U_\infty^2} = \mathcal{O}(1) \quad (4.33)$$

$$x^* = \frac{x}{L} = \mathcal{O}(1) \quad (4.34)$$

$$y^* = \frac{y}{L} = \mathcal{O}(\delta) \quad (4.35)$$

$$Re = \frac{U_\infty L}{\nu} = \mathcal{O}\left(\frac{1}{\delta^2}\right) \quad (4.36)$$

Using these non-dimensional definitions, Equation 4.30a to Equation 4.30c can be transformed into Equation 4.37a to Equation 4.37c.

$$\text{Continuity equation: } \frac{\partial u^*}{\partial x^*} + \frac{\partial v^*}{\partial y^*} = 0 \quad (4.37a)$$

$$\text{X-momentum equation: } u^* \frac{\partial u^*}{\partial x^*} + v^* \frac{\partial u^*}{\partial y^*} = \frac{\partial p^*}{\partial x^*} + \frac{1}{Re} \left(\frac{\partial^2 u^*}{\partial x^{*2}} + \frac{\partial^2 u^*}{\partial y^{*2}} \right) \quad (4.37b)$$

$$\text{Y-momentum equation: } u^* \frac{\partial v^*}{\partial x^*} + v^* \frac{\partial v^*}{\partial y^*} = \frac{\partial p^*}{\partial y^*} + \frac{1}{Re} \left(\frac{\partial^2 v^*}{\partial x^{*2}} + \frac{\partial^2 v^*}{\partial y^{*2}} \right) \quad (4.37c)$$

Assuming that the boundary-layer is significantly thinner than a streamwise length scale L , the Navier-Stokes equations can be simplified based on an order of magnitude analysis. From the thin layer theory, it follows that the variation in properties in the streamwise direction are generally much lower than those in the wall normal direction. Also keeping in mind that in the boundary-layer the viscous forces balance the inertia and pressure gradient forces, it can be said that the boundary-layer thickness is of the order L/\sqrt{Re} . Using the orders of magnitude assigned to each variable, as shown in Equation 4.31 to Equation 4.35, and going back to the dimensional form of the variables, it can be shown that the Navier-Stokes equation can be simplified to Equation 4.38a to Equation 4.38c.⁶⁸

$$\text{Continuity equation: } \frac{\partial u}{\partial x} + \frac{\partial v}{\partial y} = 0 \quad (4.38a)$$

$$\text{X-momentum equation: } u \frac{\partial u}{\partial x} + v \frac{\partial u}{\partial y} = \frac{-1}{\rho} \frac{\partial p}{\partial x} + \nu \frac{\partial^2 u}{\partial y^2} \quad (4.38b)$$

$$\text{Y-momentum equation: } \frac{-1}{\rho} \frac{\partial p}{\partial y} = 0 \quad (4.38c)$$

This last equation implies that the pressure across the boundary-layer is constant, and thus also equal to the inviscid pressure at the edge of the boundary-layer at the same streamwise position. The pressure is thus no longer an unknown and can be derived from the Bernoulli equation. The pressure gradient can be expressed by Equation 4.39 where u_e represents the fluid velocity outside the boundary-layer.

$$\frac{-1}{\rho} \frac{\partial p}{\partial x} = u_e \frac{\partial u_e}{\partial x} \quad (4.39)$$

Substituting this within the simplified x-momentum equation gives the final boundary-layer equations for laminar flows. These equations are summarised in Equation 4.40a to Equation 4.40c.

$$\text{Continuity equation: } \frac{\partial u}{\partial x} + \frac{\partial v}{\partial y} = 0 \quad (4.40a)$$

$$\text{X-momentum equation: } u \frac{\partial u}{\partial x} + v \frac{\partial u}{\partial y} = u_e \frac{\partial u_e}{\partial x} + \nu \frac{\partial^2 u}{\partial y^2} \quad (4.40b)$$

$$\text{Y-momentum equation: } \frac{-1}{\rho} \frac{\partial p}{\partial y} = 0 \quad (4.40c)$$

4.3.2 Turbulent Boundary-Layer Equations

As already mentioned, turbulent boundary-layers have unsteady velocity magnitudes. In order to take this into account, the velocity will be represented by two parts: a mean velocity and a fluctuating part. This methodology is known as the Reynolds decomposition method. The 2D expressions for the velocity and pressure are given by Equation 4.41 to Equation 4.43 where the mean parts are represented by a bar and the fluctuating parts by a prime. Note that a flow in laminar state has no fluctuating part and only consists of the mean velocity.⁶⁹

$$u = \bar{u} + u' \quad (4.41)$$

$$v = \bar{v} + v' \quad (4.42)$$

$$p = \bar{p} + p' \quad (4.43)$$

Substituting the expression of Equation 4.41 to Equation 4.43 into the general Navier-Stokes equations (Equation 4.30a to Equation 4.30c) allows to find the Reynolds-averaged Navier-Stokes (RANS) equations. Then using a similar order of magnitude analysis as in the laminar case, the following set of equations is found (Equation 4.44a to Equation 4.44c). Detailed derivations can be found in open literature such as the book 'Modelling and Computation of Boundary-Layer Flows'⁶⁹.

$$\text{Continuity equation: } \frac{\partial \bar{u}}{\partial x} + \frac{\partial \bar{v}}{\partial y} = 0 \quad (4.44a)$$

$$\text{X-momentum equation: } \underbrace{\bar{u} \frac{\partial \bar{u}}{\partial x} + \bar{v} \frac{\partial \bar{u}}{\partial y}}_{(1)} = \underbrace{\frac{-1}{\rho} \frac{\partial \bar{p}}{\partial x}}_{(2)} + \nu \underbrace{\frac{\partial^2 \bar{u}}{\partial y^2} - \frac{\partial}{\partial y} (\overline{u'v'})}_{(3)} \quad (4.44b)$$

$$\text{Y-momentum equation: } \frac{-1}{\rho} \frac{\partial \bar{p}}{\partial y} = 0 \quad (4.44c)$$

When considering the x-momentum equation in more detail (Equation 4.44b), one can recognise three main parts. The first part, at the left hand side of the equation, represents the inertial forces (convective term). The right hand side of the momentum equation contains both the pressure forces (part 2) as well as the viscous forces of part 3 (diffusive term). In the turbulent x-momentum equation, an additional term appears compared to the laminar case. This term $u'v'$ is known as the Reynolds shear stress and is an additional unknown to the system. In a book of Kundu⁷⁰, the Reynolds stress is described as the average stress exerted by turbulent fluctuations on the mean flow. It can also be interpreted as it is the rate of mean momentum transfer by turbulent fluctuations. Reynolds stresses are often much greater than viscous stresses with the exception very close to the wall. There the mean velocity gradient is large and the velocity fluctuations are going towards zero. Reynolds stresses are unknowns and need to be derived using a turbulence model such as the Spalart-Allmaras model or the $k-\omega$ model. These models aim to express the Reynolds stresses in terms of known flow parameters.

4.4 Boundary-Layer Codes

The boundary-layer theory is the basis on which boundary-layer airfoil codes are build. These codes are able to calculate the pressure distribution over an airfoil and thus predict the lift and drag performance. Most of these codes are using the same solution routine. This routine is build on Prantl's theory. According to Prantl's theory, it is convenient to divide the flow field around an object into two areas: the inviscid outer flow where viscosity can be neglected without significant effect on the solution and the viscid inner flow, where viscosity plays an important role. How these two flow fields are solved and coupled together will be explained in this section. At the end of this section, a closer look will be given to two well-known airfoil codes, namely XFOIL and RFOIL

4.4.1 Inviscid Solution

In literature, numerous variations are proposed to the use of inviscid panel methods.⁷¹ They differ in for example type of panels or boundary conditions and they all have their own strengths and weaknesses.

One of the inviscid formulations that is very often used in boundary-layer codes is a simple linear-vorticity streamfunction panel method. In this inviscid solution method, a general two-dimensional inviscid airfoil flowfield is constructed by the superposition of a freestream flow, a vortex sheet of strength γ on the airfoil surface and a source sheet of strength σ on the airfoil surface and wake.⁷¹ For this configuration, the streamfunction corresponds to Equation 4.45, where s is the coordinate along the vortex and source sheets, r is the magnitude of the vector between the point at s and the field point (x, y) , θ is the vector's angle and U_∞ and V_∞ are the velocity components of the free stream.⁷¹

$$\Psi(x, y) = U_\infty y - V_\infty x + \frac{1}{2\pi} \int \gamma(s) \ln r(s; x, y) ds + \frac{1}{2\pi} \int \sigma(s) \theta(s; x, y) ds \quad (4.45)$$

Drela⁷¹ explains that "the airfoil contour and wake trajectory are discretized into flat panels as shown in Figure 4.7. Each airfoil panel has a linear vorticity distribution defined by the node values γ_i and a constant source strength σ_i . To the wake panels, only a constant source strength is attributed. A panel of uniform source strength and vortex strength are placed across the airfoil trailing edge."

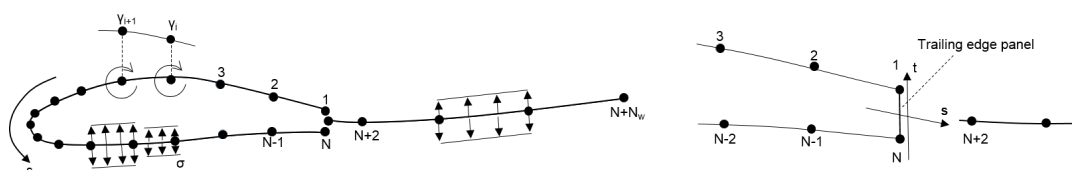


Figure 4.7: Airfoil and wake panelling with vorticity and source distributions, with trailing edge detail.¹³

Now, by requiring that the streamfunctions are equal to some constant value at each node of the airfoil, a linear set of equations can be set up. To be able to close this system and make it solvable, the system is combined with the Kutta condition.⁷¹ This condition states that the flow should leave the trailing edge of an airfoil smoothly and thus the pressure coefficient of the first panel must be equal to that of the last panel, or in other words the velocity magnitudes should be equal. As a final note, it should be remarked that the inviscid formulation of XFOIL and RFOIL incorporates a Karman-Tsien compressibility correction allowing a good compressible prediction up to sonic conditions.⁷²

4.4.2 Viscid Solution

The viscid boundary-layer solution can also be found in different ways. However, most boundary-layer codes obtain for a solution method called the numerical integral method. Contrary to the differential method, in which the continuity and momentum equations need to be solved as a fully partial differential equation to find the detailed u, v, τ fields are computed, the integral method focuses on determining the integral thickness and key shear quantities, namely δ^* , θ , C_f , C_D . These last variables only need to be determined on every streamwise position, which means that the integral method is very economical due to its small number of unknowns.¹² The integral boundary-layer formulation can be shown to be hyperbolic in nature which facilitates the design of stable spatial discretization schemes.⁷³ By integrating the boundary-layer equations, the partial differential equations are transformed into an ordinary differential equation. Note that the solution of the integral method cannot produce theoretically exact solutions but can still provide accurate answers to complex problems, with better efficiency than the

differential methods.

The integral method completely relies on the derivation of two integral equations. These two equations are the integral momentum equation and the integral kinetic energy equation. They can be obtained by integrating the momentum and continuity equations across the boundary-layer thickness, in y -direction.

Integral Momentum Equation: The integral momentum equation is derived by Von Karman in 1921. To obtain the momentum integral relation, the continuity equation as given in Equation 4.38a is multiplied with $(u - u_e)$ and subtracted from the x -momentum equation given in Equation 4.38b. The result is given in Equation 4.46.¹¹

$$-v \frac{\partial^2 u}{\partial y^2} = \frac{\partial}{\partial x} (uu_e - u^2) + (u_e - u) \frac{\partial u_e}{\partial x} + \frac{\partial}{\partial y} (vu_e - vu) \quad (4.46)$$

When now integrating this equation with respect to y from the wall to infinity, the boundary-layer approximation is found (see Equation 4.47). Note that both shear stress and the velocity component in y direction vanish at infinity. If the wall is impermeable, the last term can be neglected.¹¹

$$-v \frac{\partial^2 u}{\partial y^2} = \frac{\partial}{\partial x} \int_0^\infty (uu_e - u^2) dy + \frac{\partial u_e}{\partial x} \int_0^\infty (u_e - u) dy - (vu_e)_{y=0} \quad (4.47)$$

By replacing the integrals by the boundary-layer parameters, the momentum relation can be written in a more compact form. For steady flow with an impermeable wall, this reduces to Equation 4.48. This is the most seen form of the Von Karman integral relation.

$$\frac{\tau_w}{\rho u_e^2} = \frac{C_f}{2} = \frac{\partial \theta}{\partial x} + (2\theta + \delta^*) \frac{1}{u_e} \frac{\partial u_e}{\partial x} \quad (4.48)$$

$$= \frac{\partial \theta}{\partial x} + (2 + H) \frac{\theta}{u_e} \frac{\partial u_e}{\partial x} \quad (4.49)$$

Integral Energy Equation: The integral energy equation is derived by Leibenson in 1935. The energy integral relation can be obtained by multiplying the continuity equation as given in Equation 4.38a with $(u^2 - u_e^2)$ and the x -momentum equation given in Equation 4.38b with $2u$ and consequently subtracting them from each other (see Equation 4.50).¹¹

$$2v \frac{\partial^2 u}{\partial y^2} \frac{\partial u}{\partial y} = \frac{\partial}{\partial x} (uu_e^2 - u^3) + \frac{\partial}{\partial y} (vu_e^2 - vu^2) \quad (4.50)$$

Finally, this equation can be integrating in y -direction from the wall to infinity. Again the boundary-layer parameter expressions are used to write the integral equation in a more compact way. In Equation 4.51, the final version of the integral momentum equation, assuming steady flow and impermeable walls, is presented.

$$\frac{2D}{\rho u_e^3} = 2C_D = \frac{\partial \theta^*}{\partial x} + \left(3 + \frac{2\delta^{**}}{\theta^*}\right) \frac{\theta^*}{u_e} \frac{\partial u_e}{\partial x} \quad (4.51)$$

$$= \frac{\partial \theta^*}{\partial x} + \left(3 + \frac{2H^{**}}{H^*}\right) \frac{\theta^*}{u_e} \frac{\partial u_e}{\partial x} \quad (4.52)$$

The integral momentum equation and the integral kinetic energy equation are useful qualitative equations. In most boundary-layer codes, both equations are solved together and this is referred to as the so-called two-equation integral method such as those of Leballeur⁷⁴, Whitfield et al.⁷⁵, and Drela et al.¹³

However, when considering the two equations, one can recognise that these equations contain six unknowns δ^* , θ , C_f , C_D , H^* , H^{**} and cannot be solved without additional information. The number of boundary-layer integral parameters exceeds the number of equations available. In order to make the problem determinate, the four secondary boundary-layer parameters have to be expressed directly or indirectly via a chain of closure relations, as a function of the primary unknowns.⁷³ The functional

dependencies shown in Equation 4.53a are assumed where H_k is the kinematic shape parameter defined with the density taken constant across the boundary-layer.⁷¹ The closure formulas can be constructed in different ways for example from experimental boundary-layer data, from numerically obtained velocity profiles or through an assumed set of velocity profiles.⁷³ Due to this, it is true that different boundary-layer codes may adopt different closure relations.

$$H^* = H^*(H_k, M_e, Re_\theta) \quad (4.53a)$$

$$H^{**} = H^{**}(H_k, M_e) \quad (4.53b)$$

$$C_f = C_f(H_k, M_e, Re_\theta) \quad (4.53c)$$

$$C_D = C_D(H_k, M_e, Re_\theta) \quad (4.53d)$$

The derived closure relations also differ for turbulent or laminar flow regimes. Therefore, it is of extreme importance to accurately predict where transition will occur. Most codes use a spatial-amplification theory based on the Orr-Sommerfeld equation. This is basically the same as the e^n method of Smith and Gamberoni⁷⁶ which assumes that transition occurs when the most unstable Tollmien-Schlichting wave in the boundary-layer has grown by some factor, usually taken to be $e^9 = 8100$. Tollmien-Schlichting waves are sinusoidal-oscillating pressure and velocity perturbations within the boundary-layer. They usually have a very small amplitude near the leading edge that grow exponentially up to a level that is sufficient to trigger transition.¹² It can basically be said that the e^n method does not really predict transition but rather predicts the growth of periodic laminar instabilities.⁷⁷

4.4.3 Viscid/Inviscid Coupling

As was suggested by Prantl, the solution of the complete flow field can be split in the solution of the outer potential flow and the inner viscous boundary-layer. However, it is impossible to separate the problem into two independent solutions. There is such a strong interaction between the two regions that the two sets of equations need to be coupled. Because the outer flow velocity is an input to the boundary-layer equations and the displacement thickness resulting from the boundary-layer equations is required to compute the outer flow velocity field, it can be said that the potential and boundary-layer flow problems are two-way coupled. To deal with this interactions scheme, different coupling techniques exist.

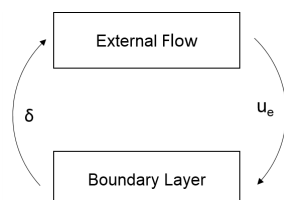


Figure 4.8: Diagram viscid-inviscid interaction.

One of the most powerful methods to deal with the strong interaction between the viscous and inviscid flow field is the use a fully-simultaneous coupling scheme. The fully-simultaneous coupling concept was first described by Drela, Giles and Thompkins⁷⁸. Instead of iterating between the viscous and inviscid solvers, the entire non-linear equation set is solved simultaneously as a fully coupled system by a global Newton-Raphson method.¹³ The integral boundary-layer equations are directly coupled with the system of equations for the inviscid solution through for instance an adapted continuity equation which incorporates the boundary-layer displacement thickness or through the concept of wall transpiration. Fully simultaneous coupling is a robust, accurate, fast and very stable calculation procedure and can deal with separated flow.¹³

The system of non-linear equations can be rewritten as Equation 4.54, where Q represents the vector of variables and F is the vector of equations.

$$F(Q) = 0 \quad (4.54)$$

The method starts with making an initial guess which is considerably close to the real solution. Then an approximation of the function F is made by computing the line tangent to the function. With this new

approximation, the x intersection can be computed. It follows now that the found intersection is most probably a better approximation of the function's solution than the initial guess. This methodology is repeated till the solution converges. The method can be summarised as shown in Equation 4.55.

$$F^v + \left[\frac{\partial F}{\partial Q} \right]^v \partial Q^v = 0 \quad (4.55)$$

$$Q^{v+1} = Q^v + \partial Q^v \quad (4.56)$$

The Newton method is an extremely powerful technique. In general the convergence pattern is quadratic which leads to the fact that XFOIL only requires around 3 iterations for a subsonic and up to 15 iterations for a transonic case to find its final solution.¹³

4.4.4 Xfoil and Rfoil

Two of the best known boundary-layer codes are XFOIL and RFOIL. These two codes are very closely related to each other. The first version of XFOIL was written by Mark Drela in 1986 and since then numerous revisions have been done. Version 6.9 is now officially frozen and all further developments will be incorporated in a completely new next-generation code. The main goal to develop XFOIL was to combine the speed and accuracy of high-order panel methods with the fully-coupled viscous/inviscid interaction method such that the computation time was significantly reduced. A fully interactive interface allows the user to easily handle the code.⁷² Mark Drela wrote several articles^{71 13} as well as a PhD thesis⁷⁹ to explain the basic theory behind the XFOIL software. RFOIL, on the other hand, is a variant of XFOIL and is a result of the TIDIS (Three Dimensional effects in stall) project of ECN, NLR and the Institute for Wind Energy of the TU Delft and was presented in 1996.⁸⁰ The original XFOIL code was lagging the capability to calculate the airfoil performance over a sufficient large range of angles of attack and generally broke down when entering the post stall region, and therefore one of the goals of this project was to improve the two-dimensional post stall lift prediction of the XFOIL code. To obtain this, improvements are made to the numerical stability of the code along with adjustments of some of the turbulent closure relations.⁸⁰ The most important differences between both codes are summed up in the report of R. van Rooij⁸⁰ but will be repeated in this part.

First of all, some improvements are made to the numerical stability of calculations at angles of attack beyond the stall angle. Altered upwinding and relaxation parameters are adopted. Also, changes are made into the initial values of the boundary-layer properties. Especially the initial value of the shear stress coefficient seemed to have a significant effect on convergence.⁸⁰

The most important differences between XFOIL and RFOIL can be recognised within the closure relations. These relations are set up separately for the laminar and turbulent boundary-layer. Besides maybe the refinements of some constants, the laminar closure relations remained untouched. However, more significant changes are made into the turbulent boundary-layer formulation. The major change can be related back to one of the closure relations, namely the closure relation of the turbulent dissipation coefficient.⁸⁰

Following Drela¹³, "the dissipation coefficient is expressed as a sum of a wall layer and a wake layer contribution, where both terms consist of a stress and a velocity scale." The relation is given by Equation 4.57, where the shear coefficient C_τ is a measure of the shear stresses in the wake layer, and U_s is an equivalent normalised wall slip velocity being a function of H , H^* and H_k .¹³

$$C_D = \frac{C_f}{2} U_s + C_\tau (1 - U_s) \quad (4.57)$$

The skin-friction coefficient C_f depends only on local boundary-layer parameters. This is not the case for the shear stress coefficient C_τ and can be explained by the fact that the Reynolds stresses in the wake layer are known to respond relatively slowly to changing conditions.¹³ The additional closure relation describing the shear stress coefficient follows from a simplified version of the stress-transport equation of Bradshaw and Ferriss⁸¹, also called the rate equation of C_τ or the shear-lag equation. The shear stress expression, given in Equation 4.58 is set up such that it is build around the concept of equilibrium flow and thus depends on an equilibrium shear stress coefficient. Equilibrium flows are self-similar, meaning that the velocity and shear-stress profiles do not vary with the x -coordinate.⁸⁰

$$\frac{\delta}{C_\tau} \frac{dC_\tau}{dx} = K_c \left(C_{\tau_{EQ}}^{1/2} - C_\tau^{1/2} \right) \quad (4.58)$$

$$\text{Where: } C_{\tau_{EQ}} = H^* \frac{0.015 (H_k - 1)^3}{1 - U_s} \frac{1}{H_k^2 H} \quad (4.59)$$

The equilibrium shear stress coefficient $C_{\tau_{EQ}}$ is derived by elaborating the $G - \beta$ locus of equilibrium boundary-layers postulated by Clauser⁸². The so-called $G - \beta$ locus, given by Equation 4.60, relates the pressure gradient parameter β and the shape parameter of the velocity-defect profile G empirically to each other.⁸⁰ The $G - \beta$ locus constants A and B basically control the equilibrium level of the shear stress of the turbulent boundary layer. For these parameters, many different combinations are in use. Drela adopted in XFOIL the combination of $A = 6.7$ and $B = 0.75$ ¹³ while in RFOIL these values are changed to $A = 6.75$ and $B = 0.83$.⁸⁰ This is a major difference between XFOIL and RFOIL and according to the developers of RFOIL their adaptations improves the maximum lift predictions compared to the predictions of XFOIL.

$$G = A \cdot \sqrt{1 + B \cdot \beta} \quad (4.60)$$

$$\text{Where: } \beta = -\frac{2}{C_f} \frac{\delta^*}{u_e} \frac{du_e}{dx} \quad (4.61)$$

$$G = \frac{H-1}{H} \sqrt{\frac{2}{C_f}} \quad (4.62)$$

There is one more unknown parameter in the shear-lag equation, namely the shear-lag coefficient K_c . This parameter expresses how much the actual shear stress lags behind the equilibrium shear stress.⁸⁰ In slowly changing flows, the boundary-layer will behave closely as the equilibrium boundary-layer. On the other hand, the more rapidly the flow is changing, the more the flow will deviate from its equilibrium position and the more the rate equation will come into play.¹³ This is especially important when the shape factor H is changing rapidly. In the original XFOIL code, the lag coefficient was kept constant to the same value as Green, namely $K_c = 5.6$. In RFOIL, the lag coefficient is linked to the shape factor since this parameter indicates how much the actual flow deviates from the equilibrium flow. Based on an engineering approach using experiments, Equation 4.63 was proposed. This improvement had a large effect on the post-stall lift curve predictions.⁸⁰

$$K_c = 4.65 - 0.95 \cdot \tanh(0.275 H_k - 3.5) \quad (4.63)$$

To conclude this discussion, the major differences between XFOIL and RFOIL can be summarised as⁸⁰:

- Different initial conditions
- Different constants in the $G - \beta$ locus
- Different expression for the shear lag coefficient K_c

5

Modifications to the Boundary-Layer Formulation

In the previous chapters, the working principle of vortex generators and the theory behind integral boundary-layer codes were discussed. Now, it is time to combine both. In this chapter, the modifications of the boundary-layer formulation necessary to model vortex generators will be described. This chapter is structured as follows. In the first section, the general principle of the vortex generator modelling technique will be presented. In section 5.2 and section 5.3, a deeper look will be given into that approach, by discussing in particular where in the closure relations the source term should be added exactly and what the general shape of the source term should be. Vortex generators may influence the location at which the flow transitions from a laminar to a turbulent boundary-layer. This is treated in section 5.4. Finally, the implementation of the boundary-layer modifications will be verified and the effect of the additional source term is demonstrated in section 5.5. The source term approach is consequently implemented within XFOIL and RFOIL and this implementation can be found in Appendix E.

5.1 Source Term Approach

Integrating vortex generators into the integral boundary-layer theory is not straightforward. It is well-known and already discussed earlier that vortex generators produce a fully three-dimensional flowfield. Because of this 3D behaviour, it is difficult to theoretically derive new boundary-layer equations that can predict the behaviour of vortex generators. Kerho and Kramer¹ presented a methodology to still include vortex generators in the integral boundary-layer theory. Their work is revised carefully since it will be the basis of this thesis work.

The article of Kramer and Kerho¹ is very descriptive but gives a rather vague explanation of the modifications done to integrate vortex generators within the integral boundary-layer theory. The authors explain that they "enhanced the turbulence production in the turbulent boundary-layer formulation by modifying the stress transport formulation. The rate equation is modified at the location of the vortex generators." In other words, the article suggests a modification of the dissipation coefficient through the shear stress coefficient by introducing a step input which decreases exponentially downstream of this location. This information can be translated into a more practical explanation, by looking at equations.

The equation of the dissipation coefficient C_D is given in Equation 5.1. It is expressed as the sum of a wall layer and a wake layer contribution where C_τ is a measure of the shear stresses in the wake layer, C_f is the skin-friction coefficient and U_s is an equivalent normalised wall slip velocity.

$$C_D = \frac{C_f}{2} U_s + C_\tau (1 - U_s) \quad (5.1)$$

Further, C_τ is given by the rate equation. The rate equation is actually a simplified form of the stress-transport equation of Bradshaw and Ferriss⁸¹. Based on the description of Kerho and Kramer¹, it is understood that an additional source term is added to that equation at the streamwise location of the vortex generator which has an initial strength of σ_0 that decays exponentially at a rate λ further downstream. C_τ is expressed by Equation 5.2.

$$\frac{\delta}{C_\tau} \frac{dC_\tau}{dx} = K_c \left(C_{\tau EQ}^{1/2} - C_\tau^{1/2} \right) + S_{VG} \quad (5.2a)$$

$$\text{Where: } S_{VG} = 0, \quad x < x_{VG} \quad (5.2b)$$

$$S_{VG} = \sigma_0 e^{-\lambda(x-x_{VG})}, \quad x \geq x_{VG} \quad (5.2c)$$

In corroboration of Kerho and Kramer¹'s ideas, Drela also insinuated that the vortices shed by vortex generators increase the dissipation. Also Drela refers in one of his works¹² that vortex generators promote an increased dissipation by introducing streamwise vortices into the boundary-layer at some distance from the wall. This increased dissipation allows the boundary-layer to sustain a larger adverse pressure gradient and thus to prevent or delay separation.

5.2 Source Term Implementation

To follow the method of Kerho and Kramer¹, the source term should thus be added to the rate equation. The rate equation, also called the shear lag equation, is an ordinary differential equation for the shear stress level in the boundary-layer. This equation includes a simplified model that accounts for the history effects that dominate turbulence intensity.⁵⁶ The shear stress coefficient C_τ does not depend only on the local conditions because it is known that Reynolds stresses in the wake layer respond relatively slowly to changing conditions.¹³ The rate equation depends on an empirical constant K_c controlling the reactivity of the boundary-layer and on the equilibrium shear stress coefficient $C_{\tau EQ}$.

Within the shear lag equation, the equilibrium shear stress coefficient $C_{\tau EQ}$ is the fundamental parameter.⁵⁶ The equilibrium shear stress coefficient represents the shear stress that would correspond to the value if the local boundary-layer would be in equilibrium. An equilibrium flow means that the boundary-layer profile for a turbulent flow exhibits a behaviour analogous to the similar flows of laminar boundary-layer theory.⁸³ In other words, a flow is assumed to be in equilibrium if it is self-similar. In slowly changing flows, C_τ closely follows $C_{\tau EQ}$ and is thus almost in equilibrium. However, in rapidly changing flows, this is not true and the rate equation thus plays an important role. A simple expression for $C_{\tau EQ}$ can be obtained from the well-known $G-\beta$ locus of equilibrium boundary-layers proposed by Clauser.¹³

Now, because $C_{\tau EQ}$ is seen as the fundamental parameter of the rate equation and because the rate equation, in the shape as it is given by Equation 5.2, is not explicitly used within integral boundary-layer codes such as XFOIL or RFOIL, the source term to model vortex generators is added to the equilibrium shear stress coefficient $C_{\tau EQ}$. This seems to represent the same as was intended by Kerho and Kramer¹ and is thus an appropriate location at which the source term can be added. The source term is thus not introduced as shown by Equation 5.2 but as given by Equation 5.3. Attempts are done to add the source term at different locations, however, it is found that adding the source term to the equilibrium shear stress coefficient was favourable considering the convergence speed and stability of XFOIL and RFOIL.

$$\frac{\delta}{C_\tau} \frac{dC_\tau}{dx} = K_c \left(\left(C_{\tau EQ}^{1/2} + S_{VG} \right) - C_\tau^{1/2} \right) \quad (5.3)$$

In XFOIL and RFOIL, the equilibrium shear stress closure relation is defined within the *BLVAR* subroutine. This subroutine is called at every chordwise positions again. The *BLVAR* subroutine may be found in the *xblsys.f* code file and the *rbl.f* file for XFOIL and RFOIL, respectively.

5.3 Source Term Shape Function

Another important aspect related to the source term approach is the functional form of the source term. The source term will not be constant for every chordwise position but will be variant and defined by a function. In the article of Kerho and Kramer¹, it is proposed to use a source term shape that mimics the downstream decay in shed vorticity generated by a mixing device. Therefore, they obtained for a source term characterised by a step function at the location of the vortex generator which decays exponentially downstream. In the present work, a slight variant of this expression will be used. The reasoning behind it will be explained in this section.

As already stated earlier in this report, shed vortices decay when travelling downstream. Some work⁴⁵ has proven that vortices decay exponentially due to the presence of wall shear stress, boundary-layer turbulence and mutual interference between vortices. On the other hand, vortices shed by vortex generators do not suddenly appear. They need time to develop before they will reach their full initial strength.

Based on this reasoning, the source term functional form is slightly adapted when compared to the definition of Kerho and Kramer¹. The selected source term shape is given by Equation 5.4 where

the source term develops gradually before the exponential decay starts. This expression consists of three variables: the source term strength σ_0 , the decay rate λ and the location of the vortex generator. Note that the decay rate λ also influences how quickly the source term develops. In Figure 5.1 and Figure 5.2, a visual representation is given to demonstrate the effect of a varying strength and decay parameter. The functional dependency of the source term is implemented in XFOIL in the *xb/f* file while for RFOIL the adaptations are done in the *rb/03.f* code file.

Note that as a first step towards a robust integration of vortex generators within integral boundary-layer codes, the parameters of the source term shape function will be given as an input to the program. Further in this thesis, the purpose will be to determine these parameters automatically based on boundary-layer properties and the vortex generator geometry.

$$S_{VG} = \sigma_0 \cdot (x - x_{vg}) \cdot \exp(-\lambda(x - x_{vg})) \quad (5.4)$$

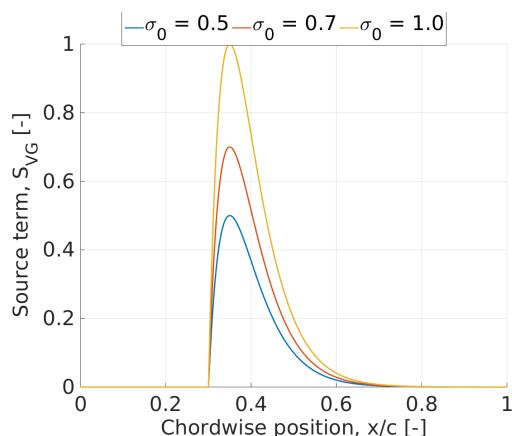


Figure 5.1: Source term with $\lambda = 20.0$, $x_{vg} = 0.3$ and varying strength

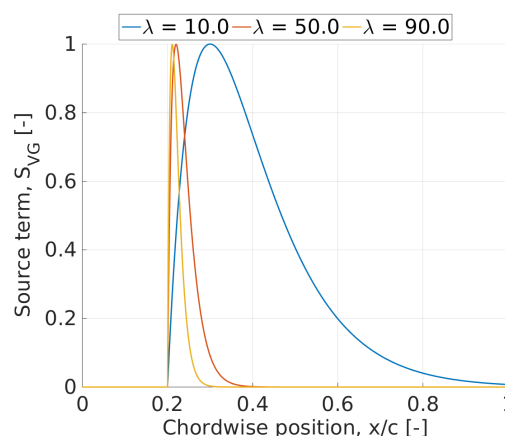


Figure 5.2: Source term with $\sigma_0 = 1.0$, $x_{vg} = 0.3$ and varying decay

5.4 Laminar-Turbulent Transition

The presence of a row of vortex generators might, but not necessarily, force the flow to transition from a laminar boundary-layer to a turbulent one. In the absence of vortex generators, XFOIL and RFOIL are using the e^N method that assumes that transition occurs when the most unstable Tollmein-Schlichting wave in the boundary-layer has grown by a given factor e^N , where N is usually assumed to be 9.¹

Although this works properly for natural transition, it is not true in case roughness or vortex generators are present. Therefore, Kerho and Kramer¹ have incorporated a transition prediction model intended to predict whether the vortex generators will promote bypass type transition or not. It decides using a VG roughness based Reynolds number, if the height of the vortex generator with respect to the boundary-layer thickness is sufficient to promote bypass transition. To clarify this more, a parallelism can be drawn to zig-zag tapes. In essence, zig-zag tapes can be seen as scaled down vortex generators. Zig-zag tapes are used to force the flow to transition from a laminar to a turbulent boundary-layer. However, if the height of the tapes is too small ($\ll 0.1\delta$), they might not be able to trigger transition.

Whether transition occurs or not for a particular vortex generator configuration is out of the scope of this thesis. Therefore, it is decided to use a simplified transition definition. This simplified model assumes that all vortex generators, independent of their configuration, are capable to transition the flow at the location of the vortex generators. It is expected that most cases that will be considered further in this thesis are indeed promoting transition, and therefore this assumption will not cause major problems.

XFOIL and RFOIL are adapted as such that when the vortex generators are positioned before the free transition location, the flow will automatically be forced to transition at the location of the vortex generators. This is illustrated by Equation 5.5. Fixing transition to the location of the vortex generators is realised by using the forced transition build in command.

$$x_{tr} = x_{tr,free}, \quad x_{tr,free} < x_{VG} \quad (5.5)$$

$$x_{tr} = x_{VG}, \quad x_{tr,free} > x_{VG} \quad (5.6)$$

5.5 Verification of the Code Modifications

To be sure that the source term approach is included properly within XFOIL and RFOIL and to prove that the source term approach is able to model vortex generators, it is necessary to verify the code. One way to do so is to study the boundary-layer properties. The effect that the source term has on these properties can be compared to the expected effects that need to occur to the boundary-layer properties when a vortex generator is present. This verification process of the code modification will be limited to quantitative comparisons since nothing is known yet regarding the magnitude of the source term.

5.5.1 Expected Effect on the Boundary-Layer Properties

The induced vortices shed by the vortex generators will modify the boundary-layer and consequently the integral boundary-layer properties. Examining the integral boundary-layer parameters allows to understand the state of the boundary-layer and the effect of mixing on the mean flow without becoming involved with the detailed flow processes. In the reference from Kerho and Kramer¹ and in the reference of Schubauer and Spangenberg³², very comprehensive descriptions are given regarding the boundary-layer parameters.

When discussing the effect of mixing due to vortex generators, it should be reminded that a relatively powerful self-mixing mechanism exist, namely turbulent flow. Turbulent flow mixes the slowly moving fluid near the wall with fast moving fluid further away, and in that way, the slow moving fluid is assisted to continue to move downstream. It is believed that a more vigorous mixing coming from for example vortex generators will behave similarly as the one naturally occurring. Therefore, analysing the effect of increased mixing to the boundary-layer properties can be observed as being analogous to the transition from laminar to turbulent flow.³²

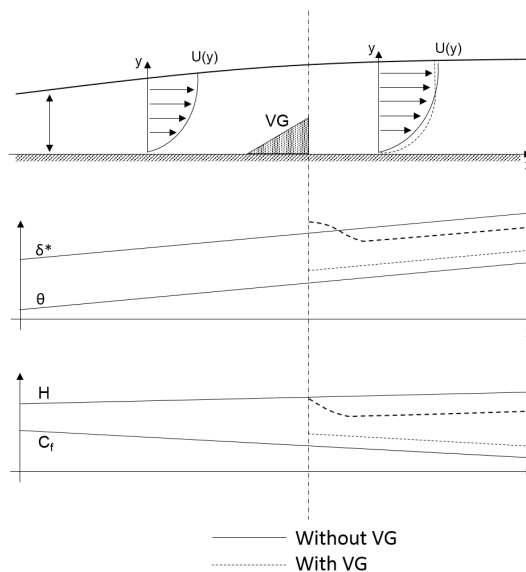


Figure 5.3: Effect of vortex generators on boundary-layer properties.¹

Bringing rapidly moving fluid closer to the wall will increase the momentum and the shear stress in the flow. A growth in the momentum thickness θ is thus expected not only due to the mixing itself, but also due to the price paid to generate the vortex.¹ Wall friction forces will rise meaning that the skin friction coefficient C_f goes up as well. In general, the retardation of the flow causes the displacement thickness to increase. However, when mixing occurs, the momentum loss will be more evenly distributed throughout the boundary-layer and the effect of retardation forces on flow displacement will be smaller. Mixing will affect the displacement thickness directly and will result in a smaller δ^* than compared to the case without additional mixing. This behaviour can be illustrated by considering the effect in terms of shape parameter H . As transition occurs from a laminar to a turbulent flow, it is well known that the

shape factor decreases. And since the distance in which turbulence is introduced is so short that the momentum thickness θ remains unchanged, δ^* should decrease compared to its original value.³²

To summarise, the increased fluid entrainment and mixing provided by the vortex generators will generally result in an increasing momentum thickness and a reduction to the displacement thickness. The shape factor will be decreased and the skin friction coefficient will increase. To illustrate these effects, Figure 5.3 is provided.^{1 32}

5.5.2 Verification Xfoil

For this verification process, the *DU93W210* airfoil is selected to be a representative case. The airfoil is considered at a Reynolds number of $1E6$ and at two angles of attack, one in the linear portion of the lift polar ($\alpha = 5^\circ$) and one after stall ($\alpha = 11^\circ$). A vortex generator is defined only at the upper side of the airfoil at a chord position of 40%. For both angles of attack, the results of three different source terms will be presented, of which the first case serves as a reference. The three different cases are:

- Case 1: $\sigma_0 = 0.00$, $\lambda = 150.0$ (no vortex generator)
- Case 2: $\sigma_0 = 0.05$, $\lambda = 150.0$
- Case 3: $\sigma_0 = 0.10$, $\lambda = 150.0$

In Figure 5.4, the source term corresponding to the three cases is plotted versus the chordwise position. The source term is zero in front of the vortex generator and given by Equation 5.4 behind it. For the first case, no vortex generator is defined, so consequently the source term is zero over the full chord length. It is clear that the maximum value of the source term corresponds to the strength σ_0 that is defined per case. Note that the source term is only computed at the panel nodes which lead to the fact that the source term graphs are not smooth especially around the peak.

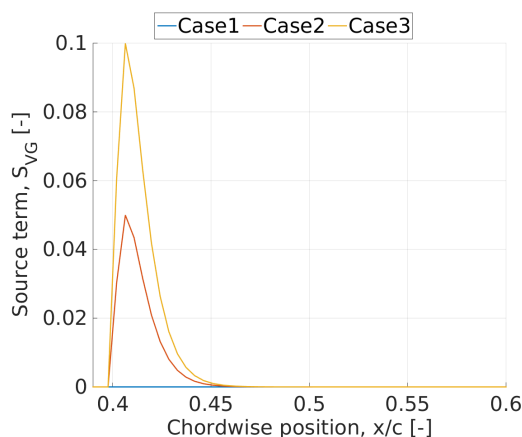


Figure 5.4: Source term versus chordwise position with $x_{vg} = 40\%$. Case 1: $\sigma_0 = 0.00$, $\lambda = 150.0$, Case 2: $\sigma_0 = 0.05$, $\lambda = 150.0$, Case 3: $\sigma_0 = 0.10$, $\lambda = 150.0$.

In Figure 5.5 and Figure 5.6, the boundary-layer properties are plotted versus the chordwise position for an angle of attack of 5° and 11° respectively. Again the three cases are shown. As expected, the larger the source term is, the larger the effect is on the boundary-layer properties. At the lowest angle of attack, the displacement thickness is almost unchanged due to the presence of the vortex generator while it decreases significantly at a high angle of attack. In the momentum thickness an increase can be recognised at both angles of attack, however, it is more pronounced at the angle of attack of 11° . Following from the displacement thickness and momentum thickness, the shape factor decreases. The velocity profile becomes fuller and is thus more resistant against separation. For the friction coefficient, in both cases an increase in friction can be recognised which could already be expected due to the

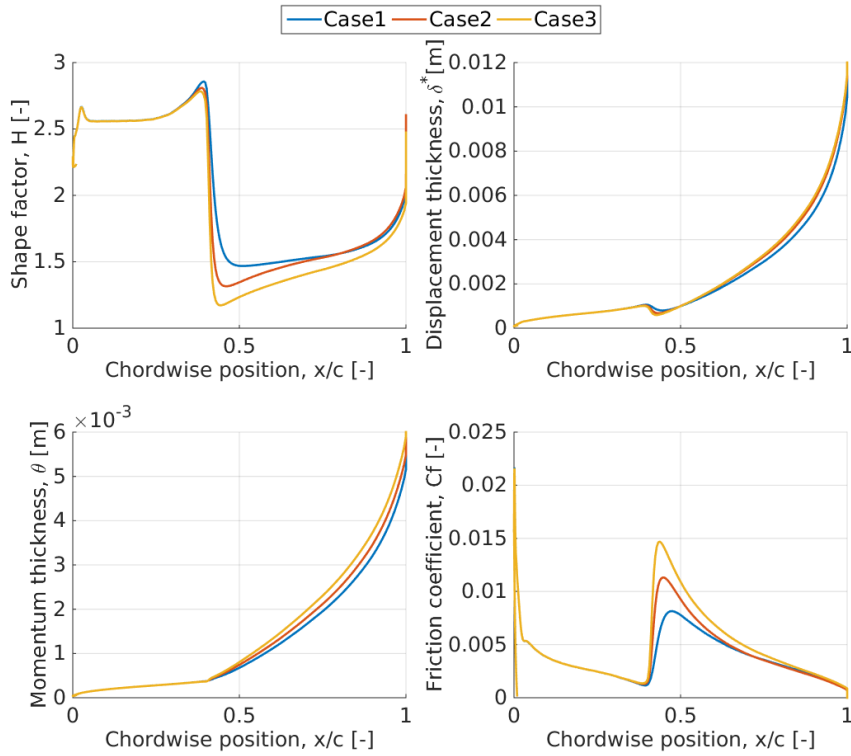


Figure 5.5: Boundary-layer properties versus chordwise position for the DU93W200 airfoil at $\alpha = 5^\circ$ and $Re = 1E6$ with $x_{vg} = 40\%$ using XFOIL. Case 1: $\sigma_0 = 0.00$, $\lambda = 150.0$, Case 2: $\sigma_0 = 0.05$, $\lambda = 150.0$, Case 3: $\sigma_0 = 0.10$, $\lambda = 150.0$

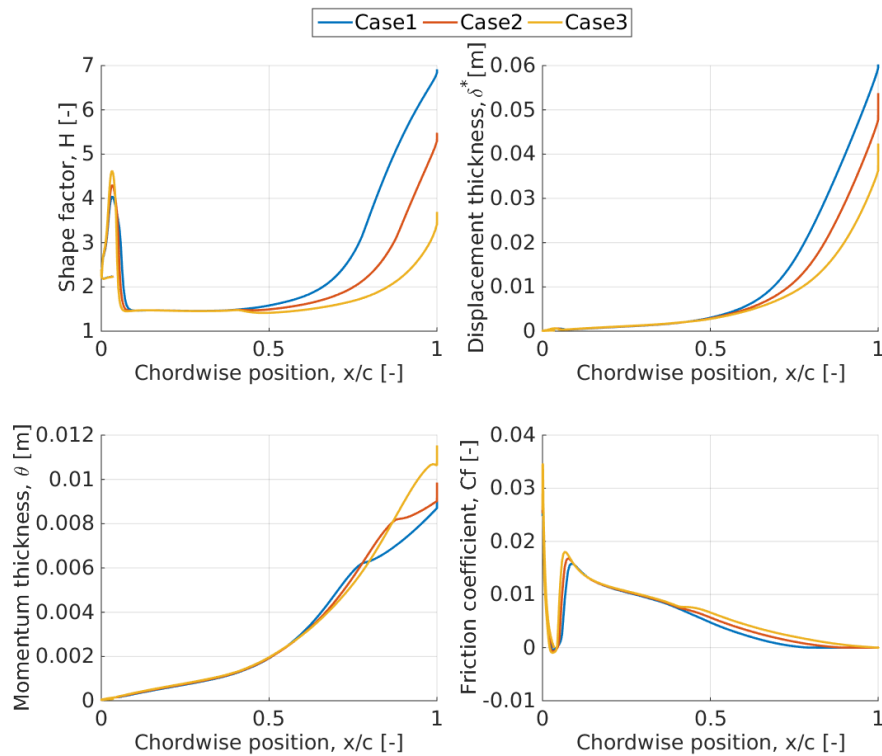


Figure 5.6: Boundary-layer properties versus chordwise position for the DU93W200 airfoil at $\alpha = 11^\circ$ and $Re = 1E6$ with $x_{vg} = 40\%$ using XFOIL. Case 1: $\sigma_0 = 0.00$, $\lambda = 150.0$, Case 2: $\sigma_0 = 0.05$, $\lambda = 150.0$, Case 3: $\sigma_0 = 0.10$, $\lambda = 150.0$

behaviour of the shape factor. From this, it can be concluded that the behaviour of the boundary-layer properties is in correspondence with the expectations. One additional remark should be made. At the angle of attack equal to 11° , transition already occurs very close to the leading edge, in front of the vortex generators. This free transition causes the sudden increase in shape factor and friction coefficient

cient. This is very clear from Figure 5.6. It appears that the exact location of transition depends on the source term strength. Altering the flow field behind the vortex generator also has an upstream effect, since the flow now sees a different airfoil shape due to the displacement effect.

Furthermore, Figure 5.7 and Figure 5.8 present a sensitivity study of the dissipation coefficient for both angles of attack, for three different source term strengths. For both the angle of attack before and after stall, an increase in dissipation at the location of the vortex generators itself is present. This again demonstrates that adding a source term to the equilibrium shear stress coefficient is similar to the method discussed by Kerho and Kramer¹. Note that the magnitude of the dissipation increment at the location of the vortex generators is larger for the case $\alpha = 5^\circ$ than for $\alpha = 11^\circ$ because at the smallest angle the vortex generators are also responsible for transition.

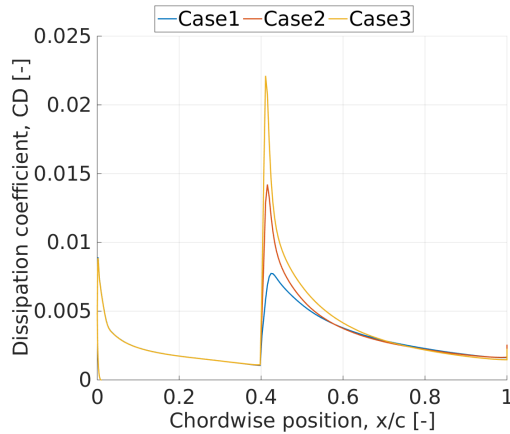


Figure 5.7: Dissipation coefficient versus chordwise position for the DU93W200 airfoil at $\alpha = 5^\circ$ and $Re = 1E6$ with $x_{vg} = 40\%$. Case 1: $\sigma_0 = 0.00$, $\lambda = 150.0$, Case 2: $\sigma_0 = 0.05$, $\lambda = 150.0$, Case 3: $\sigma_0 = 0.10$, $\lambda = 150.0$

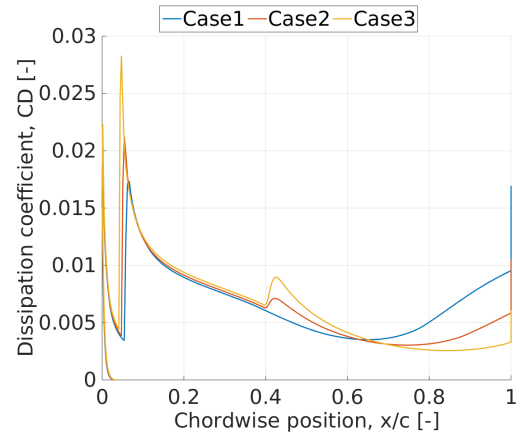


Figure 5.8: Dissipation coefficient versus chordwise position for the DU93W200 airfoil at $\alpha = 11^\circ$ and $Re = 1E6$ with $x_{vg} = 40\%$. Case 1: $\sigma_0 = 0.00$, $\lambda = 150.0$, Case 2: $\sigma_0 = 0.05$, $\lambda = 150.0$, Case 3: $\sigma_0 = 0.10$, $\lambda = 150.0$

Finally, lift and drag can be considered. Figure 5.9 and Figure 5.10 present the lift and drag polars. In each case separately, one source term is assumed for the whole angle of attack range. The graph shows that a vortex generator has only a small effect in the linear part while the effect becomes significant when the angle of attack increases above the clean stall angle. This follows the expectations as was already discussed before. Below the initial stall angle, vortex generators might decrease the lift and increase drag. For bigger source terms, the lift coefficient at zero angle of attack is smaller. This loss in lift is caused by larger momentum losses. On the other hand, the larger the source term is, the more the stall angle can be postponed and the higher the maximum lift coefficient is. Also the pressure drag is significantly reduced. This effect is thus beneficial and corresponds to the expectations of incorporating vortex generators.

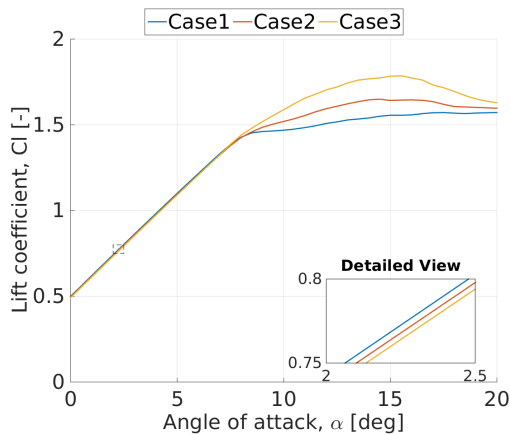


Figure 5.9: Lift polar of the DU93W200 airfoil at $Re = 1E6$ with $x_{vg} = 40\%$. Case 1: $\sigma_0 = 0.00$, $\lambda = 150.0$, Case 2: $\sigma_0 = 0.05$, $\lambda = 150.0$, Case 3: $\sigma_0 = 0.10$, $\lambda = 150.0$

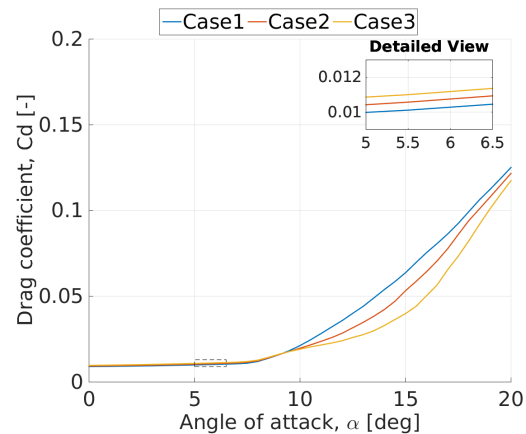


Figure 5.10: Drag polar of the DU93W200 airfoil at $Re = 1E6$ with $x_{vg} = 40\%$. Case 1: $\sigma_0 = 0.00$, $\lambda = 150.0$, Case 2: $\sigma_0 = 0.05$, $\lambda = 150.0$, Case 3: $\sigma_0 = 0.10$, $\lambda = 150.0$

5.5.3 Verification Rfoil

The modifications made to the boundary-layer formulation of RFOIL are verified by studying the boundary-layer properties for three different cases of which the first one serves as a reference.

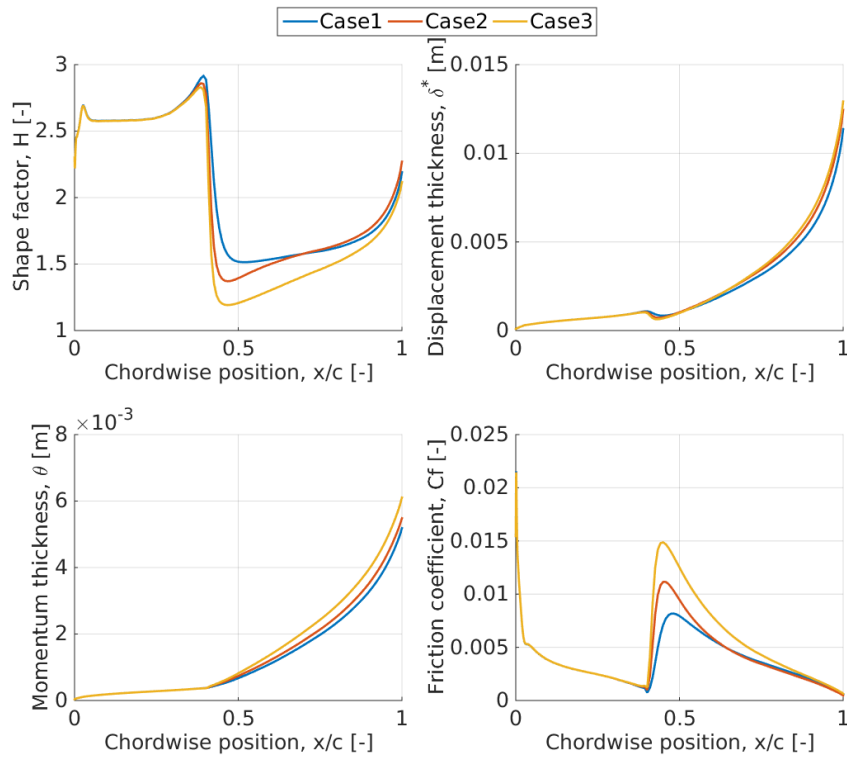


Figure 5.11: Boundary-layer properties versus chordwise position for the DU93W200 airfoil at $\alpha = 5^\circ$ and $Re = 1E6$ with $x_{vg} = 40\%$ using RFOIL. Case 1: $\sigma_0 = 0.00$, $\lambda = 150.0$, Case 2: $\sigma_0 = 0.05$, $\lambda = 150.0$, Case 3: $\sigma_0 = 0.10$, $\lambda = 150.0$

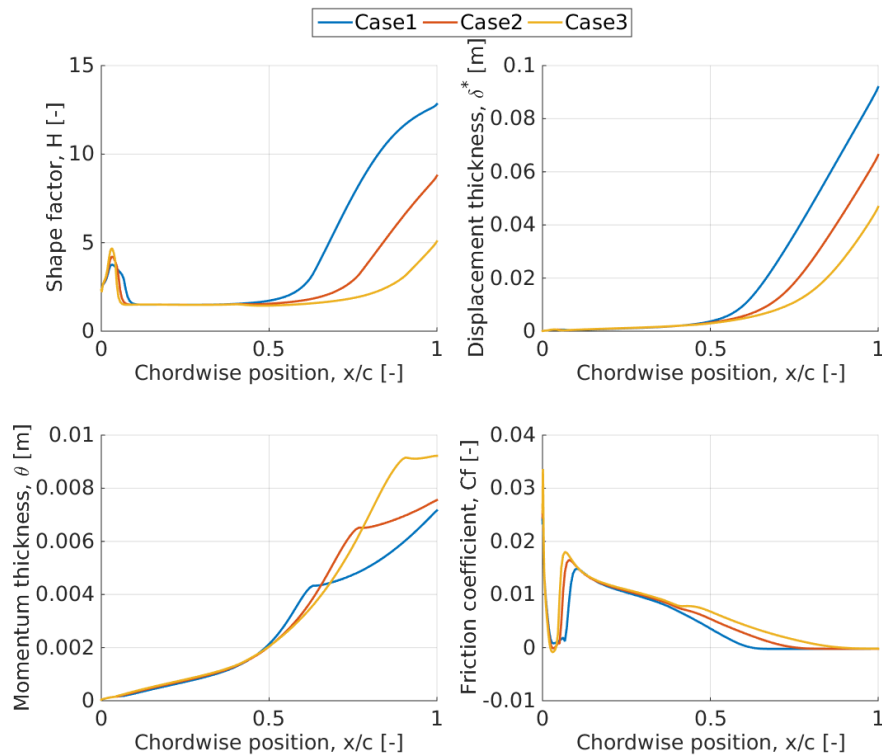


Figure 5.12: Boundary-layer properties versus chordwise position for the DU93W200 airfoil at $\alpha = 11^\circ$ and $Re = 1E6$ with $x_{vg} = 40\%$ using RFOIL. Case 1: $\sigma_0 = 0.00$, $\lambda = 150.0$, Case 2: $\sigma_0 = 0.05$, $\lambda = 150.0$, Case 3: $\sigma_0 = 0.10$, $\lambda = 150.0$

Figure 5.11 and Figure 5.12 made by using the modified RFOIL code, show the same trends as found by XFOIL. Especially at the low angles of attack, before stall, the boundary-layer properties show very similar values. After stall, the exact values differ slightly more which can be expected since the turbulent closure relations are different for both integral boundary-layer codes. Note again that at an angle of attack of 11° , transition occurs upstream of the location of the vortex generators. This is indicated by the sudden increase in shape factor and skin friction coefficient.

For RFOIL, conclusions can be drawn from the lift and drag polars and these are comparable with previous findings for the XFOIL code. Very similar trends can be recognised with, again, most influence of the source term at the higher angles of attack above the clean stall angle. For the XFOIL and RFOIL codes, the effect of the source term on lift and drag is within the same range. The differences in stall behaviour that both integral boundary-layer codes found can be explained by the different turbulent closure relations.

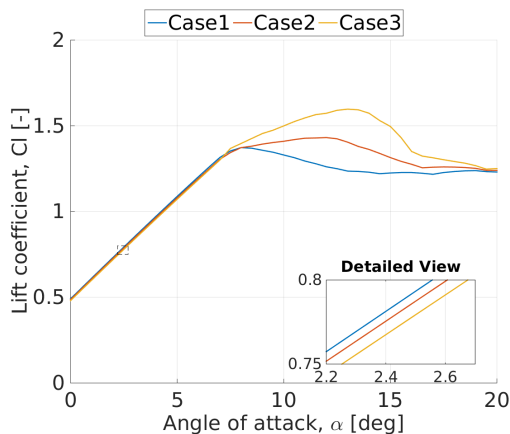


Figure 5.13: Lift polar of the DU93W200 airfoil at $Re = 1E6$ with $x_{vg} = 40\%$. Case 1: $\sigma_0 = 0.00$, $\lambda = 150.0$, Case 2: $\sigma_0 = 0.05$, $\lambda = 150.0$, Case 3: $\sigma_0 = 0.10$, $\lambda = 150.0$

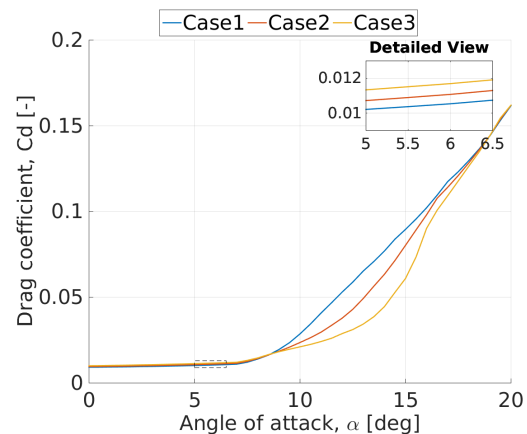


Figure 5.14: Drag polar of the DU93W200 airfoil at $Re = 1E6$ with $x_{vg} = 40\%$. Case 1: $\sigma_0 = 0.00$, $\lambda = 150.0$, Case 2: $\sigma_0 = 0.05$, $\lambda = 150.0$, Case 3: $\sigma_0 = 0.10$, $\lambda = 150.0$

6

Experimental and Numerical Reference Data

To be able to elaborate on the source term approach as a way to model vortex generators, it is necessary to gather reference data through which the effect of individual vortex generator parameters becomes clear. Therefore, a wind tunnel experiment is done led by D. Baldacchino as part of his PhD project. The set-up and equipment that is used during this experiment will be explained in section 6.2. Further in this chapter, the results of the experiment will be discussed. The data gathered from this experiment will be the main data set used to calibrate the integral boundary-layer codes including vortex generators. To enlarge the database of validation data, also data from external sources is gathered. In the last section of this chapter, more attention will be given to these additional data sets.

6.1 Experimental Set-Up & Equipment

The experimental results fully rely on the test set-up and equipment used. The different components such as the wind tunnel, airfoil model and measurement tools of the experiment will be discussed separately to convince the reader that the experiment is performed properly.

6.1.1 Wind Tunnel

The wind tunnel tests are performed in the Low Speed Low Turbulence wind tunnel (LTT) of Delft University of Technology. The LTT is an atmospheric tunnel of the closed-throat single-return type. It is driven by a six-bladed fan with a 525kW DC motor.⁸⁴

The wind tunnel has an octagonal test section with a width of 1.80m, a height of 1.25m and a length of 2.60m. Due to its powerful motor, it can reach a maximum test section velocity of approximately 120m/s. The maximum chord-based Reynolds number for 2D testing can go up to $3.5E6$. The wind tunnel can provide low levels of turbulence due to its high contraction ratio of 17.8 between the settling chamber and the test section. The free-stream turbulence level in the test section varies from 0.015% at 20m/s to 0.07% at 75m/s. In Figure 6.1, a schematic representation of the wind tunnel is given.⁸⁴

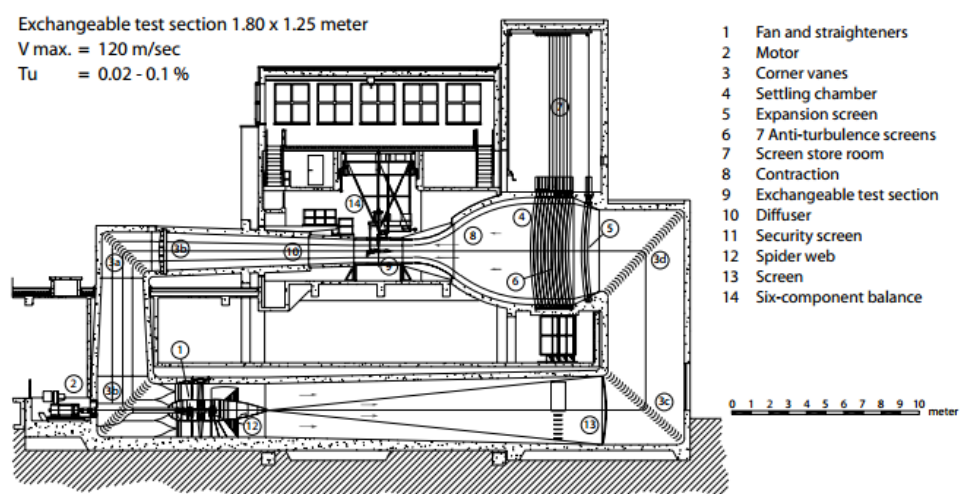


Figure 6.1: Schematic representation of the Low Speed Low Turbulence wind tunnel¹⁴

The standard wind tunnel testing equipment consists of fluid multi-manometers that can measure around 200 separate pressures, a 6-component balance, a 192 ports electronic pressure scanner system, hot wire anemometry and PIV systems. For flow visualisation purposes an infra-red camera system and normal DSLR cameras are available. Data are recorded using an electronic data acquisition system which are on-line reduced to relevant aerodynamic coefficients.⁸⁴

6.1.2 Airfoil Model

For the wind tunnel tests, an airfoil model was used with a chord length of 0.65m and a cross-section of the DU97W300 airfoil. This airfoil has a maximum thickness of 30% and had a thick trailing edge of 2% chord length. The airfoil profile is plotted in Figure 6.2. The DU97W300 airfoil is especially designed for wind energy applications. The design goals for this airfoil were⁸⁵:

- $C_{l_{max}}$ of 1.5 to 1.6 at $Re = 3E6$
- Location of maximum thickness around 30% of the chord
- Thick trailing edge of about 1.5% of the chord for structural reasons
- Designed for a wind turbine blade position around 40% span
- Smooth transition to DU91W2250
- Acceptable 2D roughness performance

The airfoil model is recovered from an older wind tunnel experiment performed by W.A. Timmer and R.P van Rooij⁸⁵ in 2003. Although the model is rather old, it should be remarked that it was still in very good shape. The model is fixed to a turning table and to obtain 2-dimensional airfoil characteristics, the model spans the whole height of the test section. The airfoil model is made out of fibre reinforced polymer and is provided with a polyester gel coat surface.

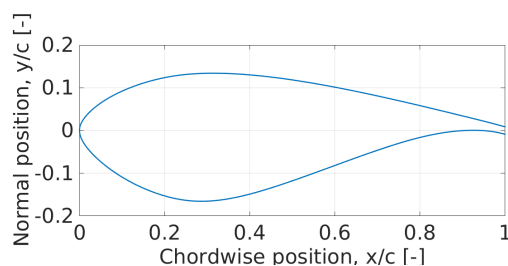


Figure 6.2: Cross section of the DU97W300 airfoil

6.1.3 Vortex Generators

The airfoil model is equipped with different vortex generator configurations, to study their effect. Parameters that are varied are the vortex generator shape, height h , length l , inflow angle β , external D and internal d pair distance and the position of the vortex generators x_{VG} with respect to the chord length c . The different parameters are indicated using a schematic representation in Figure 6.3. In the figure, a delta type vortex generator with a counter rotation orientation is shown. The vortex generators are made out of stainless steel. For easier handling of the vortex generators and to be able to quickly switch from one vortex generator configuration to the other, the individual vortex generators are attached to a strip of approximately 50cm. To do so, double-sided adhesive tape is used. The vortex generators are always placed over the whole length of the span.

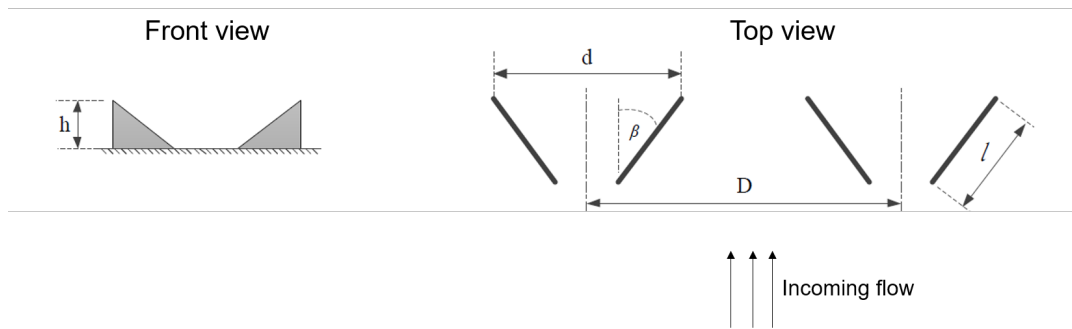


Figure 6.3: Schematic of the vortex generators

6.1.4 Zig-Zag Tape

In some test cases, the boundary-layer is tripped using zig-zag tape. The zig-zag tape has a thickness of 0.17mm and is, in case it is used, always positioned with its leading edge at 5% of the chord length on the upper surface. It is placed over the full span length. In Figure 6.4, a schematic representation is given showing the geometry specifications.

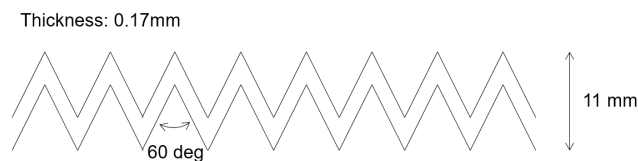


Figure 6.4: Schematic of the zig-zag tape

6.1.5 Pressure Measurement

The airfoil performance coefficients are obtained indirectly from model and wake pressure measurements. The airfoil model and the wake are provided with pressure tubes. The model is provided with 102 static pressure orifices with a diameter of 0.4mm and they are installed in staggered formation. The wake rake has 67 total pressure tubes and 16 static pressure tubes over a length of 504mm. The wake rake is able to traverse in spanwise direction such that average measurements can be taken that are representative for the full model. All pressure tubes (both static and total) are fed into a combining system and the measurements are recorded using an electronic data acquisition system. The results are further processed online using the laboratory computer.⁸⁵

The normal and tangential force coefficients, symbolised by C_n and C_t , and also the moment coefficients given by C_m are calculated from the model pressure distribution. The lift coefficient is consequently derived from the normal force C_n and the drag force C_d , and the underlying relation is given by Equation 6.1. The drag is generally computed from the wake rake results, however, in the post-stall region, the drag is computed from the airfoil pressure distributions.⁸⁵

$$C_l = \frac{C_n}{\cos \alpha} - C_d \cdot \tan \alpha \quad (6.1)$$

Similar to what is done by Timmer and Van Rooij⁸⁵, the standard correction method for model solid and wake blockage are used on the test section velocity and on the values of the static pressures.⁸⁵

6.1.6 Testing Procedure

In Appendix A, the test matrix of the experiment is presented. It contains all test cases and describes all the necessary parameters such that the experiment could be repeated. The goal of this thesis is not to present a detailed parametric study but mainly to use this data as validation for the developed code. For a detailed analysis of the parametric study, the reader is referred to upcoming papers of D. Baldacchino.

6.1.7 Set-up Pictures

In Figure 6.5 to Figure 6.8, pictures taken during the wind tunnel experiment are presented. In these pictures, the vortex generators and airfoil model are visualised.

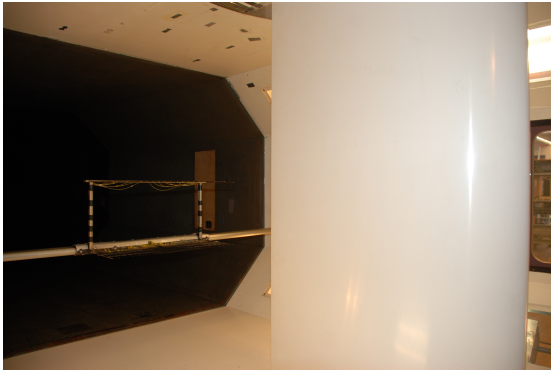


Figure 6.5: Airfoil model within the wind tunnel section, wake rake visible in background



Figure 6.6: Strip of vortex generators with different configurations



Figure 6.7: Details of vortex generator strip



Figure 6.8: Vortex generators installed on airfoil model

6.2 Experimental Results & Discussion

It is important for the continuation of this work, that it is well understood what the effect is of certain vortex generator geometrical parameters. Therefore, this section is provided. The focus of the results will lie on the effect of the aerodynamic polars when changing some geometrical parameters of the vortex generators, such as the height, inflow angle and chordwise position. Also a short discussion will be given about the spanwise pattern of the aerodynamic properties. Remember that it is not the purpose to discuss all the wind tunnel data sets, but only the data sets that are of importance for this thesis.

6.2.1 Height of the Vortex Generators

One of the geometrical parameters that has a significant effect on the aerodynamic properties, is the height of the vortex generators. In Figure 6.9 and Figure 6.10, the lift and drag polar are presented for three cases, namely the clean case where no vortex generators are installed, one case with vortex generators of height 5mm and a last case with vortex generators with a height of 10mm, both placed at 0.4c.

If the clean case is compared to the cases where vortex generators are present, one can see that the presence of the vortex generators has a beneficial effect on the stall angle and maximum lift coefficient. The effect on the linear part of the lift curve is rather small, while in the post-stall region the effect is significant. The presence of the shed vortices and the vortex generators itself increase the drag at the lower angles of attack. Since stall is postponed, the drag is reacting accordingly and thus decreased at high angles of attack.

The experimental results show that larger vortex generators are more effective than the smaller ones. The maximum lift coefficient is increased even further as well as the stall angle. Since the large vortex generators have a larger profile drag and generate more circulation, the drag is slightly higher at the angles of attack below stall.

Note that, when the vortex generators are positioned more towards the leading edge, the difference between the small and large vortex generators is smaller and could even be opposed. This can be related back to the boundary-layer thickness. Close to the leading edge, the boundary-layer is smaller compared to the boundary-layer thickness at chordwise positions more downstream. This means that

the vortex generator height to boundary-layer thickness increases moving upstream. Larger height to thickness ratios are in general beneficial considering maximum lift coefficient but at the same time introduce more drag. An optimum ratio exists at which both effects are balanced.

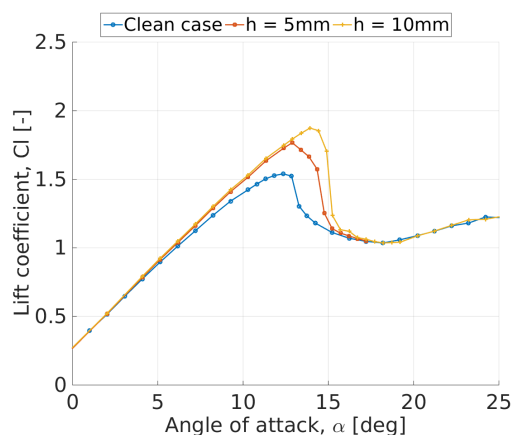


Figure 6.9: Lift polar of the DU97W300 airfoil at $Re = 2E6$ with $x_{vg}/c = 0.4$, $\beta = 15^\circ$ and varying height

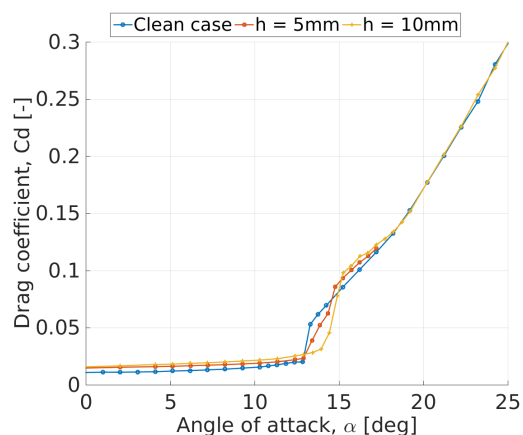


Figure 6.10: Drag polar of the DU97W300 airfoil at $Re = 2E6$ with $x_{vg}/c = 0.4$, $\beta = 15^\circ$ and varying height

6.2.2 Chordwise Position of the Vortex Generators

A second parameter that plays an important role in the effectiveness of vortex generators is the position of the vortex generators with respect to the chord length. In Figure 6.11 and Figure 6.12, the lift and drag polar are presented corresponding to the configuration where the smaller vortex generators with height 5mm are installed at 20, 30 and 40% of the chord length measured from the leading edge.

From these results, it is clear that the position of the vortex generators should be selected with care since it has a significant effect when considering lift and drag. In this specific case, it seems that placing the vortex generators at 30% chord position is most beneficial regarding the maximum lift coefficient. Based on the lift to drag ratio, the best location to put the vortex generators is at 40% of the chord. In this configuration, an L/D ratio of 80.4 can be reached. Besides that, the stall behaviour is much more gradual when positioning the vortex generators at 20%.

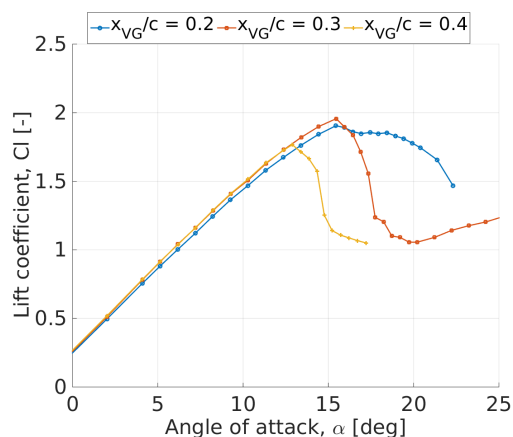


Figure 6.11: Lift polar of the DU97W300 airfoil at $Re = 2E6$ with $h = 5\text{mm}$, $\beta = 15^\circ$ and varying position

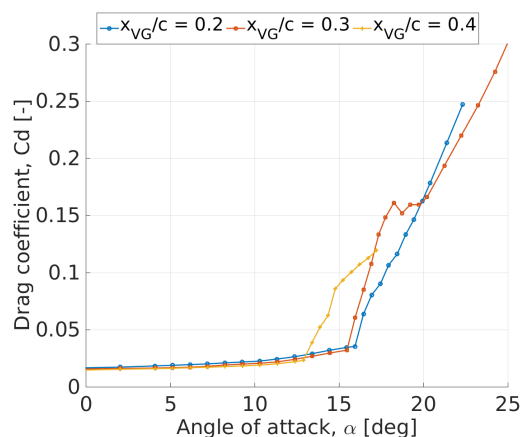


Figure 6.12: Drag polar of the DU97W300 airfoil at $Re = 2E6$ with $h = 5\text{mm}$, $\beta = 15^\circ$ and varying position

6.2.3 Inflow Angle of the Vortex Generators

The inflow angle of the vortex generator with respect to the free stream velocity is the next parameter that is considered in this discussion. The comparison of three different inflow angles, namely 12° , 15° and 18° , is given in Figure 6.13 and Figure 6.14.

In general, it is expected that the maximum lift coefficient would increase with increasing inflow angle until a certain point. The larger the inflow angle, the larger the circulation will be that is produced by the vortex generators and the more effect it will have on the airfoil performance. However, starting from a certain angle of attack, this is no longer true since the flow past the thin plates is expected to

separate right at the leading edge, introducing a significant increase in drag.³⁹ When now considering Figure 6.13 and Figure 6.14, the most beneficial situation for this airfoil in particular, corresponds to an inflow angle of 12° . In this situation, the lift to drag ratio is optimal when comparing the three different cases. Because the parameter range was limited to 12° , 15° and 18° , it can not be judged whether this is the true global optimum.

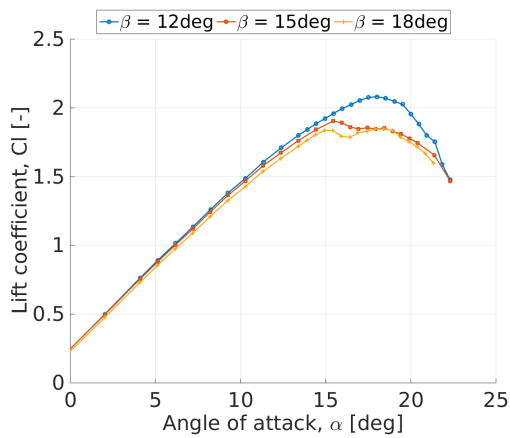


Figure 6.13: Lift polar of the DU97W300 airfoil at $Re = 2E6$ with $h = 5\text{mm}$, $x_{vg}/c = 0.2$ and varying inflow angle

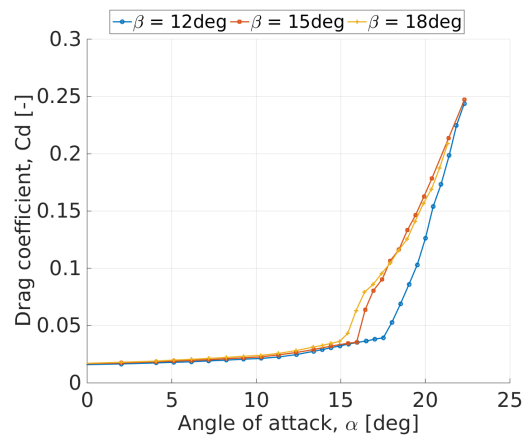


Figure 6.14: Drag polar of the DU97W300 airfoil at $Re = 2E6$ with $h = 5\text{mm}$, $x_{vg}/c = 0.2$, and varying inflow angle

6.2.4 Leading Edge Forced Transition

For wind energy applications, the aerodynamic characteristics of an airfoil suffering from roughness is a very important topic. Due to dust, insect accumulation or due to surface damage, the leading edge can be affected and this may have a significant effect on the aerodynamic performance of the airfoil. A way to imitate these phenomena is by forcing transition close to the leading edge by for example using zig-zag strips. With this in mind, it is important to consider how vortex generators behave when transition is forced.

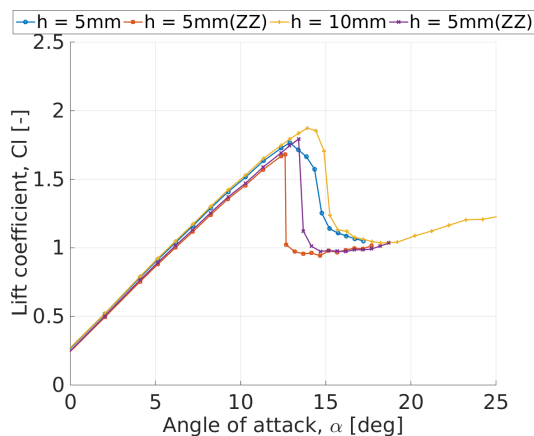


Figure 6.15: Lift polar of the DU97W300 airfoil at $Re = 2E6$ with $h = 5$ and 10mm , $\beta = 15^\circ$, $x_{vg}/c = 0.4$ with free and forced transition

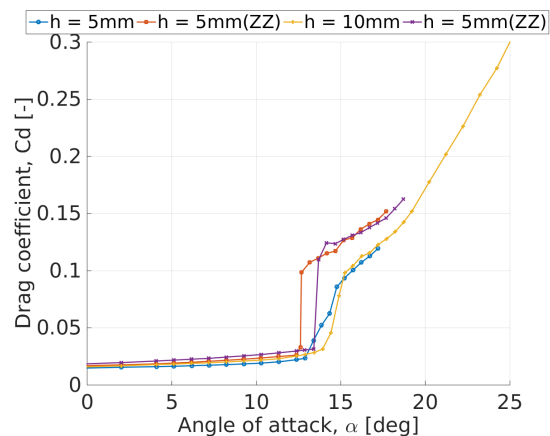


Figure 6.16: Drag polar of the DU97W300 airfoil at $Re = 2E6$ with $h = 5$ and 10mm , $\beta = 15^\circ$, $x_{vg}/c = 0.4$ with free and forced transition

In Figure 6.15 and Figure 6.16, lift and drag polars are provided in which a comparison is made between free and forced transition. The comparison is done for the situation where 5mm and 10mm vortex generators are positioned at 40% of the chord. In general, the presence of a zig-zag trip at a chordwise position of 5% leads to a decrease in stall angle and maximum lift coefficient. Also, it is remarkable that the DU97W300 in particular shows a much sharper and abrupt stall behaviour in case of forced transition compared to the free transition situation. The presence of the zig-zag tape introduces turbulence already in front of the vortex generators and this gives rise to additional drag. In the linear part of the lift curve, this additional drag penalty can be connected to the decrease in lift coefficient.

6.2.5 Three-Dimensional Flowfield

Due to the shed vortices and the physical presence of the vortex generator device itself, the aerodynamic properties at discrete locations along the span are not constant. As already explained earlier, the flow field of an airfoil equipped with a row of vortex generators is mainly three-dimensional. The three-dimensional behaviour of the vortex generators was also observed in this experiment.

A very qualitative way to look at a flow field is by using oil flow visualisation. This very valuable technique helps to identify important features such as limiting streamlines. In Figure 6.17, a picture taken during the wind tunnel campaign is shown. In this case the airfoil is set under a zero angle of attack and is equipped with small 5mm vortex generators at 20% of the chord. The dark spot around 20 percent of the chord, represents the location of the vortex generators. The shed vortices can be recognised as well as their downstream path. The flow is clearly three-dimensional and large flow variations can be recognised in spanwise direction. Starting from a chordwise position of 60%, the individual vortices seem to merge and the variations in spanwise direction seem to vanish out.

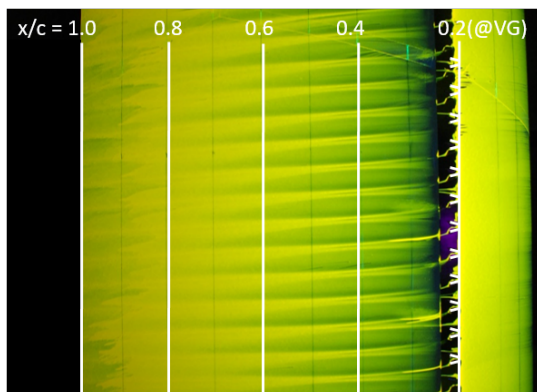


Figure 6.17: Flow visualisation of the DU97W300 airfoil equipped with vortex generators at $Re = 2E6$ and $\alpha = 0^\circ$

Besides the qualitative flow visualisation technique, the three-dimensional behaviour of the vortex generators can be proven by Figure 6.18, where the drag coefficient is plotted against the spanwise position. Over the spanwise direction, these properties are varying in a sinusoidal way. At the symmetry plane of a vortex generator pair, at the inflow region, the drag coefficient reaches its minimum. In this region, there is a strong downwash and the shape factor will decrease (fuller boundary-layer profile). In between two vortex generator pairs, in the so-called upflow region, the flow is actually moved away from the wall causing an additional momentum deficit. Due to this effect, the drag coefficient is reaching a maximum value at that spanwise location.

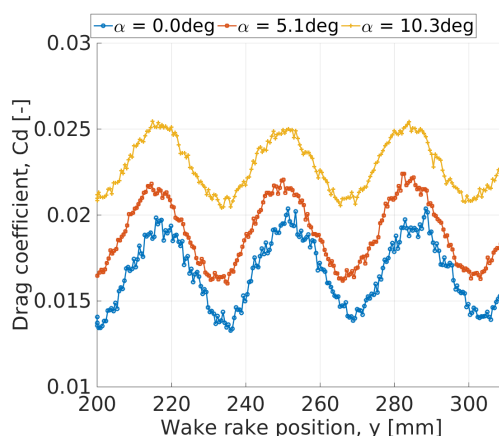


Figure 6.18: Spanwise Pattern of the drag coefficient of the DU97W300 airfoil at $Re = 2E6$ with $h = 5\text{mm}$, $x_{vg}/c = 0.2$ and $\beta = 5^\circ$

Integral boundary-layer codes such as XFOIL and RFOIL are two-dimensional codes, and therefore all boundary-layer properties as well as aerodynamic coefficients will be computed in a two-dimensional way. In the experiment, two-dimensional coefficients are obtained by analysing a range of three full

sinusoidal cycles. Averaging these results gives representative two-dimensional parameters. Two-dimensional results are very valuable since they give an indication of how an equivalent wing section would behave overall.

6.3 Additional Reference Data

The wind tunnel experiment provided very valuable data that can be used further in this work to integrate vortex generators within integral boundary-layer codes. However, this set of data limits to one airfoil model. To be able to build a robust code, as much validation data as possible needs to be obtained. Therefore, additional data sets are collected from different sources.

The first additional data set is one generated by W.A. Timmer and R.P. van Rooij⁸⁵. They have done wind tunnel experiments on the DU91W2250, DU93W210 and the DU97W300 airfoil equipped with counter rotating vane type vortex generators. The vortex generators had a height of 5 mm and were positioned at an inflow angle of 16.4° . The experiments are performed in the same TU Delft wind tunnel.

The second set of data originates from the *AVATAR* project⁸⁶. This project focusses on the aerodynamic modelling of large wind turbines with a rated power of 10MW and more, in which one of the work packages is focussing on the development and assessment of models for flow devices such as vortex generators. Within this work package, extensive CFD simulations are performed for a parametric study. The CFD simulations are conducted using many CFD codes amongst which the *Ellipsys* code. *Ellipsys* is an in-house flow solver developed by DTU that solves a discretization of the incompressible Reynolds Averaged Navier-Stokes (RANS) equations.⁸⁷ In this study, two different airfoils are considered, namely the FFAW3333 and the DU331 airfoil. Vortex generators with varying heights, location, inflow angles, internal and external distance are studied.

An additional data set is made available for a separation control study which was performed by M. Manolesos et al.⁸⁸ He performed an experimental study of 3D separation and separation control. He performed experiments in the wind tunnels of the National Technical University of Athens. In this study an 18% thick NTUA airfoil was used and equipped with counter rotating upwash vane type vortex generators. The vortex generators had a height of 6mm and were positioned at an angle of 20° with respect to the free stream flow.

The available data set spans different airfoil families at a wide range of Reynolds numbers. The airfoils are equipped with different vortex generator configurations and analysed. In Appendix A, tables are provided that sum up all the available data sets that will be used in this thesis. It contains all necessary flow properties and configuration parameters.

7

Source Term Empirical Relation

As explained before a source term approach is used to integrate vortex generators within the integral boundary-layer theory. An additional term is added to one of the closure relations and a verification process has shown that this additional term is able to capture the effect of a vortex generator. However, the exact value of the extra term for a specific airfoil/vortex generator configuration still needs to be determined. It is expected that the value of the source term is not just a constant, but that it will depend on the vortex generator configuration. The methodology to calibrate this source term will be explained in this chapter. In the first section of this chapter, the source term calibration procedure will be explained. Further, section 7.2 explores relations between the optimal source terms found for every case and the case specific properties. An empirical relation will be determined that may predict the required source term depending on the vortex generator geometry and boundary-layer properties. At the end of this chapter, it is shown how this empirical relation is implemented into XFOIL and RFOIL.

The work presented in this chapter is very novel. A thorough calibration of the source term is performed with the ultimate goal to relate that source term to the vortex generator geometry and the boundary-layer parameters.

7.1 Source Term Calibration Process

The source term shape function that has been selected to best mimic the shed vortex of the vortex generator is one that is gradually developing and continuously decaying exponentially. The source term shape function describing this behaviour consists of three variables: the unknown source term strength σ_0 and the decay rate λ and the known location of the vortex generator x_{vg}/c . These first two parameters (σ_0 and λ) need to be determined. It is expected that the value of these two parameters are not constant and are depending on the airfoil/vortex generator configuration. Therefore, a calibration process is set up, such that for every reference point, meaning for one defined vortex generator configuration installed on that particular airfoil under specifically set flow conditions, an optimal source term can be defined. This calibration process consists of three main steps. First of all, a brute-force optimisation approach is applied to analyse the effect of the source term on lift and drag properties. Secondly, the target aerodynamic properties need to be defined. In the last step, the results of step one and two are combined to finally determine the optimal source term. The details of this calibration method will be explained in this section step by step. To start, some terminology needs to be introduced. Throughout this chapter, a distinction will be made between an airfoil with and without vortex generators. The case where no vortex generators are installed is referred to as the *clean case*. An airfoil equipped with vortex generators is called the *vortex generator case*.

The explanation of the calibration process will be supported with one elaborated example. The case that will be considered is a DU97W300 airfoil equipped with vortex generators at 30% chord. The vortex generators have a height of 5mm, a length of 15mm and are under an inflow angle of 15° . The chord-based Reynolds number is $2.0E6$ and the angle of attack ranges from -4° to 20° . This example is proven to be representative for the whole reference data base.

7.1.1 Optimisation Approach

The first step of the calibration is analysing the effect of adding different source terms. It should become very clear how the XFOIL and RFOIL codes react on a certain source term input and to do so, a *brute-force approach* will be used. The brute-force approach is a very basic optimisation method where all possible input combinations are analysed separately. Although it is a rather time-consuming method, this method is found very suitable for this specific problem. It is very simple and effective and allows to gain a good understanding in the effect of the source term strength and decay factors.

To start the brute-force approach, a suitable range of source term strength and decay values is selected. Consequently, all possible combinations of these two parameters are set up. Every combination of these two parameters prescribes a different source term function. The various source term functions are input to the integral boundary-layer codes and the boundary-layer properties and aerodynamic properties are calculated. Remember that XFOIL and RFOIL are adapted as such that the strength and decay values are still inputs to the program. This makes it very easy to adapt the source term shape function.

To clarify this brute-force procedure, an example will be brought into the discussion. In Figure 7.1 and Figure 7.2, the lift and drag coefficients corresponding to all possible combinations of source term strength and decay are presented. On the x and y axis, the strength and decay ranges are indicated. The colors indicate the value of the lift and drag coefficient, where yellow refers to large values and blue to smaller ones. The results are generated for three different angles of attack separately.

Different observations can be made from these graphs. First of all, remark that the effect of increasing the source term strength and decay is different depending on the angle of attack. Increasing the strength and decay parameters at low angles of attack (e.g. $\alpha = -0.038^\circ$) results in a decreasing lift coefficient and increasing drag coefficient. At high angles of attack (e.g. $\alpha = 15.458^\circ$) the opposite is true: lift increases and drag decreases. Also, adding a source term into the low angles of attack region is less significant than when a source term is applied to the high angles of attack region. This is very clear by considering the scale indicated on the colour bars. For a similar range of strength and decay values, the lift coefficient for $\alpha = -0.038^\circ$ ranges only over an order $10E-3$. For $\alpha = 10.287^\circ$, the lift coefficient spread with one order more while the lift coefficient can be increased with approximately 0.5 at $\alpha = 15.458^\circ$. A similar observation is made in the drag coefficient. As a final remark, XFOIL and RFOIL do show convergence problems when the source term becomes too large. Especially at low angles of attack, this might cause some problems in the future and this will be discussed later in this report.

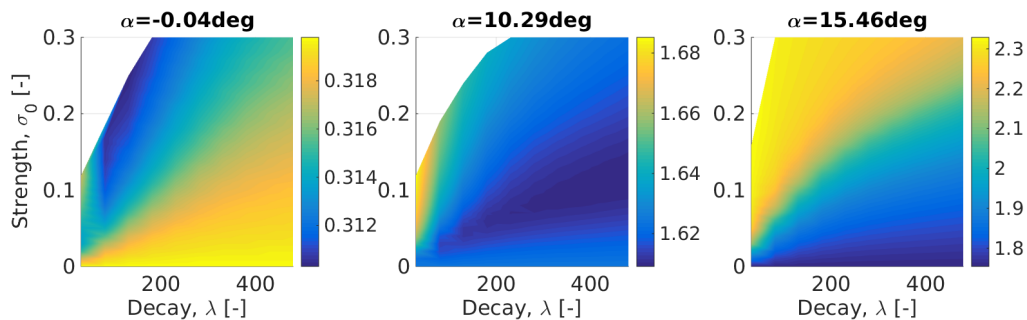


Figure 7.1: Variation of lift coefficient for a range of strength and decay values.

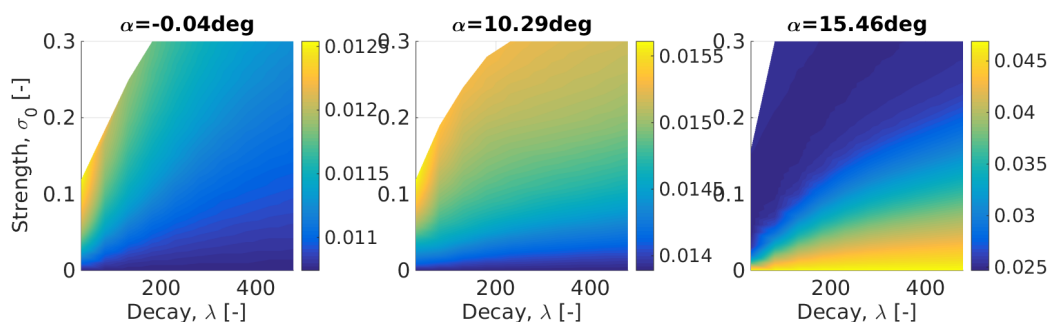


Figure 7.2: Variation of drag coefficient for a range of strength and decay values.

Considering the above figures, one may ascertain that multiple combinations of source term strength and decay predict the same lift and drag coefficient. It has been established that all these combinations of strength σ_0 and decay λ constants have in common that their prescribed integral is equal. This source term integral, symbolised by I_{st} , is defined by the area enclosed by the source term function. The integral is numerically determined based on the airfoil panelling using the trapezoidal rule, and is given by Equation 7.1. N represents the number of panels on the top-side of the airfoil. Introducing

the source term integral made it possible to reduce the number of unknowns from two (strength σ_0 and decay λ) to one and thus simplify the problem.

$$I_{ST} = \int_0^c f_{ST}(x) dx \quad (7.1)$$

$$\approx \sum_{i=1}^{N-1} (x_{i+1} - x_i) \left(\frac{f_{ST}(x_{i+1}) + f_{ST}(x_i)}{2} \right) \quad (7.2)$$

$$\text{where: } f_{ST}(x) = \sigma_0 \cdot (x - x_{vg}) \cdot \exp(-\lambda(x - x_{vg})) \quad (7.3)$$

The fact that all source terms with the same integrals are predicting the same aerodynamic properties implies that the effect of the source term is independent of what the specific value of the strength and decay parameters are. This could imply that the source term is representing a kind of energy increment introduced by the presence of the vortex generators. This statement could be supported by a dimensional analysis. The source term is added to a shear stress parameter meaning that the source term should have the same unit as the parameter it is added to. Shear stress is given by a force per area (chord times span) or in a 2 dimensional case as a force per unit chord length. Therefore its unit is $[N/m]$. The integral of the source term with respect to the chordwise direction has thus a unit of $[N/m \cdot m]$. This is similar as $[J/m]$ or energy per unit chord length. The source term integral is in that sense representing how much energy per unit chord length is added by the vortex generators.

$$\int_0^c S_{VG}(x) dx = \left[\frac{N}{m} \cdot m \right] = \left[\frac{J}{m} \right] \quad (7.4)$$

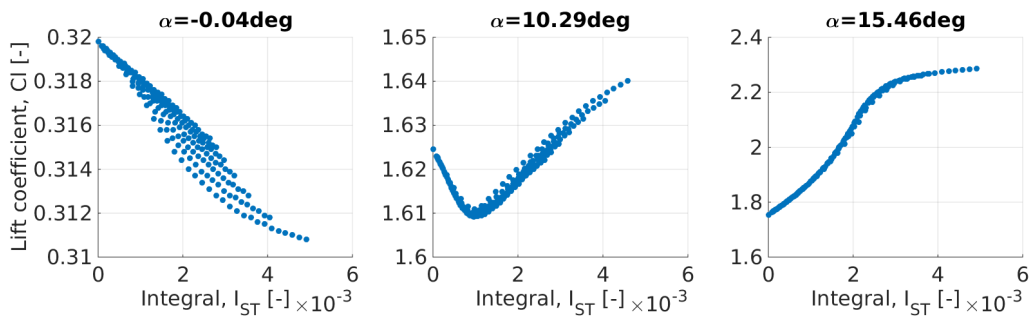


Figure 7.3: Variation of the lift coefficient with the source term integral.

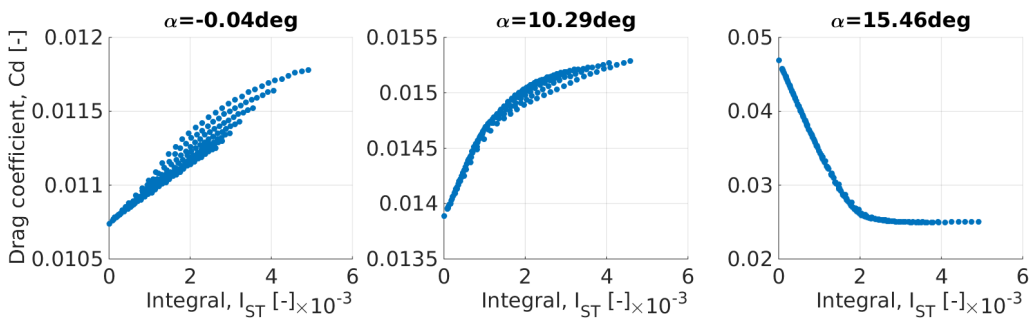


Figure 7.4: Variation of the drag coefficient with the source term integral.

To further discuss this matter, the same example is continued. The source term strength and decay parameter are now combined into the source term integral. In Figure 7.3 and Figure 7.4, the lift and drag coefficient is plotted versus the source term integral. The same angles of attack are considered as before, namely -0.038° , 10.287° and 15.458° . From this graph, it is clear that the lift and drag coefficient corresponding to one specific source term integral but resulting from a different combination of strength and decay parameters, are very similar. One could argue that at the lower angles of attack, this is not valid since the data points seem to be spread more than at higher angles of attack. However, this should be put in perspective because the range of lift and drag coefficient indicated on the y-axis is almost two orders less at these lower angles of attack than at high angles of attack. In conclusion, reducing the unknowns from two (source term strength and decay) to one (source term integral) is a valid assumption.

7.1.2 Target Lift Polar

In the second step of the source term calibration method, the aerodynamic properties expected to be found by the airfoil codes need to be determined. What are the lift and drag coefficients that XFOIL and RFOIL should predict ideally? One may say that the expected aerodynamic properties are the ones found by analysing a specific vortex generator case in an experiment or using CFD calculations, but this should not necessarily be true. The reasoning behind this statement will be explained.

XFOIL and RFOIL are not perfect codes, even not in clean case, meaning when no vortex generators are added. The lift and drag coefficients found by experiments or CFD calculations for a clean airfoil are in average well predicted by XFOIL and RFOIL but still significant differences exist. Differences are present in maximum lift coefficient, stall angle and lift slope. Also the post-stall behaviour (especially of XFOIL) misses some accuracy and drag is most often underestimated.

The goal of this thesis is to model vortex generators. It is really the purpose to predict as accurately as possible the effect of adding vortex generators compared to the clean case. More specifically, the source term should thus not additionally try to correct for the error of the code already existing in clean case. Therefore it is decided, after a careful investigation, that it would be beneficial to transform the measurement data using a correction factor as such that it takes into account the differences existing in clean case between the codes on one hand and measurement data on the other. Major attention is given to the lift curve slope, since this seems to be the most significant problem. Airfoil codes often overestimate the lift curve slope and by applying a correction factor for it, the effect of this error can be accounted for.

To clarify how the lift polar transformation is performed, the same example as used before will be further elaborated. First consider the clean curves shown in Figure 7.5. In this graph, the lift polar of the DU97W300 in clean conditions at a Reynolds number of $2.0E6$ is plotted for the measurement data and for the XFOIL code. Clear differences are visible between both curves in maximum lift coefficient, stall angle, post-stall behaviour and the lift curve slope. Focus now on the lift curve slope. It is estimated by extrapolating both clean curves that they intersect at an angle of attack of -8.4829° and a lift coefficient of -0.85 . The slope difference is determined consequently to be $8E-3\text{rad}$.

If now the measurement data of the vortex generator case is brought into the picture, as presented, the effect of the vortex generator becomes clear. Below an angle of attack of 3° , the lift coefficient is slightly decreased. Above that angle, the effect of the vortex generators becomes positive when considering the lift. This is mainly true since the lift curve slope is increased compared to the clean airfoil situation. Starting from the angle at which the clean airfoil initiates to stall (around 10°), the lift polar with vortex generators begins to diverge from the clean case and the vortex generators prove their functionality.

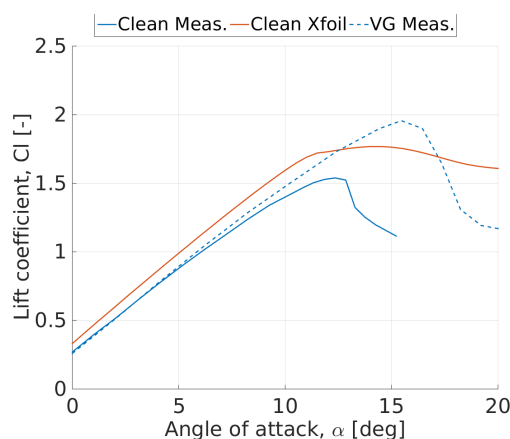


Figure 7.5: Lift polar of a clean DU97W300 at $Re = 2.0E6$ calculated using XFOIL and measurement data and the measurement data of the vortex generator case.

Because of the differences between the measurements and the XFOIL/RFOIL codes in clean case, it should not be the goal to compare the vortex generator predictions with the measurement data. This would otherwise imply that the presence of the vortex generators decrease the lift coefficient with a significant amount up till an angle of attack of around 12° , while the measurement data clearly showed

that this is not corresponding to the real effect of the vortex generators. The optimal source term would in that case be correcting for both the effect of the vortex generators and the error already present in clean conditions, which is definitely not the purpose.

Therefore, an artificial lift polar will be introduced and this curve will be referred to as the *target curve*. The measured lift polar will be transformed using a lift curve slope correction. The lift slope is increased with the same difference as was present in the clean case between the measurement and code data. If the lift slope is increased, consequently also the maximum lift coefficient will be slightly increased and the stall angle decreased. In this particular example the slope error was estimated to be $8E-3$ rad measured around a rotation point at -8.4829° angle of attack. The result of applying this transformation on the measured VG data is presented in Figure 7.6. In this graph, the lift coefficient is plotted versus the angle of attack. The blue lines represent the measurement data in clean case (full line) and with vortex generators (dashed line). The red full line indicates how XFOIL predicts the aerodynamic performance of the clear DU97W300 airfoil at a Reynolds number of $2.0E6$. The red dashed line refers to the artificial target curve. This target curve is, according to the author, much more representative and realistic to be found by the airfoil code and will thus be used to identify the optimal source term, hence, the optimal source term will be the one that causes the closest match with the artificial lift polar.

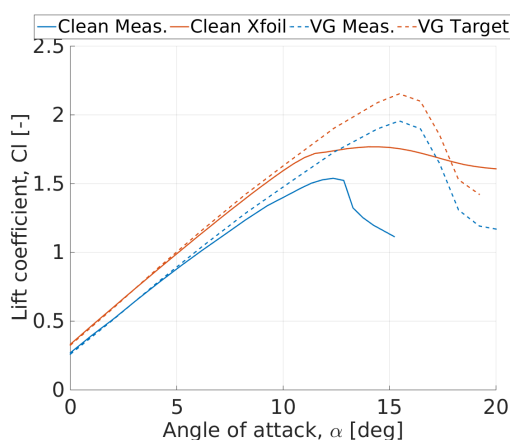


Figure 7.6: Lift polar of the DU97W300 at $Re = 2.0E6$ with and without vortex generators as well as the introduction of the target lift polar.

7.1.3 Optimal Source Term

The last step in the calibration process is the actual identification of the optimal source term. In this final step, the results of the previous two steps are combined. From the brute-force approach, the relation between the lift and drag coefficients and the source term integral is established. And from the target lift polar, the lift coefficient that is aimed for to be obtained by XFOIL/RFOIL may be specified. Combining these two results allows to identify the optimal source term. The results of the example considered throughout this section are presented in Figure 7.7.

One remark still needs to be made. The determination of the optimal source term will be mainly based on the lift coefficient. The drag coefficient or any other boundary-layer parameters will not be considered and this decision is supported by several reasons. First of all, integral boundary-layer codes often underestimate drag. On top of that, the drag below the stall angle is hardly changing in the presence of the source term. The effect is so little compared to the error already existing in clean case that the drag coefficient seems to be an unreliable parameter. The source term approach, as it is considered right now, is not taking into account the additional profile drag of the vortex generators itself. The device geometry and in case of the experiments also the strip to which the vortex generators were attached, introduce a significant amount of drag that is not accounted for in the codes. Note that in a further stadium, including the additional profile drag into the codes could be realised. For a more detailed discussion of this, the reader is referred to chapter 9 further in this thesis. The reason why boundary-layer parameters such as boundary-layer thickness or shape factor are not selected in the optimisation criteria is that these parameters are hard to be measured during an experimental campaign. Due to this, the availability of boundary-layer information is very limited. On top of that, boundary-layer parameters vary in chordwise direction due to the three-dimensional flow field, making an optimisation more difficult. Based on the above mentioned reasons, the author believes that given

the available dataset and code limitations, lift is the best suited quantity to determine the source term.

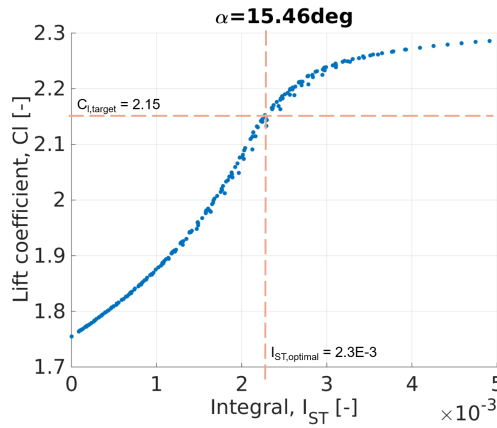


Figure 7.7: Identification optimal source term.

7.1.4 Summary of the Calibration Process

The above explained calibration process is summarised in Figure 7.8. This figure presents a scheme in which all the different steps that needs to be made to identify the optimal source term are presented. The calibration process can be subdivided into three parts: the source term influence, the target lift curve and the optimal source term. The first two parts can be performed simultaneously while the third step, the determination of the optimal source term, results from the previous two.

The calibration method is applied to every data set detailed in Appendix A. Every angle of attack for which a measurement point was provided is analysed separately and has its own optimal source term. In total 968 optimal source terms are identified.

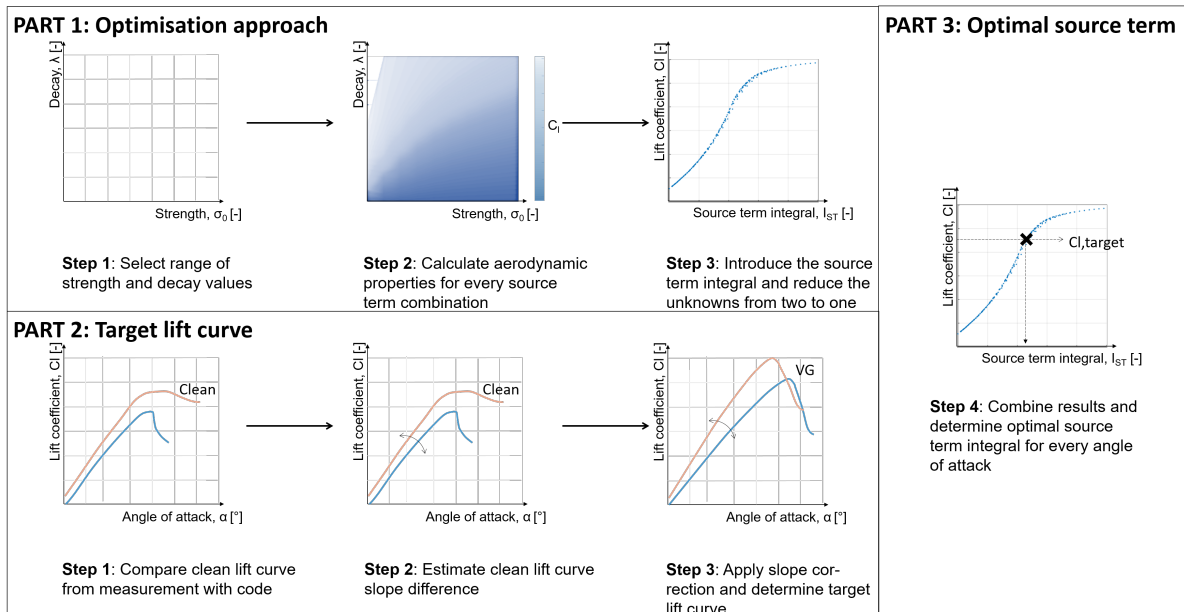


Figure 7.8: Illustration of the brute-force solution of the source term problem.

7.2 Source Term Regression

A large data set of optimal source terms is gathered, all specifically determined for one airfoil/vortex generator configuration. In future cases, however, measurement data or CFD calculations will no longer be available and thus it will not be possible any more to calibrate the source term by using the above explained methodology. A relation needs to be found such that the magnitude of the source term can be predicted for a new airfoil/vortex generator configuration in advance without the presence of any reference data. Therefore, an empirical relation will be set up that relates the value of the source term to vortex generator geometry parameters and boundary-layer parameters. How this is done will

be discussed in this section. The final source term relations for both XFOIL and RFOIL will be presented and discussed.

7.2.1 Multiple Variable Linear Regression Approach

The approach that will be used to set up an empirical relation for the source term is the multiple variable linear regression approach. But before that this approach is applied to the source term case, the theory will be introduced.

Linear regression is one of the fundamental models in statistics used to determine the relationship between dependent and independent variables.⁸⁹ A simple linear combination of independent variables x_k is assumed to represent the dependent variable y . The general expression for k independent variables and n data points is given by Equation 7.5.

$$Y_i = C_0 + C_1 \cdot X_{i1} + C_2 \cdot X_{i2} + \dots + C_k \cdot X_{ik} + \epsilon_i, \quad i = 1, 2, \dots, n \quad (7.5)$$

This problem can be easily rewritten by introducing matrices. In Equation 7.6, the regression equation is written in matrix notation.⁸⁹

$$\underbrace{\begin{pmatrix} Y_1 \\ Y_2 \\ \vdots \\ Y_n \end{pmatrix}}_y = \underbrace{\begin{pmatrix} 1 & X_{11} & \dots & X_{1k} \\ 1 & X_{21} & \dots & X_{2k} \\ \vdots & \vdots & \ddots & \vdots \\ 1 & X_{n1} & \dots & X_{nk} \end{pmatrix}}_X \underbrace{\begin{pmatrix} C_0 \\ C_1 \\ \vdots \\ C_k \end{pmatrix}}_c + \underbrace{\begin{pmatrix} \epsilon_1 \\ \epsilon_2 \\ \vdots \\ \epsilon_n \end{pmatrix}}_e \quad (7.6)$$

Using the least-square method, the best combination of C_0, C_1, \dots, C_k may be determined such that the sum of the squares of $\epsilon_1, \epsilon_2, \dots, \epsilon_n$ is minimised. The sum of the error squared can be expressed in matrix form by Equation 7.7 where small letters refer to vectors and capital letter indicates a matrix.⁹⁰

$$J(c) = e^2 = e^T e \quad (7.7)$$

$$= (y - Xc)^T \cdot (y - Xc) \quad (7.8)$$

$$= y^T y - y^T (Xc) - (Xc)^T y + (Xc)^T (Xc)$$

$$= y^T y - 2c^T X^T y + c^T X^T X c$$

These least-square estimators are obtained by minimising J , or by setting the derivative of it equal to zero. This equation, given by Equation 7.10, is called the least-squares normal equation.⁹⁰

$$\frac{\partial J}{\partial c} = -2X^T y + 2X^T X c = 0 \quad (7.9)$$

$$X^T X c = X^T y \quad (7.10)$$

Rewriting this equation, allows to find the regression coefficients. The final solution is given by Equation 7.11. Note that it is assumed that all variables x_1, x_2, \dots, x_n should be linearly independent such that the inverse of $X^T X$ exists.⁸⁹

$$c = (X^T X)^{-1} X^T y \quad (7.11)$$

The multiple variable linear regression method can be extended further by introducing a weight matrix W . In this matrix, the importance of a particular data point can be specified. The higher the weight, the more the data point will weigh and the more it will be taken into account when determining the regression constants. The weight matrix W is a diagonal matrix where the weights are specified on the diagonal and all other elements are zero. In Equation 7.12, the weight matrix is added to the solution equation. The use of the weight matrix is illustrated in Figure 7.9.

$$c = (X^T W X)^{-1} X^T W y \quad (7.12)$$

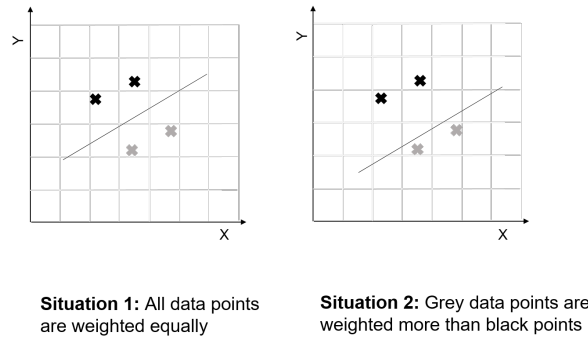


Figure 7.9: The use of a weight matrix in a linear regression approach.

7.2.2 Source Term Linear Regression

The multiple variable linear regression approach will be applied to the source term case in order to produce an empirical relation presenting the dependency of the source term integral with vortex generator geometry and boundary-layer properties. In general, an expression needs to be found such as Equation 7.13.

$$I_{ST} = f \left(\underbrace{h, l, d, D, \beta}_{\text{VG configuration}}, \underbrace{\delta, \theta, U_e}_{\text{BL properties}} \right) \quad (7.13)$$

However, performing a linear regression with so many independent variables is impractical. Basically, every kind of solution can be fitted through the data points if the data base is not large enough. Therefore some of the independent variables will be disregarded from the regression equation. Based on theoretical expressions and using a sensitivity analysis, the importance of a certain parameter is judged. Finally, the most influencing parameters are selected.

According to the thin airfoil theory, the circulation of a flat plate in ideal conditions depends on three important parameters: the chord length, the angle of attack and the incoming flow velocity. This is given by Equation 7.14. Remember that this equation does not account for separation at high angles of attacks. The thin airfoil theory does not include the non-linearity present around the stall region of a plate.

$$\Lambda = \pi \cdot U \cdot c \sin(\alpha) \quad (7.14)$$

A parallelism can be made between vortex generator and a flat plate creating circulation. The vortex generator with length l is impinged to a flow with velocity U_e at a flow angle of β . The vortex generator height can be seen as the span of a wing. Most articles found in literature, are unanimous that the circulation produced by vortex generators depends directly on the vortex generator height. Based on the reasoning that the vortex generator length l , the inflow angle β , the height h and the flow velocity U_e are directly related to the definition of circulation for a flat plate, and assuming that the source term magnitude follows the amount of circulation produced, these parameters are selected to be important variables for the linear regression. Also, in the available data set, these variables are the most systematically changed parameters and therefore the author believes that the influence of it on the source term will be sufficiently captured with the linear regression approach. The last parameter that is selected as independent variable for the regression is the momentum thickness. This parameter represents an important flow conditions to which the vortex generators are subjected. One may also have chosen the displacement thickness or shape factor instead, because the accuracy and sensitivity of the regression is found to be similar. Resulting from this discussion, an equation of the shape given by Equation 7.15 is assumed. Note that h^* and l^* represent the non-dimensional vortex generator height and length.

$$I_{ST} = C_0 \cdot (h^*)^{C_1} \cdot (l^* \cdot \sin \beta)^{C_2} \cdot U_e^{C_3} \cdot \theta^{C_4} \quad (7.15)$$

By taking the logarithm of both sides of the equation, the dependent variable I_{ST} can be written as a linear combination of independent variables. In this situation, the vortex generator geometry and

boundary-layer variables will serve as the independent variables.

$$\log(I_{ST}) = \log(C_0) + C_1 \log(h^*) + C_2 \log(l^* \cdot \sin \beta) + C_3 \log(U_e) + C_4 \log(\theta) \quad (7.16)$$

By using the multiple variable linear regression approach, the best combination of C_0, C_1, \dots, C_5 can now be determined. Because the accuracy of the codes in clean case significantly depends on the airfoil choice, weights will be incorporated into the regression. The author believes that the source term identified to be the optimal is much more trustworthy if the aerodynamic performance of the clean airfoil is predicted well. Therefore, an error criterion is set up that describes the goodness of the clean case predictions. The error takes into account maximum lift and its corresponding angle of attack and the lift curve slope predictions. In addition to the accuracy of clean case lift predictions, the weight matrix also takes into account the amount of angles of attack that are analysed in one data set. Every data set (see Appendix A) should be equally represented in the regression independent of the amount of data points within that data set. Every data set in total, with the same clean case error, should weight equally. The elements of the weight matrix W are thus defined by Equation 7.17, where N represents the number of data points (i.e. angles of attack) in one data set and $(\Delta C_{l,max})_{clean}$, $(\Delta \alpha_{stall})_{clean}$ and $(\partial C_l / \partial \alpha)_{clean}$ are the relative differences of the maximum lift coefficient, stall angle and lift curve slope between XFOIL/RFOIL and the measurements.

$$w_{ii} = \frac{1}{N} \frac{1}{(\Delta C_{l,max})_{clean} + (\Delta \alpha_{stall})_{clean} + (\partial C_l / \partial \alpha)_{clean}} \quad (7.17)$$

For the regression, the data sets are filtered and outliers are removed. Also, the focus is put to the higher angles of attack. A clear reasoning is behind this decision. The effect that the source term has on the lift and drag at small angles of attack is smaller than the expected accuracy of the code. Therefore, the range of interest is selected to be all angles in between the stall angle of the clean airfoil and the stall angle of the airfoil equipped with vortex generators. This is the range at which the two lift curves, significantly deviate from each other. The range of interest is indicated in Figure 7.10.

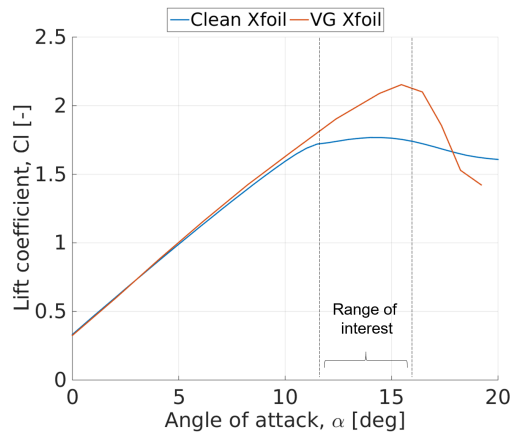


Figure 7.10: Range of interested angles of attack

7.2.3 Results Source Term Regression

By applying the weighted multiple variable linear regression method, an empirical expression is set up describing the source term integral in terms of boundary-layer properties and vortex generator geometry parameters. Two different expressions are set up for XFOIL and RFOIL. The regression coefficients are presented in Table 7.1.

To discuss the accuracy and goodness of fit of the empirical relations, Figure 7.11 to Figure 7.14 are provided. The interpretation of these plots is as follows. In Figure 7.11 and Figure 7.13, the value of the optimal source term is compared to the value prescribed by the empirical relation. If the optimal source term is closely related to the source term found by the empirical relation, the fit is assumed to be good. In that way, the data points should lie closely to the linear line prescribed by $y = x$. Less scatter in these plots implies that the data points follow the trend well. How much deviation exists between the empirical source term and the optimal one, is presented in Figure 7.12 and Figure 7.14. In these

graphs the distribution of the error existing between both source terms is plotted. The error is given by the difference between the optimal source term and the empirical one, relative to the empirical one. The errors are distributed normally. Note that part of the scatter can be related back to the fact that not all vortex generator parameters and boundary-layer properties are included into the regression as independent variables.

Table 7.1: Regression coefficients for XFOIL and RFOIL

Coefficients	XFOIL	RFOIL
C_0	$0.2970E-5$	0.0110
C_1	0.4965	0.3280
C_2	0.1433	0.0700
C_3	-1.9369	-0.4375
C_4	-0.6131	0.2608
$I_{ST} = C_0 \cdot (h^*)^{C_1} \cdot (l^* \cdot \sin \beta)^{C_2} \cdot U_e^{C_3} \cdot \theta^{C_4}$		

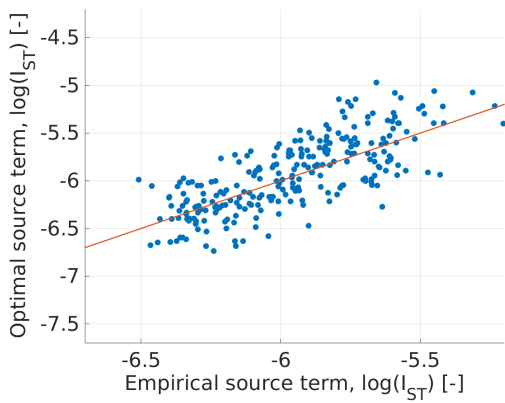


Figure 7.11: Xfoil goodness of fit of source term regression line.

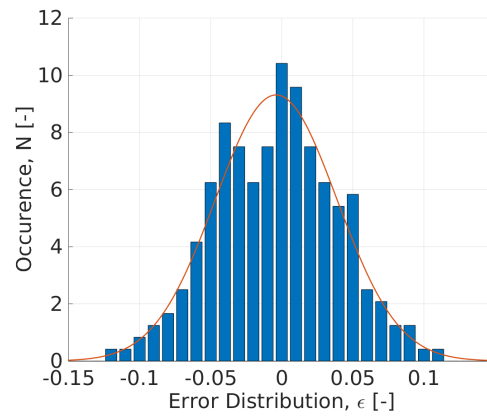


Figure 7.12: Xfoil error distribution between optimal source term and empirical source term.

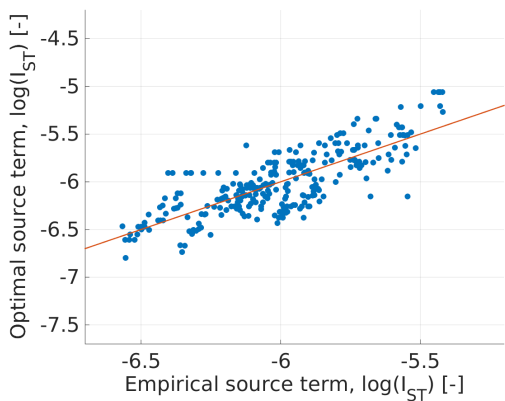


Figure 7.13: Rfoil goodness of fit of source term regression line.

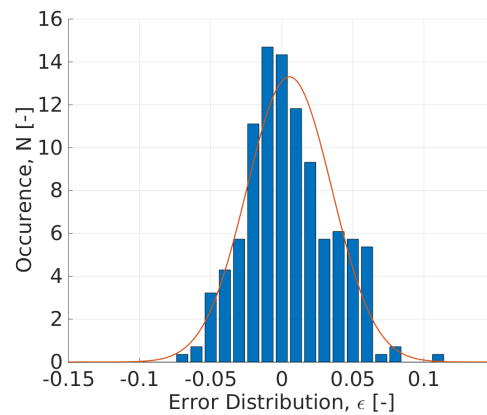


Figure 7.14: Rfoil error distribution between optimal source term and empirical source term.

7.2.4 Discussion on Source Term Regression

The resulting empirical relation should be judged with a critical attitude. All regression coefficients should be analysed in more detail to investigate whether they correspond to the expectations, and if not, what the reason could be. Also a comparison should be done between the source term relation found for XFOIL and RFOIL.

First of all, the regression coefficients accompanying the vortex generator properties can be considered. If the assumption is made that the magnitude of the source term is related to the circulation generated by the vortex generators, it is expected that the sign of the regression coefficients C_1 and C_2 are positive. This statement is based on the thin airfoil theory, that states that the circulation produced by the vortex generators increases with $h \cdot l \sin(\beta)$. The regression coefficients accompanying h and $l \sin(\beta)$ are indeed positive for both XFOIL and RFOIL but their magnitudes differ.

The identified effect of the boundary-layer properties on the source term slightly deviates from what was expected initially. Based on the circulation definition, the regression coefficient corresponding to U_e was also expected to be positive, which is not true for both XFOIL and RFOIL. From this result, it is insinuated that the strength of the vortex generator decreases with increasing flow velocity. This is, however, not corresponding to what is said in literature. One may also have observed that the sign of the coefficient corresponding to the momentum thickness θ appears to be opposed for XFOIL as for RFOIL. The opposed sign of the regression coefficient implies that the effect that the momentum thickness has on the source term, is reversed. One may expect that the vortex generators are the most effective when the momentum thickness is the smallest, and thus that the source term should decrease with increasing momentum thickness. This is indeed true for the source term equation found for XFOIL but not for the one found for RFOIL. These observations may raise questions.

After critically evaluating these observations, a potential explanation will be given that might explain why the coefficients are different for XFOIL and RFOIL and why the regression coefficients corresponding to the boundary-layer properties are not all as expected. This will be explained below.

- **Closure relations:** The reason why XFOIL and RFOIL are finding different regression coefficients can be related back to the theory behind these codes. XFOIL and RFOIL are two viscid-inviscid codes both using similar solution methods relying on their own set of closure relations. XFOIL and RFOIL opt for different constants in the $G-\beta$ locus and different expressions are used for the shear lag coefficient K_c . In RFOIL, the value of K_c is depending on the shape factor H while in XFOIL, the shear lag coefficient is assumed to be constant. The closure relations are significantly influencing the prediction of the aerodynamic properties and consequently also how a source term is handled. To support that the effectiveness of a source term is significantly depending on the chosen closure relations, the expression of K_c in XFOIL is adapted and the optimal source terms are recalculated using the calibration process. This analysis has proven that the influence of the boundary-layer closure relations on the source term is very strong and its effect cannot be neglected. Decreasing the shear lag coefficient already led to the fact that the trend between the source term and angle of attack opposed. The details of this analysis are presented in Appendix B.
- **Error clean airfoil:** XFOIL and RFOIL are basic two-dimensional codes and it is already known that these codes, especially at higher angles of attack, miss some accuracy in their lift and drag prediction. On top of that, measurement and CFD data have their limitations. Most often, the lift slope is overestimated as well as the maximum lift coefficient, and drag is underestimated. In most cases, the resulting polars may still be considered to be within an acceptable range. However, for RFOIL in particular, the aerodynamic performance of the DU331 and FFAW3333 with forced transition at the leading edge and without vortex generators are very badly recorded when compared to the reference data. In this case, the lift is extremely under predicted. This is a serious issue since also the trustworthiness of the optimal source term found for these two airfoils may be questioned. Since these two airfoils form almost half of the available data base, it was impossible to take these two airfoils out of the regression process. The data base would become too small to draw any conclusions on the source term dependency. From this issue, it is expected that the net effect of the vortex generators on the lift will be over predicted. A comparison of the lift and drag polars originating from measurements, XFOIL and RFOIL is provided in Appendix C.
- **Internal parameters:** The boundary-layer edge velocity and momentum thickness are internal parameters calculated by XFOIL and RFOIL. These boundary-layer parameters might not always be modelled correctly according to the reality (e.g. spanwise averaging of three dimensional flowfield). Therefore, it seems obvious that the regression coefficients corresponding to these two parameters are less reliable than others.

- **Target value:** The optimal source term is selected as such that it is reproducing the effect that vortex generators have on lift. That effect was estimated based on measurement data and a correction factor. The role of the measurement data and correction factor is very strong since slight deviations in one of those may significantly influence directly what source term is selected to be the optimal.

The set of closure relations used, the error in the clean airfoil modelling, the use of internally calculated parameters and the role of the target lift value, cause an accumulation of uncertainties. These uncertainties influence the source term calibration process and propagate to the final empirical relation of the source term. The reader should realise that fully relating the required source term to the theoretical circulation produced by the vortex generators would be too hopeful since the source term approach is still an engineering approach to model vortex generators. Based on the discussion above, the author has at this stage more faith in the source term relation found for XFOIL than for RFOIL, however, it is still believed that the results of both codes are worth further consideration.

7.3 Implementation of the Source Term Empirical Relation

The empirical source term relation set up in the previous section, can now be implemented in the boundary-layer codes. The source term will be computed internally and thus direct inputs for the source term are no longer required. The original XFOIL and RFOIL codes will be able to deal with the presence of vortex generators and the foundations of XFOILVG and RFOILVG will be born.

The empirical relation set up for the source term depends on two main inputs: the vortex generator configuration and the boundary-layer properties at the location of the vortex generator. The parameters defining the vortex generator configuration need to be specified as an input to the code. The parameters of interest are the location of the vortex generator, the height, length and inflow angle. The boundary-layer properties at the location of the vortex generator need to be collected inside the program. In every iteration of the solution, the momentum thickness and boundary-layer edge velocity are isolated and the source term integral is recalculated using the empirical relation.

To finally specify the value of the source term at every chordwise position, the source term integral needs to be traced back to the strength and decay parameter to define the source term shape function. With the source term integral known and assuming a fixed decay value λ , the corresponding source term strength parameter σ_0 can be derived. Note again that the exact value of the decay parameter has only minor influence on the results. It was found before that it is a valid assumption to assume that every combination of strength and decay that enclose the same area (same source term integral) predict the same aerodynamic properties.

To illustrate the implementation of the source term empirical relation into XFOIL and RFOIL, a simplified flow scheme of the integral boundary-layer code is provided in Figure 7.15.

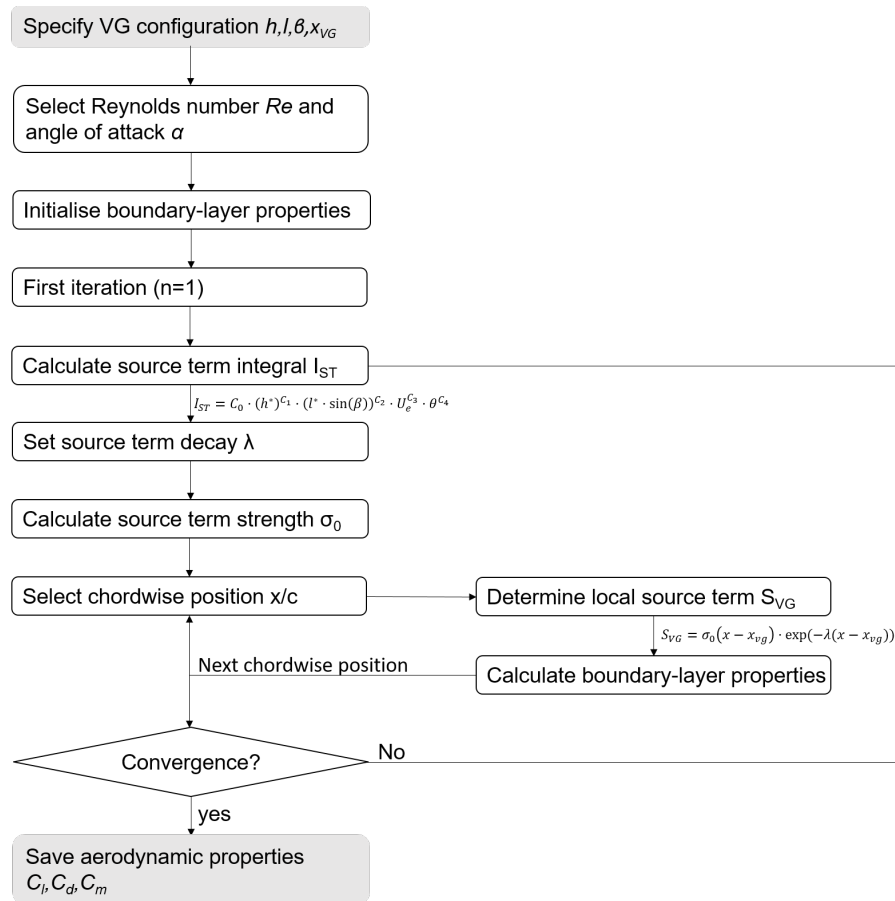


Figure 7.15: Flow chart source term implementation.

XFOILVG and RFOILVG are now able to calculate the aerodynamic properties of an airfoil equipped with vortex generators. To analyse how well the predictions match with reality, a validation needs to be done. In a validation process, the simulated numerical results should be compared to reference data. When discrepancies are significant, a critical reflection is important. The validation of the XFOIL and RFOIL code are presented in this chapter. As a first step in the validation process, the code performance will be analysed based on the data sets that are already used to set up the source term empirical relation. This first validation allows to validate the empirical relation. If from this validation it may be concluded that the codes perform properly, the second part of the validation can be done. In this second part of the validation, external reference data, adopted from literature, will be used. This part of the validation process focusses on proving the robustness of the code regarding airfoil and Reynolds number selection. The results of this part of the validation are presented in the second section. The first two sections of this chapter will focus only on observing the predictions of both codes. At the end of this chapter, all the observations will be combined and the codes' performance and limitations assessed. Also the code limitations will be established.

8.1 First Validation: Source Term Relation

In the first step of the validation process, the source term empirical relations will be validated. Various cases are selected from the reference data base. Because the cases used in this part of the validation are already used to derive the source term empirical relation, it is expected that the prediction will automatically be relatively good. The reader can consult Appendix D, to see how close the calibrated source term of the cases used in this part of the validation, lie to the source term found by the empirical relation. In this section, the focus will be only on the observations that can be made by comparing the lift and drag polars. The evaluation of these observations is given in the last section of this chapter.

8.1.1 LTT Data Set

One of the dominant data sets in the determination of the source term empirical relation is the LTT data set. This data is gathered experimentally during this master thesis. A DU97W300 airfoil equipped with different vortex generator configurations is tested in the low speed low turbulence wind tunnel of the TU Delft. As validation, the effect of varying the vortex generator position and vortex generator height will be analysed.

In Figure 8.1 and Figure 8.2, the lift and drag polars of the DU97W300 airfoil are presented for varying vortex generator positions. The numerical results of both XFOIL and RFOIL are presented as well as the reference data of the wind tunnel experiment. The model used during the tests had a chord length of 0.65m and was equipped with 10mm high and 15mm long vortex generators put under an inflow angle of 15° . The whole model was subjected to a flow with a Reynolds number of $2E6$. The vortex generators are positioned at 30, 40 and 50% chord length. As a reference, and to indicate how good the clean airfoil was modelled by XFOIL and RFOIL, the clean airfoil lift and drag polars are provided. Clean airfoil refers to a case where no vortex generators are included. In general, the maximum lift coefficient and stall angle increase when the vortex generators are more upstream. This behaviour is captured clearly by XFOIL. For RFOIL, the same behaviour is observed, however, it is less pronounced. XFOIL seems to predict the maximum lift coefficient accurately within an error of 5%. This error represents the difference between the reference data and the code with respect to the reference data. When considering the drag, one may observe that drag is in general underestimated. This fulfils the expectations, since the model does not account for the vortex generator profile drag. Further, the more the vortex generators are positioned to the leading edge, the earlier the flow is forced to transition from laminar to turbulent and the larger the drag is at pre-stall angles of attack. This behaviour is correctly modelled by both

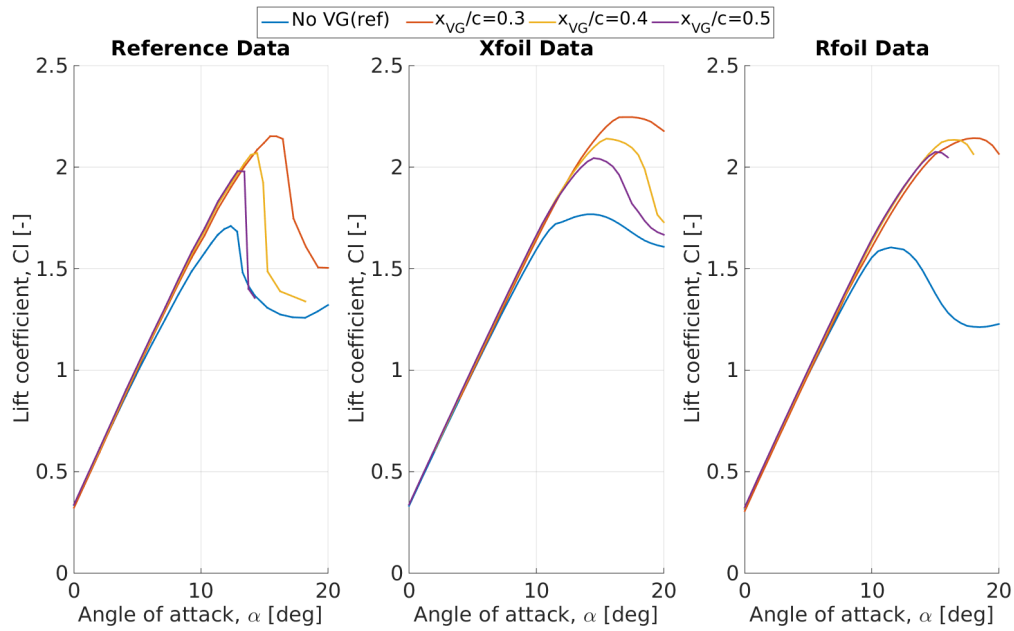


Figure 8.1: Lift polar of the DU97W300 airfoil at $Re = 2E6$ with $h = 10\text{mm}$, $l = 30\text{mm}$, $\beta = 15^\circ$ and varying position originating from measurements, XFOIL and RFOIL

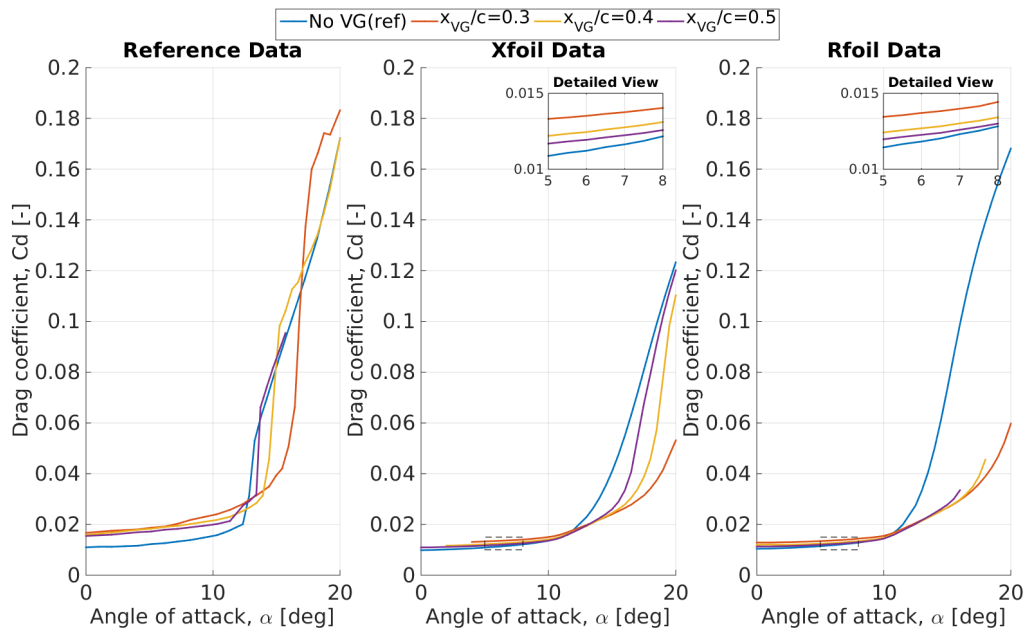


Figure 8.2: Drag polar of the DU97W300 airfoil at $Re = 2E6$ with $h = 10\text{mm}$, $l = 30\text{mm}$, $\beta = 15^\circ$ and varying position originating from measurements, XFOIL and RFOIL

Table 8.1: Error XFOIL and RFOIL in Figure 8.1

Case	Reference		Xfoil Error		Rfoil Error	
	Stall angle[deg]	Max lift[-]	Stall angle[-]	Max lift[-]	Stall angle[-]	Max lift[-]
Clean	12.35	1.71	0.13	0.04	-0.07	-0.06
$x/c=0.3$	15.94	2.15	0.10	0.05	0.13	0.00
$x/c=0.4$	14.42	2.07	0.07	0.03	0.14	0.03
$x/c=0.5$	13.41	1.98	0.08	0.03	0.12	0.05

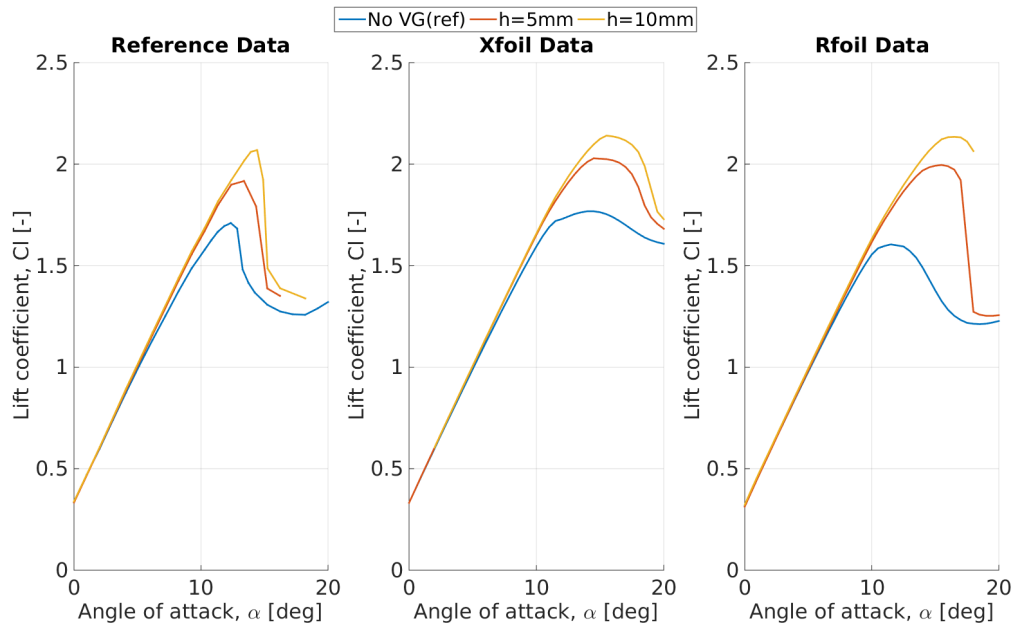


Figure 8.3: Lift polar of the DU97W300 airfoil at $Re = 2E6$ with $l = 3h$ mm, $\beta = 15^\circ$, $x_{vg}/c = 0.4$ and varying height originating from measurements, XFOIL and RFOIL

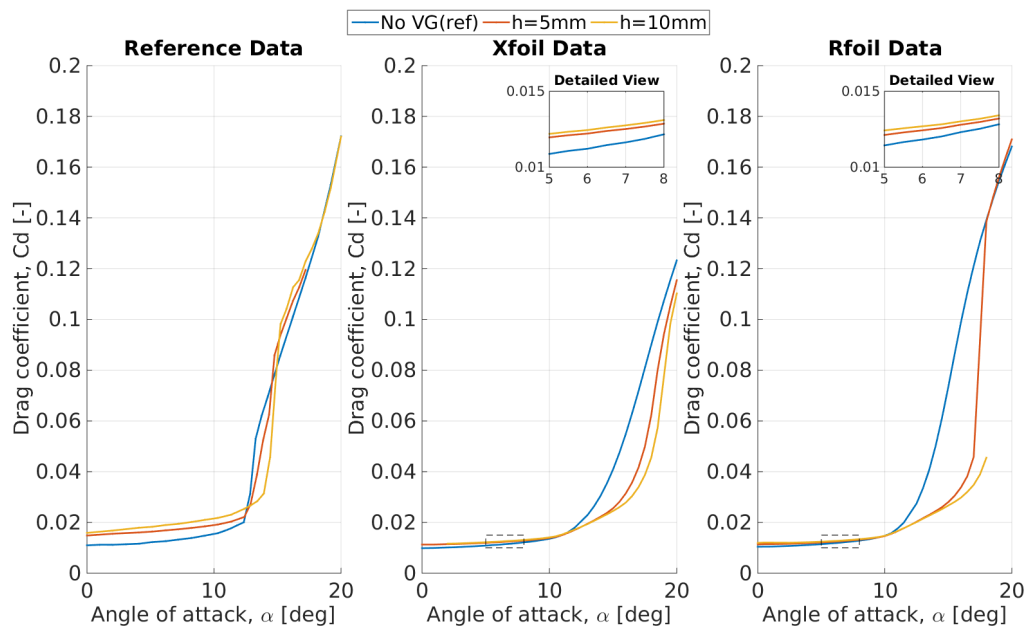


Figure 8.4: Drag polar of the DU97W300 airfoil at $Re = 2E6$ with $l = 3h$ mm, $\beta = 15^\circ$, $x_{vg}/c = 0.4$ and varying height originating from measurements, XFOIL and RFOIL

Table 8.2: Error XFOIL and RFOIL in Figure 8.3

Case	Reference		Xfoil Error		Rfoil Error	
	Stall angle[deg]	Max lift[-]	Stall angle[-]	Max lift[-]	Stall angle[-]	Max lift[-]
Clean	12.35	1.71	0.13	0.04	-0.07	-0.06
h=5	13.39	1.92	0.08	0.06	0.16	0.04
h=10	14.42	2.07	0.07	0.03	0.14	0.03

XFOIL and RFOIL. The error of the numerical results with respect to the reference data is quantified in Table 8.1.

In Figure 8.3 and Figure 8.4, the lift and drag polar of the same DU97W300 airfoil are presented but now for varying vortex generator heights. For these cases, the vortex generators are at a fixed position of 40% of the chord. The height varies from 5mm to 10mm and the length to height ratio is kept constant to 3. The effect of increasing the vortex generator height is captured well by both XFOIL and RFOIL. The maximum lift and the drag at pre-stall angles increase. Note that both codes slightly over predict the maximum lift and stall angle. For XFOIL this could be expected since also in clean case the maximum lift is over predicted. The accuracy of XFOIL and RFOIL are quantified in Table 8.2.

According to the relative errors, quantified in Table 8.1 and Table 8.2, XFOIL offers a better prediction of the DU97W300 characteristics with vortex generators. The maximum lift predictions are for both codes within the same range but the stall angle is better modelled by XFOIL.

8.1.2 AVATAR Data Set

The second internal data set that is used to validate the source term empirical relation of XFOIL and RFOIL is the AVATAR data set. This data set originates from a parametric study as part of the AVATAR project⁸⁶ and is obtained using fully turbulent CFD computations. Two different airfoils are used. The first airfoil model has a DU331 cross-section and a chord length of 6.06m. The second model is shaped with a FFAW3333 airfoil and has a chord length of 5.84m. The airfoils are visualised in Figure 8.5 and Figure 8.6, respectively. For the purpose of validation, variation in vortex generator height and inflow angle are studied.

Figure 8.7 to Figure 8.10 present the parametric study of vortex generator height on the airfoil polars for the DU331 and FFAW3333 airfoil. The vortex generators are in both cases positioned at 40% of the chord and have a length over height ratio of 3. The counter-rotating vane type vortex generators are put under an angle of 20° and encounter a flow at Reynolds number $15.8E6$ and $14.0E6$ depending on the airfoil selection. Since the reference data is a fully turbulent simulation, transition is forced at 0.01 in XFOIL and RFOIL. The general behaviour of the lift and drag polars are in both cases the same. Increasing the vortex generator height, increases the maximum lift coefficient that can be obtained as well as the according stall angle. The sudden drop in lift and sudden increase in drag for the DU331 airfoil case with $h = 60\text{mm}$ vortex generators is assumed to be an outlier. The numerical simulations of both XFOIL and RFOIL seem to closely agree with the measurement data. Although the maximum lift coefficient and stall angle are relatively well predicted by RFOIL for both airfoils, the net effect of adding vortex generators is overestimated to a great extent. The clean airfoil computations with forced transition at the leading edge show a large error that could not be alleviated by using the lift curve correction. The maximum lift and stall angle prediction in clean case deviate more than 20% from the reference data as shown in Table 8.3 and Table 8.4.

In Figure 8.11 to Figure 8.14, the effect of increasing the vortex generator inflow angle on the lift and drag polar is presented. The same two airfoils are used but now the vortex generator height is fixed to 10mm. Inflow angles of 15° , 20° and 25° are compared. The larger the inflow angle, the larger the effect on lift. However, increasing the inflow angle from 10° to 15° is more significant than increasing the inflow angle from 15° to 20° , especially for the FFAW3333 airfoil. Finally, note that again the net effect of the vortex generator resulting when comparing the clean airfoil with the VG case, is overestimated by RFOIL. The evaluation of these observations is provided further in this chapter. Error indications are provided in Table 8.5 and Table 8.6.

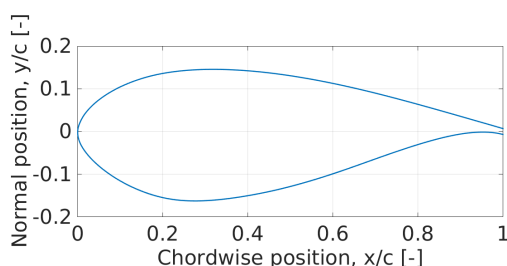


Figure 8.5: Cross-section of the DU331 airfoil.

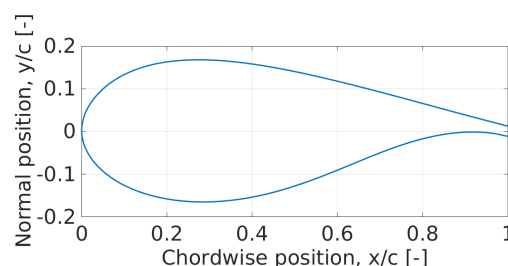


Figure 8.6: Cross-section of the FFAW3333 airfoil.

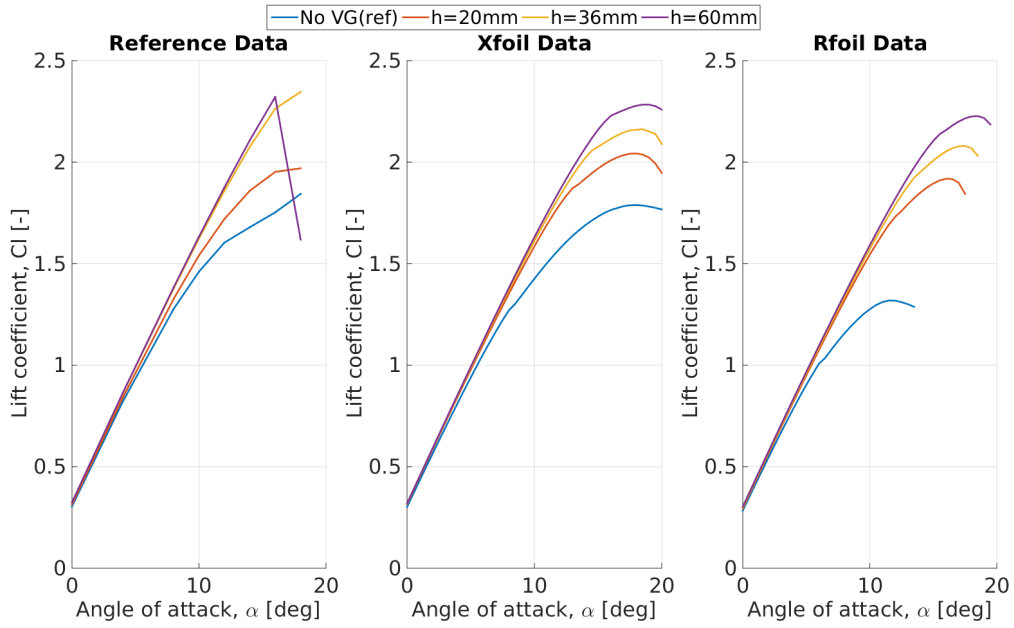


Figure 8.7: Lift polar of the DU331 airfoil at $Re = 15.8E6$ with $l = 3h$ mm, $\beta = 20^\circ$, $x_{vg}/c = 0.4$ and varying height originating from measurements, XFOIL and RFOIL

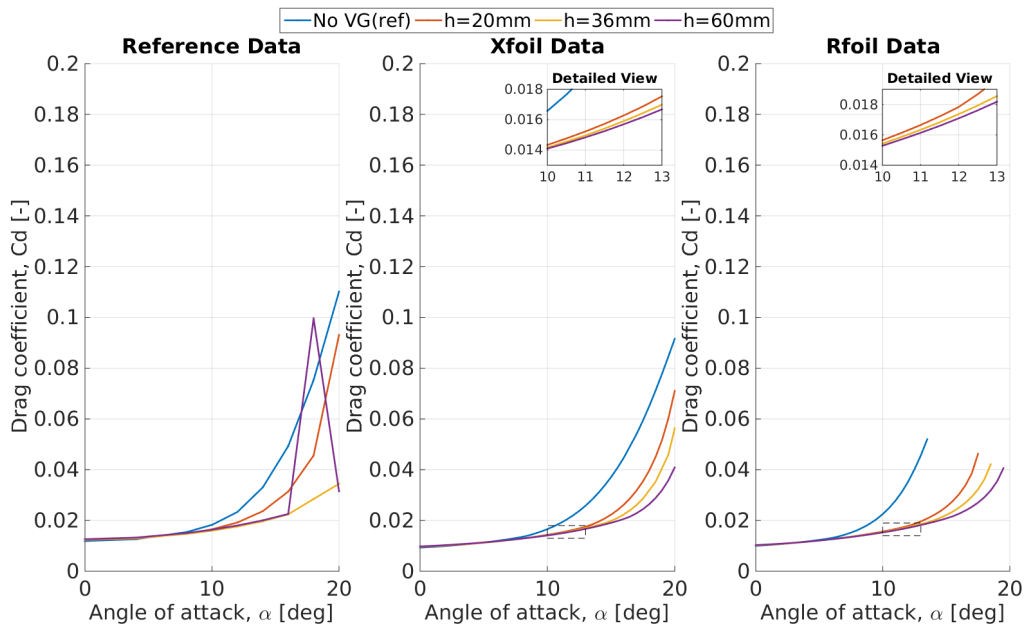


Figure 8.8: Drag polar of the DU331 airfoil at $Re = 15.8E6$ with $l = 3h$ mm, $\beta = 20^\circ$, $x_{vg}/c = 0.4$ and varying height originating from measurements, XFOIL and RFOIL

Table 8.3: Error XFOIL and RFOIL in Figure 8.7

Case	Reference		Xfoil Error		Rfoil Error	
	Stall angle[deg]	Max lift[-]	Stall angle[-]	Max lift[-]	Stall angle[-]	Max lift[-]
Clean	18.00	1.84	-0.03	-0.03	-0.33	-0.28
h=20	18.00	1.97	0.00	0.04	-0.11	-0.03
h=36	>18.00	>2.34	0.03	-0.08	-0.03	-0.11
h=60	>18.00	>2.32	0.03	-0.02	0.03	-0.04

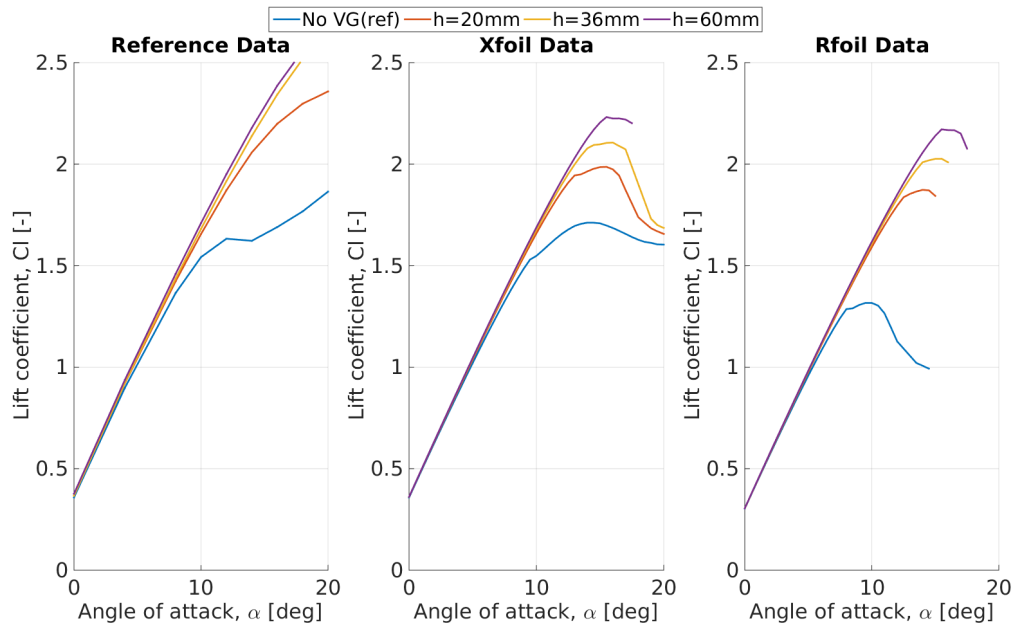


Figure 8.9: Lift polar of the FFAW3333 airfoil at $Re = 14.0E6$ with $l = 3h$ mm, $\beta = 20^\circ$, $x_{vg}/c = 0.4$ and varying height originating from measurements, XFOIL and RFOIL

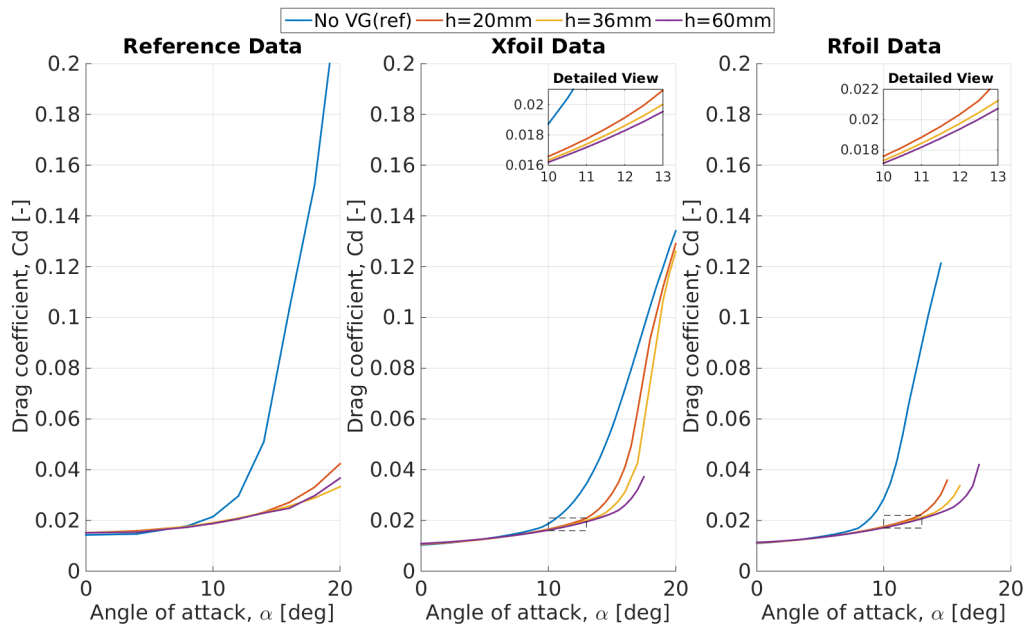


Figure 8.10: Drag polar of the FFAW3333 airfoil at $Re = 14.0E6$ with $l = 3h$ mm, $\beta = 20^\circ$, $x_{vg}/c = 0.4$ and varying height originating from measurements, XFOIL and RFOIL

Table 8.4: Error XFOIL and RFOIL in Figure 8.9

Case	Reference		Xfoil Error		Rfoil Error	
	Stall angle[deg]	Max lift[-]	Stall angle[-]	Max lift[-]	Stall angle[-]	Max lift[-]
Clean	12.00	1.63	0.17	0.05	-0.17	-0.19
h=20	20.00	2.36	-0.25	-0.16	-0.30	-0.21
h=36	20.00	2.65	-0.23	-0.20	-0.25	-0.23
h=60	20.00	2.67	-0.23	-0.16	-0.23	-0.19

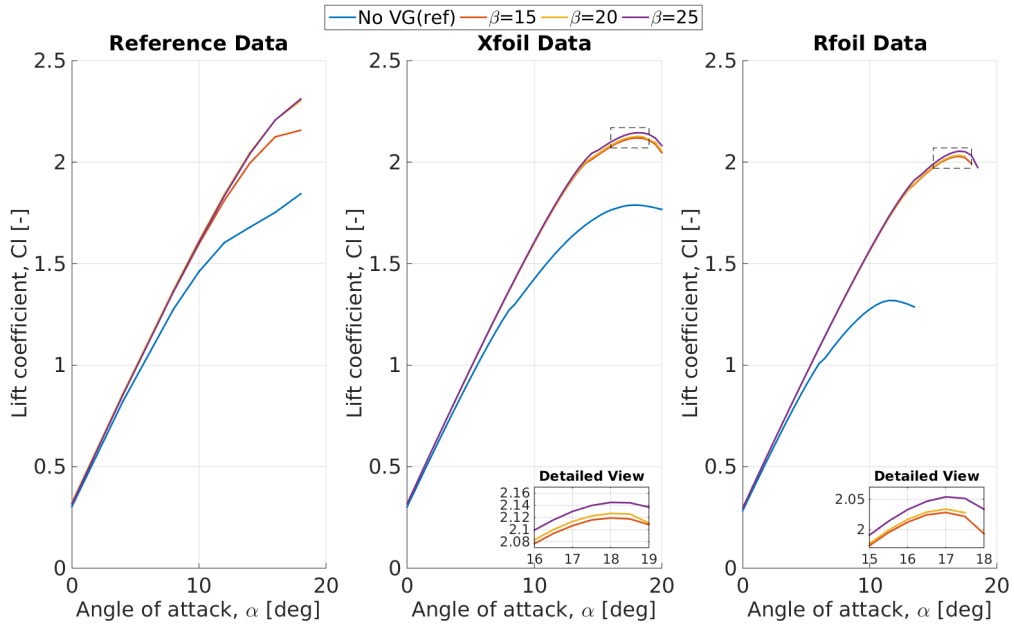


Figure 8.11: Lift polar of the DU331 airfoil at $Re = 15.8E6$ with $h = 10\text{mm}$, $l = 30\text{mm}$, $x_{vg}/c = 0.4$ and varying inflow angle originating from measurements, XFOIL and RFOIL

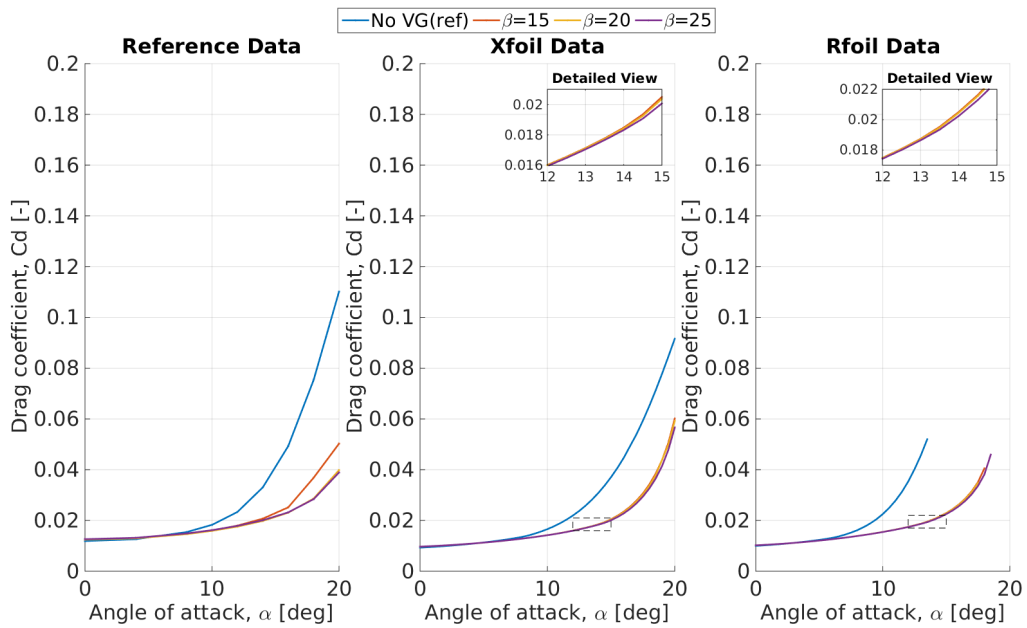


Figure 8.12: Drag polar of the DU331 airfoil at $Re = 15.8E6$ with $h = 10\text{mm}$, $l = 30\text{mm}$, $x_{vg}/c = 0.4$ and varying inflow angle originating from measurements, XFOIL and RFOIL

Table 8.5: Error XFOIL and RFOIL in Figure 8.11

Case	Reference		Xfoil Error		Rfoil Error	
	Stall angle[deg]	Max lift[-]	Stall angle[-]	Max lift[-]	Stall angle[-]	Max lift[-]
Clean	18.00	1.84	-0.03	-0.03	-0.33	-0.28
$\beta=15$	>18.00	>2.16	0.00	-0.02	-0.06	-0.06
$\beta=20$	>18.00	>2.30	0.00	-0.07	-0.06	-0.11
$\beta=25$	>18.00	>2.31	0.00	-0.07	-0.06	-0.11

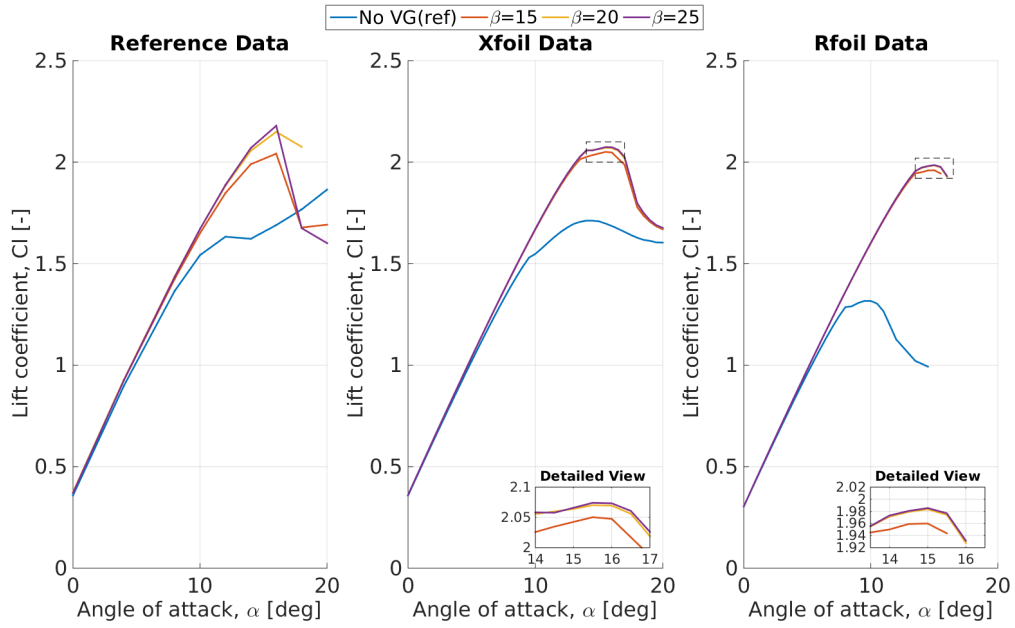


Figure 8.13: Lift polar of the FFAW3333 airfoil at $Re = 14.0E6$ with $h = 10\text{mm}$, $l = 30\text{mm}$, $x_{vg}/c = 0.4$ and varying inflow angle originating from measurements, XFOIL and RFOIL

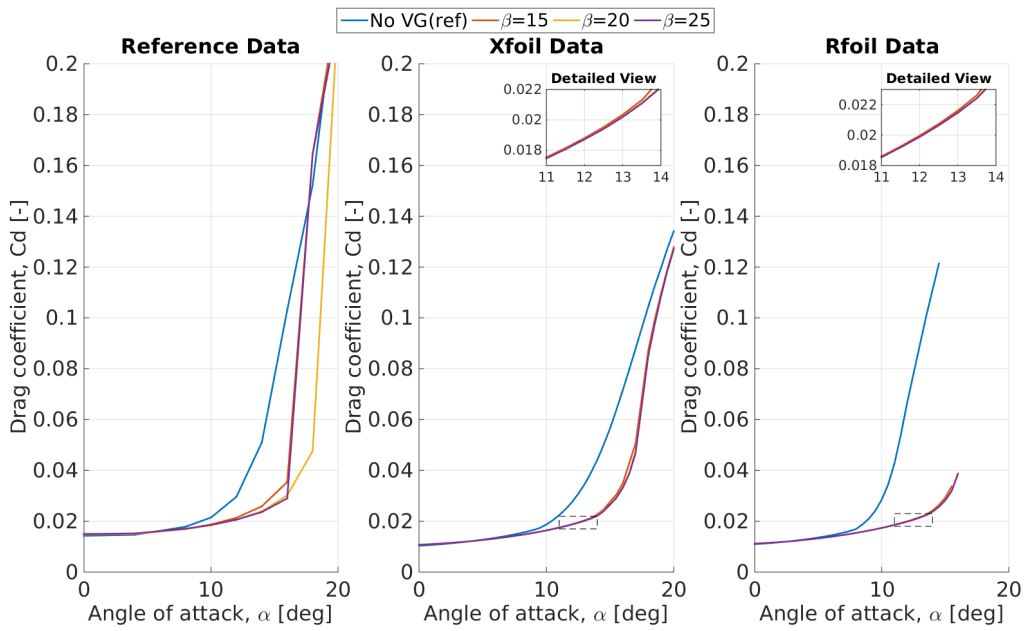


Figure 8.14: Drag polar of the FFAW3333 airfoil at $Re = 14.0E6$ with $h = 10\text{mm}$, $l = 30\text{mm}$, $x_{vg}/c = 0.4$ and varying inflow angle originating from measurements, XFOIL and RFOIL

Table 8.6: Error XFOIL and RFOIL in Figure 8.13

Case	Reference		Xfoil Error		Rfoil Error	
	Stall angle[deg]	Max lift[-]	Stall angle[-]	Max lift[-]	Stall angle[-]	Max lift[-]
Clean	12.00	1.63	0.17	0.05	-0.17	-0.19
$\beta=15$	16.00	2.04	-0.03	0.00	-0.06	-0.04
$\beta=20$	16.00	2.15	-0.03	-0.04	-0.06	-0.08
$\beta=25$	16.00	2.18	-0.03	-0.05	-0.06	-0.09

The validation of the AVATAR data set can be concluded by stating that the numerical lift polar for VG cases of XFOIL and RFOIL are in good qualitative and reasonably quantitative agreement with the reference data. Note that the errors provided by Table 8.3 to Table 8.6 are in three of the four cases only indicative since the reference data does not show a clear stall behaviour within the given angle of attack range. In the one case where the reference data shows a clear stall behaviour, the accuracy of XFOIL remains within 5% and for RFOIL within 10%. The large difference existing between the clean airfoil reference data and RFOIL data rises doubts about the value of the prediction.

8.1.3 TUD Data Set

The last data set used to validate the vortex generator implementation into XFOIL and RFOIL is the TUD data set. This data set is generated by W.A. Timmer and R.P. van Rooij⁸⁵. They have performed wind tunnel experiments on the DU91W2250, DU93W210 and the DU97W300 airfoil equipped with counter rotating vane type vortex generators. Analysing the modelling results of the DU91W2250 and DU93W210 is very valuable since these two airfoils had only little influence to the source term empirical relation. The amount of cases available for these two airfoils is much smaller compared to the amount of data available for the DU97W300, DU331 and FFAW3333. If the aerodynamic behaviour of these two airfoils is well predicted, it is already a first step in approving the code robustness. In the TUD data set, the effect of the chordwise position of the vortex generators is studied.

Figure 8.17 and Figure 8.18 present the lift and drag polars of a 2D wing with a DU91W2250 cross-section equipped with vortex generators. This airfoil is visualised in Figure 8.15. The vortex generators used during the experiment had a height of 5mm, length of 17mm and were put at an inflow angle of 16.4° . The airfoil with 0.6m chord is tested at a Reynolds number of $2E6$. From the lift polar, it is clearly visible that adding a vortex generator is favourable considering the maximum lift coefficient. The vortex generators increase the lift coefficient with more than 30%. According to the measurement data, the vortex generators are best located at 20% of the chord. XFOIL confirms this while according to RFOIL locating the vortex generators at 30% is favourable. For both codes, it is remarkable that the stall angle is significantly over-predicted while the maximum lift is captured within an acceptable range of 1% for XFOIL and 10% for RFOIL. A summary of the codes' accuracies is provided in Table 8.7.

In Figure 8.19 and Figure 8.20, the lift and drag performance of the DU93W210 airfoil at a Reynolds number of $1E6$ is analysed. The airfoil cross-section is plotted in Figure 8.16. The airfoil model was equipped with the same vortex generators as before but now they are installed at 20%, 40% and 60% of the chord. Again, the location reaching the highest maximum lift is at 20% chord length. This is also found by XFOIL and now also by RFOIL. However, placing the vortex generators closer to the leading edge introduces earlier transition and this is on its turn associated with a lift curve slope decrease. Especially with the vortex generators installed at 20% of the chord, this is clearly visible in the measurement data, XFOIL data and the RFOIL data. The slope decrease seems to be overestimated by RFOIL. Depending on the vortex generator location, the accuracy of the numerical maximum lift results of both codes vary from 1% to slightly more than 10%.

From this discussion, both codes emerged to be modelling the effect of vortex generators with a similar accuracy. Despite the fact that the maximum lift coefficient is estimated within acceptable limits, the stall angle is overestimated. According to the reference data, stall occurs very suddenly while both codes predict a more gradual stall behaviour. RFOIL seems to better perform when the vortex generators are positioned more downstream. The drag modelled by both codes is still under-predicted but this can again be related back to the fact that in general the codes miss some accuracy in drag even in clean case and that the profile drag is not incorporated into the integral boundary-layer codes yet.

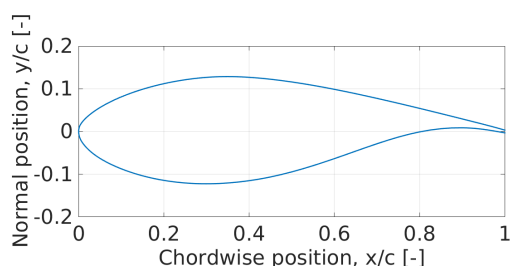


Figure 8.15: Cross-section of the DU91W2250 airfoil.

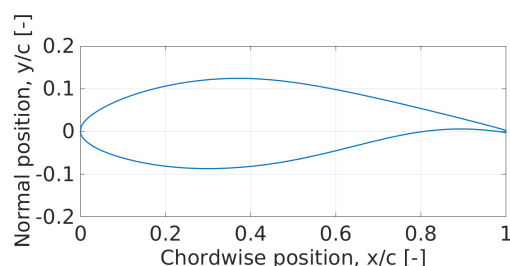


Figure 8.16: Cross-section of the DU93W210 airfoil.

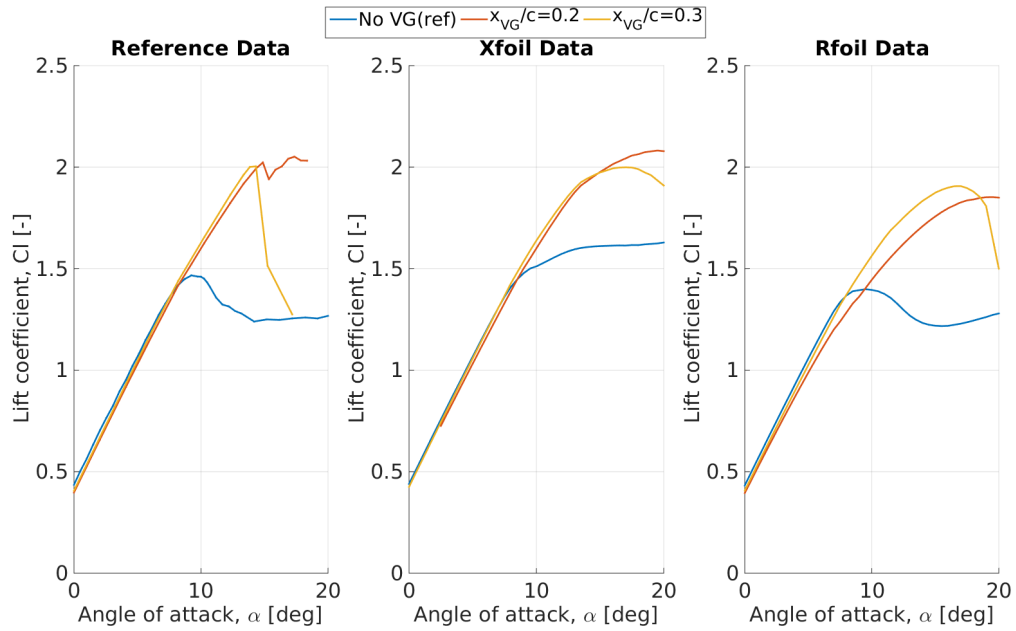


Figure 8.17: Lift polar of the DU91W2250 airfoil at $Re = 2E6$ with $h = 5\text{mm}$, $l = 17\text{mm}$, $\beta = 16.4^\circ$ and varying position originating from measurements, XFOIL and RFOIL

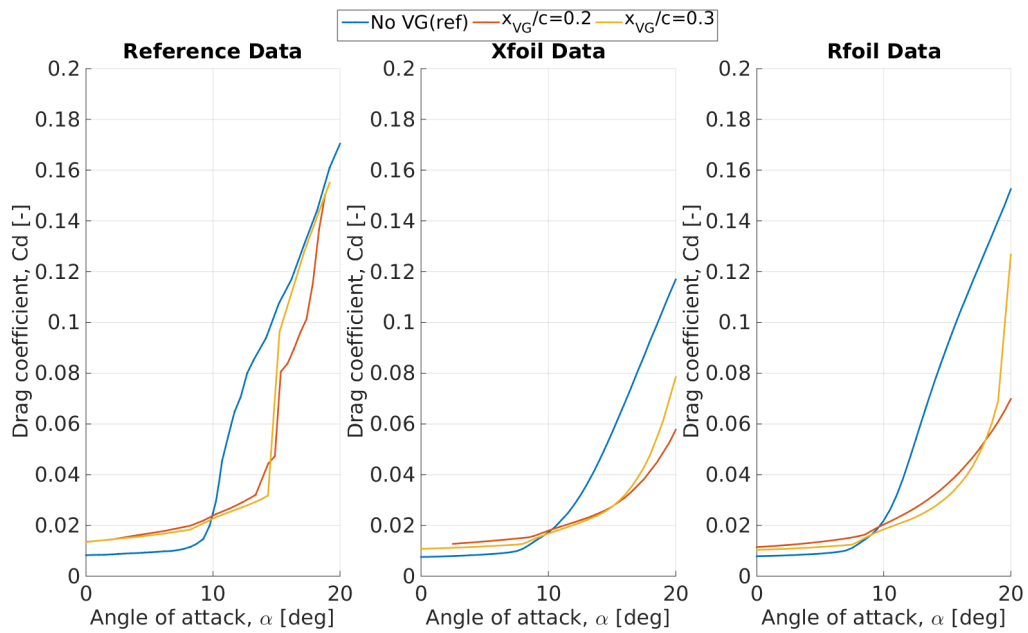


Figure 8.18: Drag polar of the DU91W2250 airfoil at $Re = 2E6$ with $h = 5\text{mm}$, $l = 17\text{mm}$, $\beta = 16.4^\circ$ and varying position originating from measurements, XFOIL and RFOIL

Table 8.7: Error XFOIL and RFOIL in Figure 8.17

Case	Reference		Xfoil Error		Rfoil Error	
	Stall angle[deg]	Max lift[-]	Stall angle[-]	Max lift[-]	Stall angle[-]	Max lift[-]
Clean	9.24	1.47	0.46	0.09	0.03	-0.05
$x/c=0.2$	17.36	2.05	0.12	0.01	0.12	-0.10
$x/c=0.3$	14.33	2	0.19	0.00	0.19	-0.05

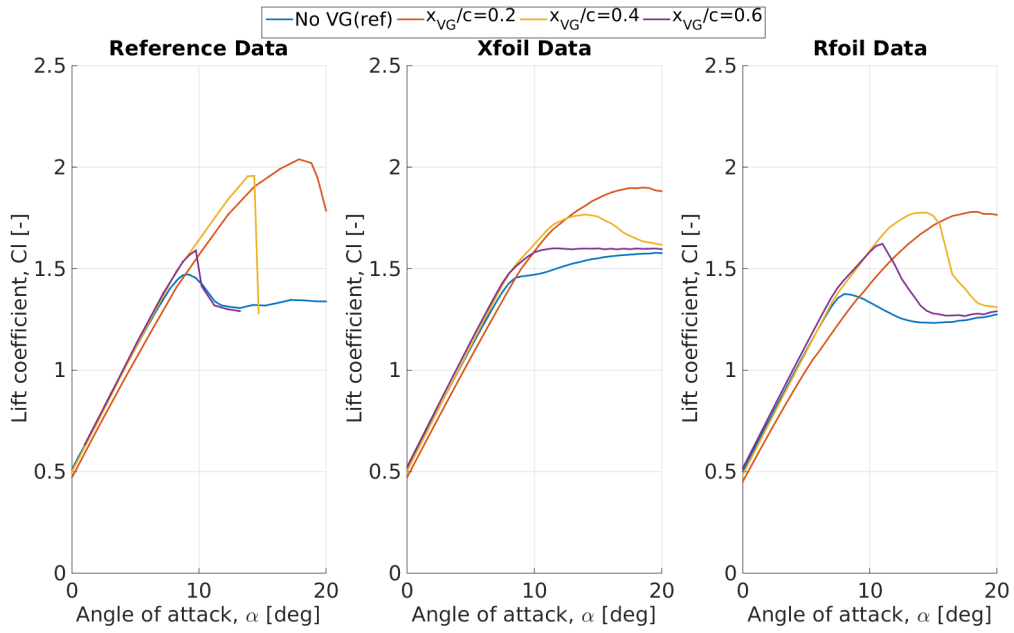


Figure 8.19: Lift polar of the DU93W210 airfoil at $Re = 1E6$ with $h = 5\text{mm}$, $l = 17\text{mm}$, $\beta = 16.4^\circ$ and varying position originating from measurements, XFOIL and RFOIL

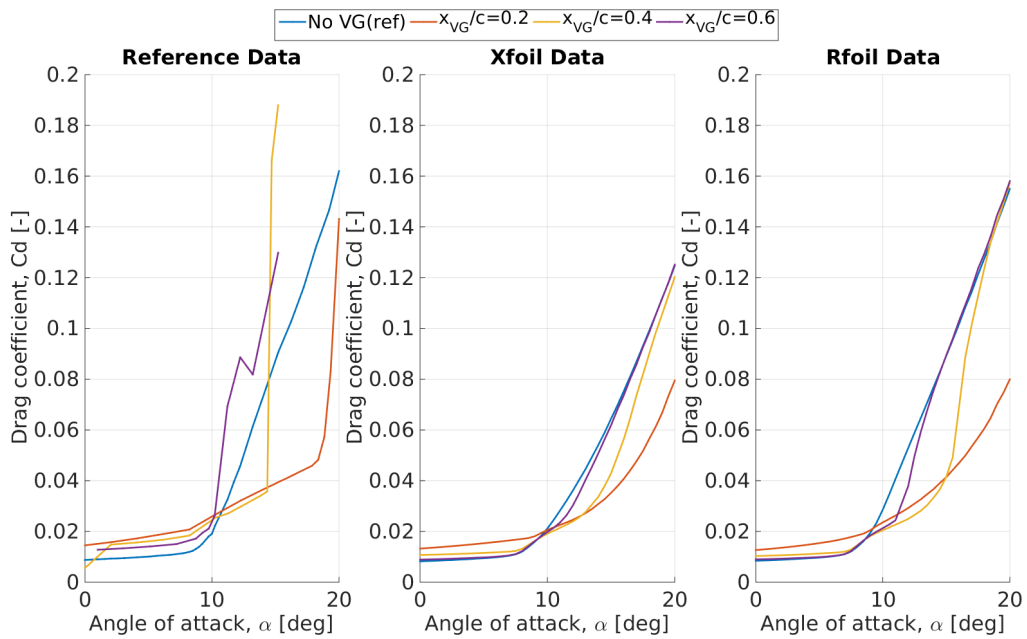


Figure 8.20: Drag polar of the DU93W210 airfoil at $Re = 1E6$ with $h = 5\text{mm}$, $l = 17\text{mm}$, $\beta = 16.4^\circ$ and varying position originating from measurements, XFOIL and RFOIL

Table 8.8: Error XFOIL and RFOIL in Figure 8.19

Case	Reference		Xfoil Error		Rfoil Error	
	Stall angle[deg]	Max lift[-]	Stall angle[-]	Max lift[-]	Stall angle[-]	Max lift[-]
Clean	8.98	1.47	0.00	-0.01	-0.11	-0.06
x/c=0.2	17.87	2.04	0.04	-0.07	0.04	-0.13
x/c=0.4	14.35	1.98	-0.02	-0.11	0.01	-0.10
x/c=0.6	9.75	1.59	0.18	0.01	0.13	0.02

8.2 Second Validation: Code Robustness

The set up of the source term empirical relation is based on the analysis of five airfoils. It is believed that these airfoils are diverse enough to be representative for other airfoil families. The second part of the validation process focusses on demonstrating the code robustness and the capability of modelling the behaviour of other airfoils than the ones used to set up the empirical relation. The numerical lift and drag results will be compared to reference data collected from literature. Note that finding proper reference data is not so simple since details of the vortex generator configurations are often incomplete. Two data sets will be considered and introduced further in this section. Remark that the presented reference data has been transformed using the lift curve correction, as presented before, to get good agreement for the clean cases. In this way, lift curve slopes will match and the comparisons become more valuable.

8.2.1 Pechlivanoglou Data Set

The first considered data set is originating from a study performed by G. Pechlivanoglou⁹¹. As part of his PhD thesis, he investigated the possibilities of aerodynamic flow control on wind turbine blades, with vortex generators as one of these possibilities. He performed an experimental study using the wind tunnel facilities of TU Berlin. The airfoil model had a AH93W174 cross-section and a chord length of 0.6m. It is a relatively thick airfoil (17.4% thickness) and was designed especially for the mid-span and outboard part of wind turbine blades. The shape of this airfoil is plotted in Figure 8.21. In this study, the special focus was on the effect of positioning the vortex generators at different chordwise locations. Note that the measurement data is digitalised from the graphs presented in the thesis report of G. Pechlivanoglou⁹¹. Since this process involved some manual action, small deviations in the data can be expected but this will not influence the value of this validation. Especially in the linear part of the lift curve, it was impossible to distinguish differences between the different test cases.

In Figure 8.22 and Figure 8.23 the lift and drag polars derived from the reference and the ones computed using XFOIL and RFOIL are presented. Three different cases are presented: the clean airfoil as reference, a case with vortex generators installed at 20% chord length and a case where the vortex generators are positioned at 30% chord length. The vortex generators that were used in the experiment had a height of 9mm, length of 18mm and inflow angle of 18°. The model is tested at a Reynolds number of $1.3E6$. When adding vortex generators to the airfoil, stall is delayed and the maximum lift of the airfoil is increased with approximately 30%. The drag increases at pre-stall angles of attack due to the earlier transition and higher skin friction. At high angles of attack drag is reduced due to the separation delay. Positioning the vortex generators closer towards the leading edge increases the drag at low angles of attack but at higher-angles of attack, the drag is significantly reduced. Also a slightly larger maximum lift coefficient is achieved and the stall angle is delayed further if the VGs are installed more downstream. From the reference data, one may conclude that the optimal vortex generator position for this airfoil is around 20%. The results of both codes show the same behaviour as the reference data. However, in XFOIL the effect of replacing the vortex generators from 20 to 30% chord is more pronounced. In Table 8.9, the error between both codes and the reference data are quantified.

In general, both codes show a good agreement with the measurement data especially in terms of maximum lift coefficient. The maximum lift coefficients are estimated within an accuracy of 3%. The stall angle deviates up till 12%, however, in clean case the stall angle predictions are already off up till 13%. More detailed information about the codes accuracy can be found in Table 8.9.

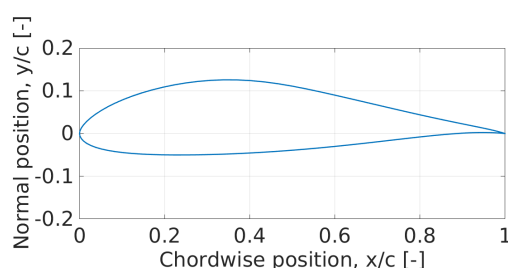


Figure 8.21: Cross-section of the AH93W174 airfoil.

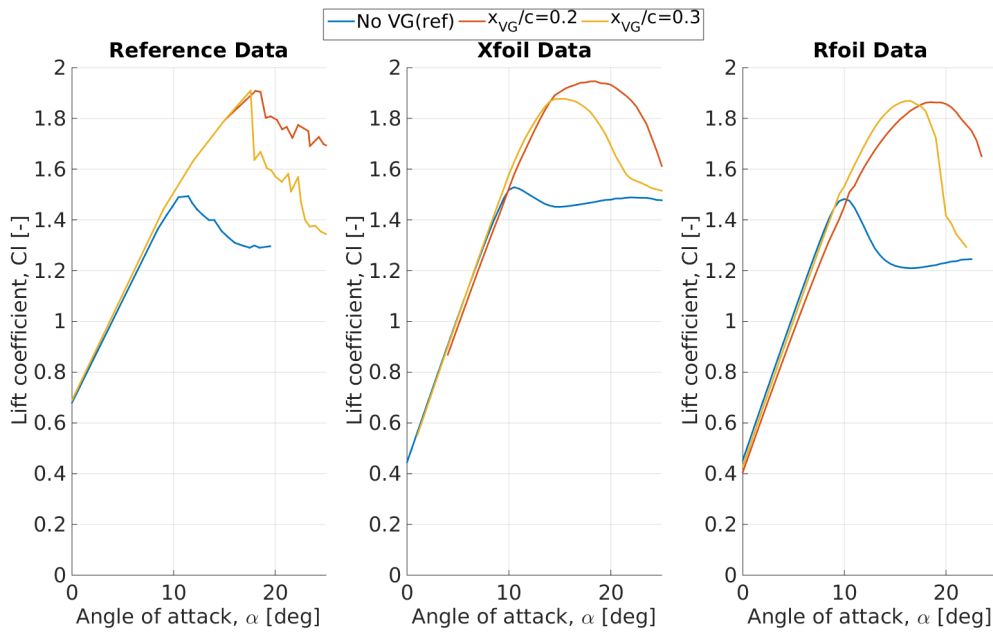


Figure 8.22: Lift polar of the AH93W174 airfoil at $Re = 1.3E6$ with $h = 9\text{mm}$, $l = 18\text{mm}$, $\beta = 18^\circ$ and varying position originating from measurements, XFOIL and RFOIL

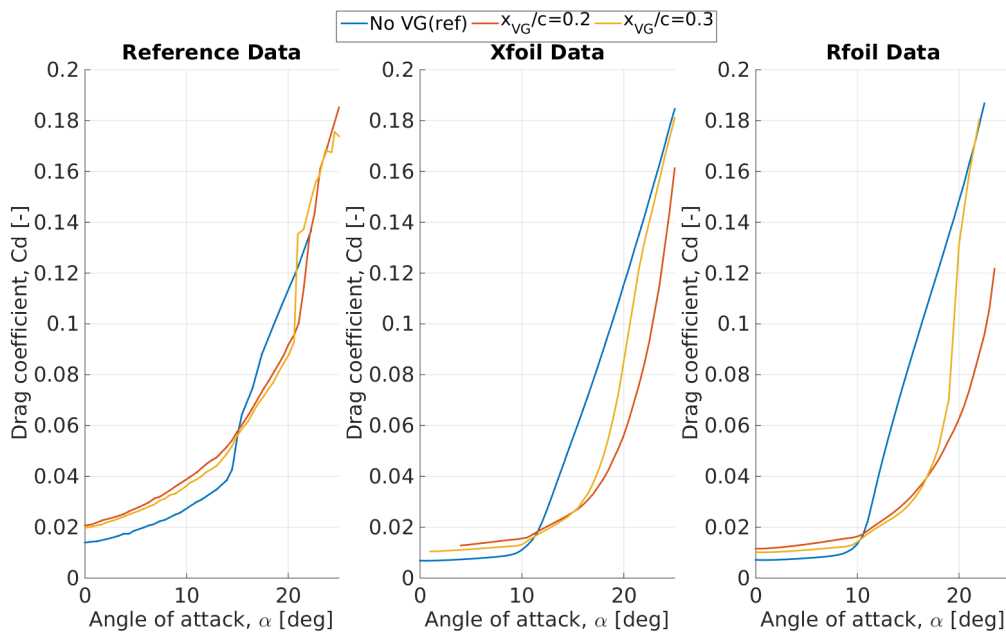


Figure 8.23: Drag polar of the AH93W174 airfoil at $Re = 1.3E6$ with $h = 9\text{mm}$, $l = 18\text{mm}$, $\beta = 18^\circ$ and varying position originating from measurements, XFOIL and RFOIL

Table 8.9: Error XFOIL and RFOIL in Figure 8.22

Case	Reference		Xfoil Error		Rfoil Error	
	Stall angle[deg]	Max lift[-]	Stall angle[-]	Max lift[-]	Stall angle[-]	Max lift[-]
Clean	11.45	1.49	-0.08	0.03	-0.13	-0.01
x/c=0.2	18.10	1.91	-0.01	0.02	0.08	-0.03
x/c=0.3	17.58	1.91	-0.12	-0.02	-0.09	-0.02

8.2.2 Madani Data Set

The second additional data set used to analyse the code robustness is collected from an article written by O.M. Fouatih⁹². In this article, a parametric study is conducted on different vortex generator geometrical parameters with the ultimate goal to optimise the flow separation control of a NACA4415 airfoil. The study is purely experimental. The experiments were carried out in a subsonic wind tunnel at a Reynolds number of $2E5$. The airfoil model had a NACA 4415 cross-section and a 0.152m chord length. The airfoil is plotted in Figure 8.24. Pressure distributions were obtained and used to compute lift and drag coefficients. Variations of vortex generator position, height and inflow angle are studied.

In Figure 8.25 and Figure 8.26, the lift and drag polar are presented of the NACA4415 with vortex generator installed at different positions. The polars are calculated using XFOIL and RFOIL and compared with measurement data. In these figures, the vortex generators all have the same shape, meaning a height of 5mm, length of 15mm and inflow angle of 10° . For all the cases studied, the effect of the vortex generators is mainly to reduce or completely remove the laminar separation bubble. These separation bubbles are formed over the airfoil due to the low Reynolds number. At the lower angles of attack, drag increases for vortex generators closer to the leading edge, however it is not very pronounced. According to the measurement data, the optimal location is shown to be at 40%. The general effect of adding vortex generators is captured well by both XFOIL and RFOIL. However, both codes identify $x/c = 0.3$ to be the optimal location. The maximum lift coefficient is predicted within 3% for XFOIL and within 7% for RFOIL. Note that for RFOIL the clean case lift is under predicted and thus the net effect of the vortex generator is over predicted. The net effect is better captured by XFOIL but with this code, stall is predicted too early. In Table 8.10, the accuracy of the codes is quantified.

Figure 8.27 and Figure 8.28 present the effect of increasing the vortex generator height on the lift and drag respectively. Three cases are considered: the clean case with no vortex generators, a case with 3mm vortex generators and one with 5mm vortex generators. Both vortex generator cases show an increase in lift where the largest effect is identified for the largest vortex generators. Similar observations are found by XFOIL and RFOIL. The lift increments due to the presence of the vortex generators are best predicted by XFOIL while the stall angles better agree for RFOIL. Details of the code accuracies are given in Table 8.11.

The last validation case is one with varying inflow angle. In Figure 8.29 and Figure 8.30, the lift and drag curve of three different inflow angles is presented. The used vortex generators have a fixed height of 5mm and a length over height ratio of 3. The vortex generator's leading edge is still at 30% of the chord. The reference data as well as the modelling results of both codes show that increasing the inflow angle results in an increasing maximum lift coefficient. The maximum lift coefficient predictions deviate only 3% for XFOIL and 7% for RFOIL from the measurements. The stall angle remains under predicted by XFOIL and the net effect of the vortex generators is over predicted by RFOIL. The code errors are presented in Table 8.12.

For the three different cases, similar conclusions can be drawn. RFOIL seems to over predict the net effect of adding vortex generators to the NACA4415. XFOIL better captures the net effect on the lift coefficient but tends to under predict the stall angle. For the drag calculations, no clear conclusions can be drawn except that similar results are found for XFOIL and RFOIL.

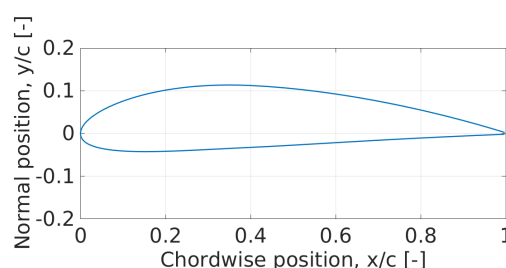


Figure 8.24: Cross-section of the NACA4415 airfoil.

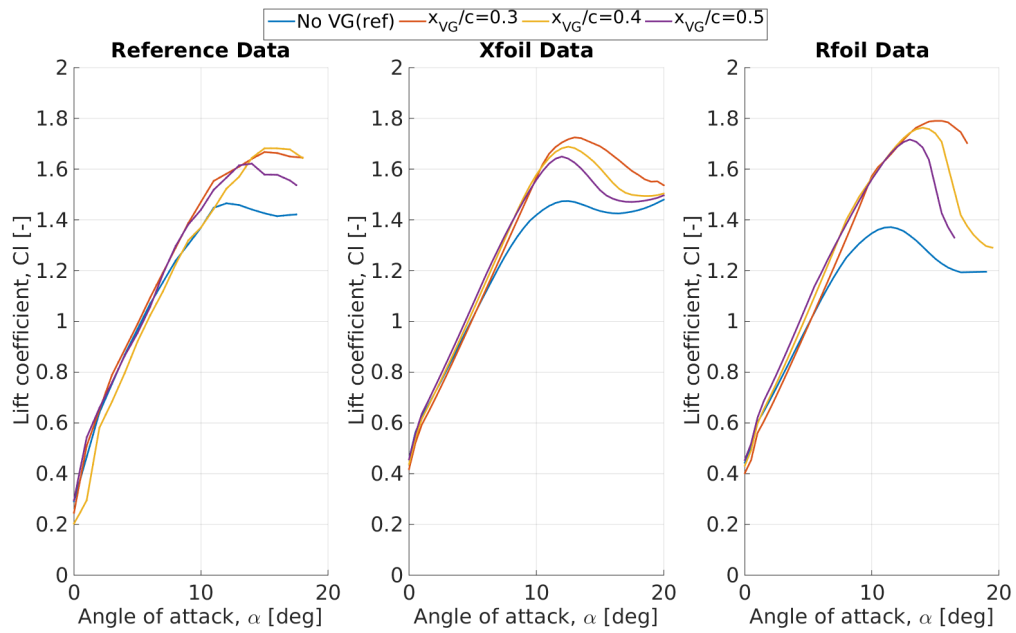


Figure 8.25: Lift polar of the NACA4415 airfoil at $Re = 2E5$ with $h = 5\text{mm}$, $l = 15\text{mm}$, $\beta = 10^\circ$ and varying position originating from measurements, XFOIL and RFOIL

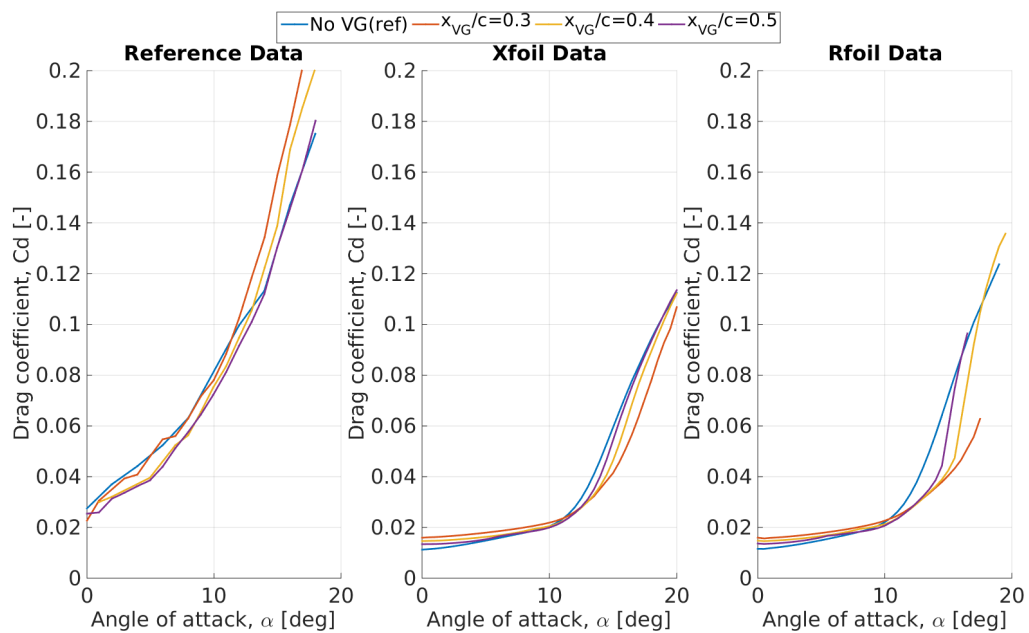


Figure 8.26: Drag polar of the NACA4415 airfoil at $Re = 2E5$ with $h = 5\text{mm}$, $l = 15\text{mm}$, $\beta = 10^\circ$ and varying position originating from measurements, XFOIL and RFOIL

Table 8.10: Error XFOIL and RFOIL in Figure 8.25

Case	Reference		Xfoil Error		Rfoil Error	
	Stall angle[deg]	Max lift[-]	Stall angle[-]	Max lift[-]	Stall angle[-]	Max lift[-]
Clean	12.00	1.47	0.00	0.00	-0.04	-0.07
x/c=0.3	15.00	1.67	-0.13	0.03	0.00	0.07
x/c=0.4	15.00	1.68	-0.17	0.00	-0.07	0.05
x/c=0.5	14.00	1.62	-0.14	0.02	-0.07	0.06

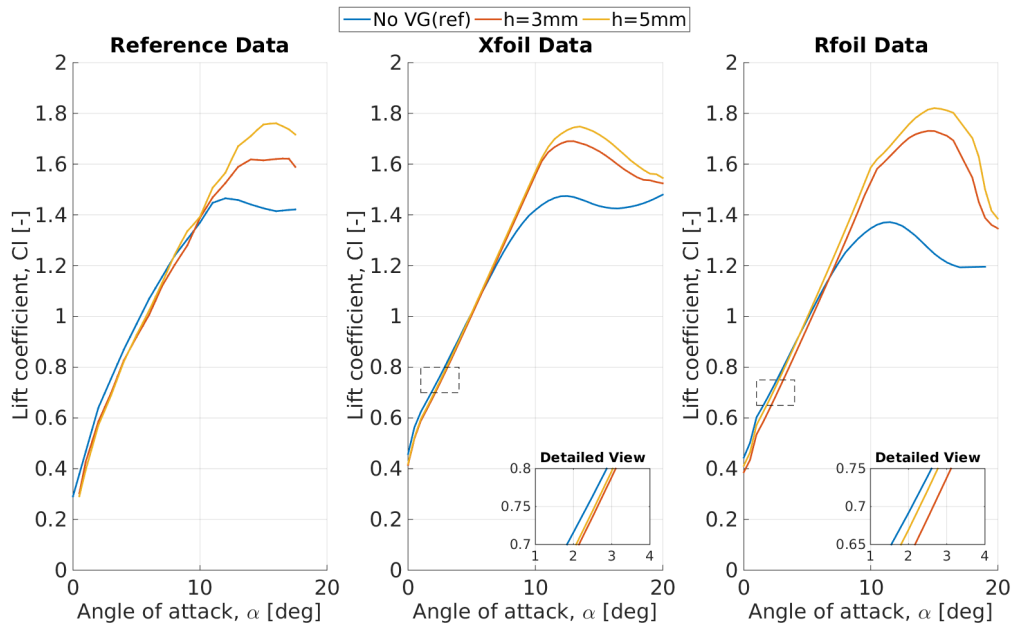


Figure 8.27: Lift polar of the NACA4415 airfoil at $Re = 2E5$ with $l = 3hmm$, $\beta = 20^\circ$, $x_{vg}/c = 0.3$ and varying height originating from measurements, XFOIL and RFOIL

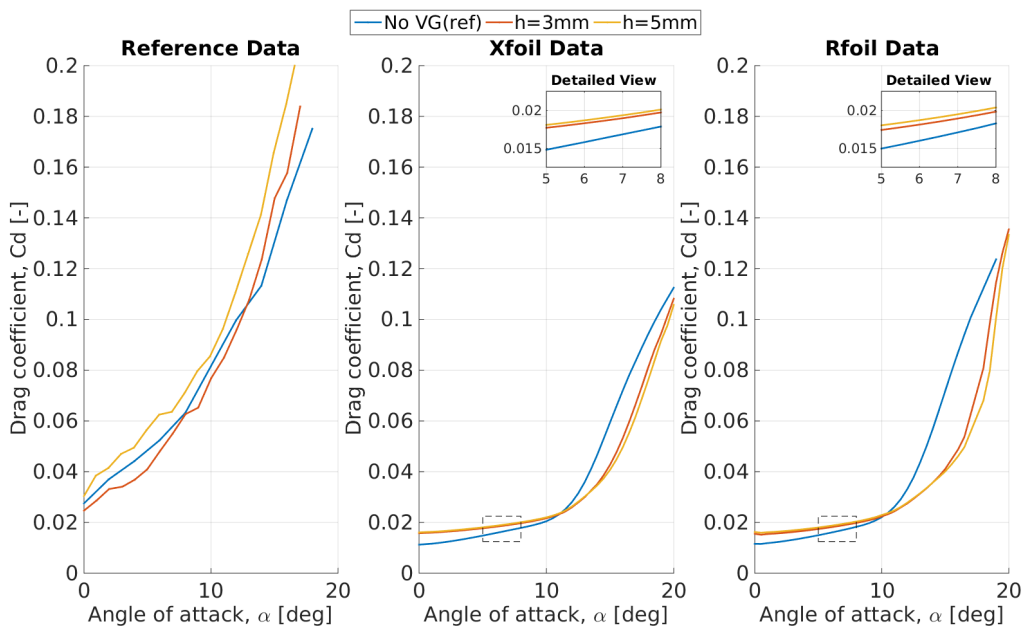


Figure 8.28: Drag polar of the NACA4415 airfoil at $Re = 2E5$ with $l = 3hmm$, $\beta = 20^\circ$, $x_{vg}/c = 0.3$ and varying height originating from measurements, XFOIL and RFOIL

Table 8.11: Error XFOIL and RFOIL in Figure 8.27

Case	Reference		Xfoil Error		Rfoil Error	
	Stall angle[deg]	Max lift[-]	Stall angle[-]	Max lift[-]	Stall angle[-]	Max lift[-]
Clean	12	1.47	0.00	0.00	-0.04	-0.07
h=3	14	1.62	-0.11	0.04	0.04	0.07
h=5	16	1.76	-0.16	-0.01	-0.06	0.03

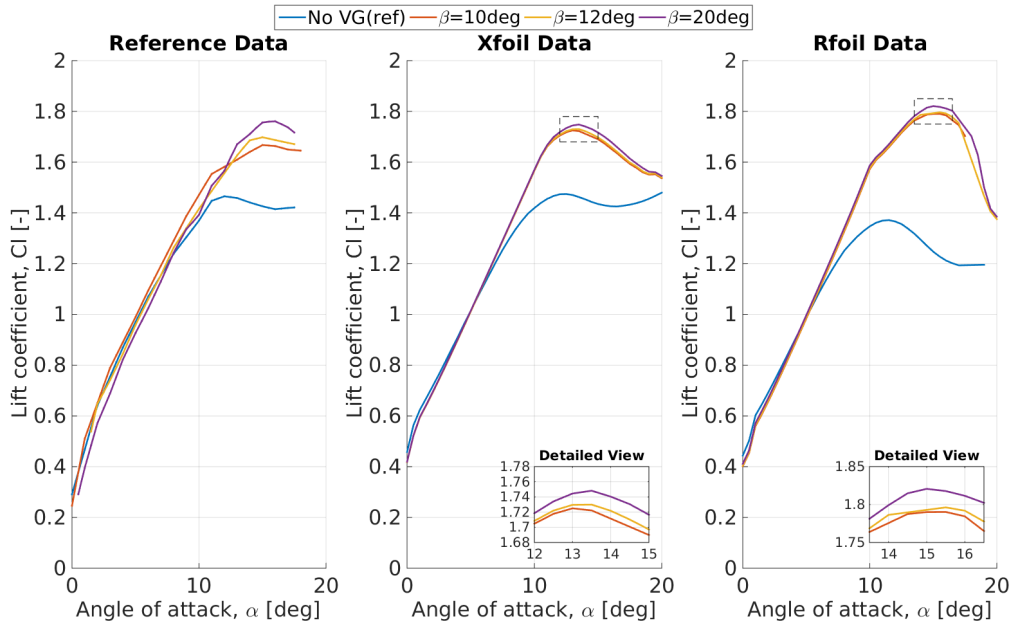


Figure 8.29: Lift polar of the NACA4415 airfoil at $Re = 2E5$ with $h = 5\text{mm}$, $l = 15\text{mm}$, $x_{vg}/c = 0.3$ and varying inflow angle originating from measurements, XFOIL and RFOIL

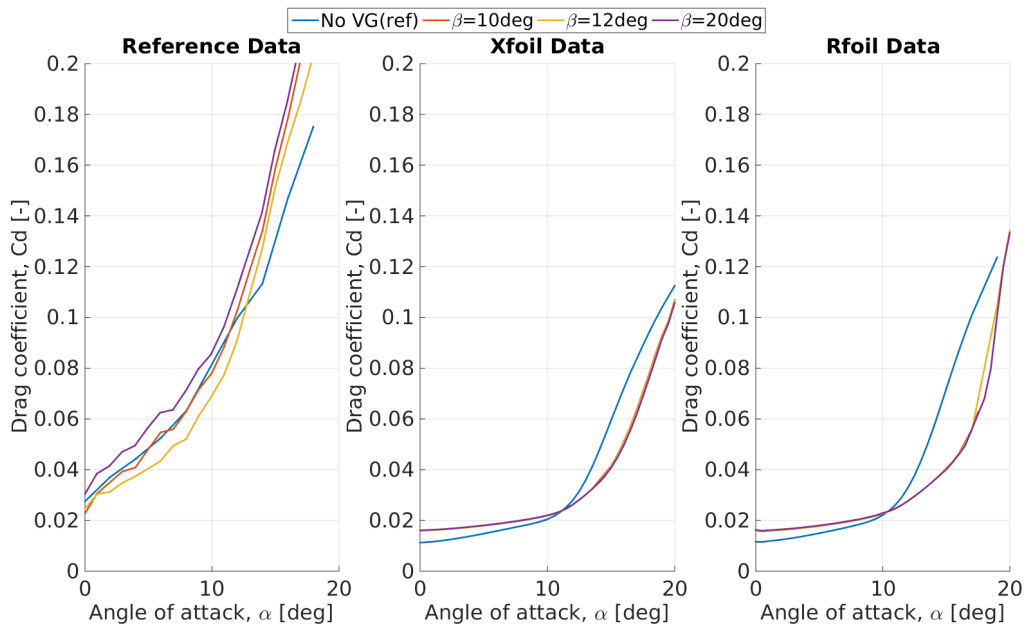


Figure 8.30: Drag polar of the NACA4415 airfoil at $Re = 2E5$ with $h = 5\text{mm}$, $l = 15\text{mm}$, $x_{vg}/c = 0.3$ and varying inflow angle originating from measurements, XFOIL and RFOIL

Table 8.12: Error XFOIL and RFOIL in Figure 8.29

Case	Reference		Xfoil Error		Rfoil Error	
	Stall angle[deg]	Max lift[-]	Stall angle[-]	Max lift[-]	Stall angle[-]	Max lift[-]
Clean	12.00	1.47	0.00	0.00	-0.04	-0.07
$\beta=10$	15.00	1.67	-0.13	0.03	0.00	0.07
$\beta=12$	15.00	1.70	-0.13	0.02	0.03	0.06
$\beta=20$	16.00	1.76	-0.16	-0.01	-0.06	0.03

8.3 Evaluation & Limitations

The above observations allow to evaluate the performance of the modified integral boundary-layer codes and to identify the code limitations. The results will be combined and conclusions will be drawn. The performance of both codes will be discussed systematically by firstly pointing out the general observations and consequently translating these observations into a general evaluation. Some additional limitations will be discussed and at the end a clear conclusion will be drawn.

By combining the validation results of both the data sets used to set up the empirical relation as well as the external data sets obtained from literature, some general observations can be made. Observations regarding maximum lift coefficient, stall angle, drag coefficient and convergence will be pointed out for XFOIL and RFOIL.

- **Maximum lift coefficient:** During the source term optimisation process, one of the most determinant parameters was the lift coefficient. Therefore also in the validation process, major attention is drawn to the capability to model this parameter properly. A good reference is to consider the maximum lift coefficient that can be obtained. It is observed that when all validation data is considered, XFOIL can predict this value with a certainty of 90% within an accuracy range of 7%. RFOIL is less accurate in modelling the maximum lift coefficient. With this code the accuracy remains within a range of 9% for 90% of the cases. However, this is excluding the validation data sets where the airfoils are equipped with vortex generators before 30% of the chord. For RFOIL it seems to be a trend that placing the VGs before 30% of the chord, introduces more error in the calculations. The modelling error of XFOIL does not seem to be related to airfoil or vortex generator properties. The error probability distributions are presented in Figure 8.31 and Figure 8.32. It was also remarkable that the net effect of the vortex generator, i.e the difference between the clean airfoil and the airfoil equipped with vortex generators is most often over predicted by RFOIL. XFOIL deals significantly better with it.
- **Stall angle:** The error of the stall angle found by XFOIL and RFOIL is more difficult to standardise. On average, larger errors exist in the stall angle modelling than in the prediction of the maximum lift coefficient, but no clear trend could be identified. The difference in stall angle between the modelling results and the reference data go up till 20%. However, this value should be put in perspective, since in clean case the stall angle predictions are already off. The stall angle error of the cases with vortex generators remain within the same range as was the case for the clean airfoil predictions. This is true for both XFOIL as RFOIL.
- **Drag coefficient:** The drag coefficient is consistently under predicted. This is true for clean airfoil calculations as well as in cases the airfoil is equipped with vortex generators. The net increment in drag by adding vortex generators is lower than it should be due to the lag in modelling the parasitic drag of the vortex generator itself.
- **Convergence:** The additional source term added to the closure relations did not introduce significant convergence problems to any of the codes. However, XFOIL shows small convergence issues at low angles of attack in case vortex generators are positioned too close to the leading edge (i.e upstream of the 20% chord length). The modified RFOIL code encounters some convergence issues in the post-stall region.

The above general observations can now be evaluated and if possible related back to assumptions or decisions made in the methodology part of this work. Two main points should be highlighted in the evaluation. First of all, a clear reasoning can be built around the fact that XFOIL seems to better perform than RFOIL especially in the maximum lift modelling. This was already predicted in subsection 7.2.4 and is now also proven. The author has less confidence in the empirical relation set up for RFOIL, especially due to the sign of the regression coefficient accompanying the momentum thickness. The reason for this is related to the fact that the aerodynamic performance of two clean airfoils that form a large part of the data base are badly modelled by RFOIL when compared to reference data. For these two airfoils, the additional source term is not only anticipating for the net effect of the vortex generators but it also accounts for the error already existing in clean airfoil case. This raises questions to the generality and robustness of the found expression. XFOIL seems to not suffer from this issue

and therefore the predictions are better. A second observation interesting to point out is that drag is systematically under estimated. This is also as expected since the physical presence of the vortex generators device itself in the flow is not taken into account. The vortex generators introduce an additional profile drag and this is not yet incorporated in the integral boundary-layer codes. The profile drag depends on the vortex generator configuration and the flow it is encountering.

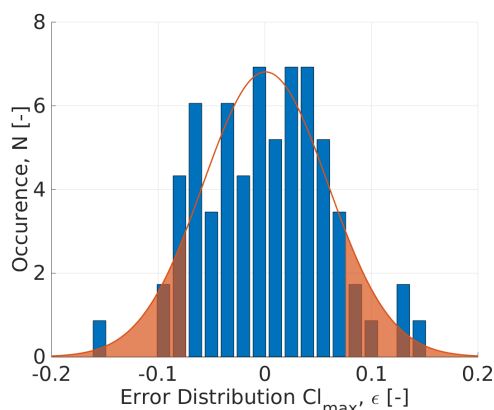


Figure 8.31: Probability density function of the error in maximum lift coefficient obtained by XFOIL. Unshaded area indicated 90% confidence interval.

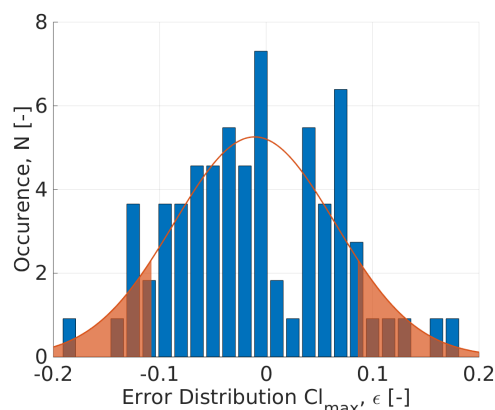


Figure 8.32: Probability density function of the error in maximum lift coefficient obtained by RFOIL. Unshaded area indicated 90% confidence interval.

Besides the observations of the validation process, one should keep in mind other limitations of the current source term approach. Firstly, a lot of this research builds on the reference data. The performance of the codes is thus limited to the quality of the data sets. Experiments are subjected to wind tunnel corrections and phenomenon such as 3D separation might influence the lift and drag measurements. Also, CFD have limitations on itself in predicting separation and hence stall and the maximum lift coefficient. A second limitation is that codes such as XFOIL and RFOIL are two-dimensional codes. However, the flow field behind a vortex generator is fully three-dimensional. The lift and drag that may be calculated using these integral boundary-layer codes represents a spanwise average while in reality lift and drag vary in a sinusoidal way in spanwise direction. This behaviour cannot be captured by the codes, but this is not necessarily the purpose. Although the lift and drag values might represent spanwise average values, a more in depth analysis is necessary to validate if this is also through for the integral boundary-layer parameters. Besides that, remember that not all vortex generator geometric parameters are already included in the source term empirical relation. No distinction is made between for example different internal and external vortex generator pair distances while it is definitely expected that these parameters influence lift and drag. Not enough reliable validation data was available to accurately incorporate its effect in the source term relation. A fourth limitation is related to transition. In the beginning of this thesis an assumption is made stating that all vortex generators are able to force the flow to transition from a laminar boundary-layer into a turbulent one. This statement is not verified but for the used data base it is not expected to influence the results. Finally, one should again be reminded that the source term approach is an engineering approach and this will always come together with limitations.

According to the complete validation process, one may conclude that both codes are able to predict the aerodynamic performance of an airfoil equipped with vortex generators within an acceptable accuracy. Both codes are capable to address the effect of vortex generator height, length, inflow angle and chordwise position. The resulting lift polars showed a good agreement with measurement data. XFOIL in particular is demonstrated to be robust and able to model different airfoil families at a wide range of Reynolds numbers. Although both codes can still be improved, a great step is taken towards the modelling of vortex generators within the integral boundary-layer theory. The author believes that the source term concept is very promising and can be elaborated further to improve its modelling capabilities even more.

9

Recommendations & Further Work

Although great steps are taken in this master thesis towards the modelling of vortex generators within the integral boundary-layer theory, some improvements can still be done. In this chapter, three recommendations will be given that could be worth studying further. The recommendations concern the data base used to set up the source term empirical relation, the effect of vortex generators on the friction coefficient and the role and value of adding a transition model.

9.1 Enlarge Data Base

The measurement and CFD data sets studying the effect of vortex generators on airfoils play an important role in the set up of the source term empirical relation. The reference data should originate from a reliable source but this is not enough. XFOIL and RFOIL do a great job in modelling the clean airfoil aerodynamic properties, however, an error is still existing. This error makes the optimisation process of the source term more difficult. To anticipate for the clean airfoil error, a correction factor has been applied but this correction can not fully remove the clean case error. Especially for some airfoils, the clean case error is too large.

Therefore, to improve the theoretical value of the source term empirical relation and thus to improve the performance of the integral boundary-layer codes, it is advised to extend the reference data base. There is a need for data studying the behaviour of an airfoil that is modelled with maximum accuracy in clean case. The airfoil selection and flow conditions are of major importance since XFOIL and RFOIL are particularly applicable for low Reynolds number airfoils.⁷¹ Both codes also perform better for thin airfoils with a thin trailing edge. If the available data set would be extended with a parametric study on an appropriate airfoil, the author believes that the source term definition will follow more closely to theories and the trend of the theoretical circulation produced by the vortex generators.

Besides selecting a proper airfoil, it is also advised to perform an extensive parametric study. All vortex generator parameters should be varied in a consistent way. Ideally, the vortex generator height, length and inflow angle should be varied from relatively low to rather high values to capture their effect clearly. For some of the data sets, the variation of the various parameters was too limited. To incorporate the effect on internal and external vortex generator pair distance, also these parameters should be included in the parametric study. In this thesis work, the emphasis has been on the modelling of counter-rotating vane type vortex generators, however, if enough reference data is available, the model could be extended to also cope for other vortex generator types.

9.2 Friction Coefficient

Adding vortex generators to an airfoil, affects the boundary-layer behaviour. The boundary-layer properties are changing due to the presence of this flow control device. One of the expected changes is that the friction coefficient will increase at the location of the vortex generator. Due to the introduction of the vortices, the flow becomes more turbulent and the velocity profile becomes fuller. This is associated with an increase in shear stress and thus in friction coefficient.

The modelling of vortex generators is in this thesis realised by increasing the dissipation coefficient through the shear stress coefficient. Modifying this parameter has a direct effect on the energy equation. The velocity profiles are changing accordingly and this will indirectly also have its effect on the momentum equation. The added source term is thus able to cause the friction coefficient to increase simultaneously. However, the closure relation of the friction coefficient used by XFOIL and RFOIL are derived for a 2D flow. These equations are not necessarily valid any more for 3D flow fields behind vortex generators. It is thus necessary to verify this and if necessary derive a new closure relation for

the friction coefficient.

To present the effect of changing the friction coefficient closure relation, a basic sensitivity analysis is performed. The skin friction equation is adapted as such that a multiplication factor is added to the equation. This factor is activated for all chordwise positions downstream the vortex generator. A fixed source term of strength 0.1 and decay 150 is introduced and the lift and drag curves are compared for different multiplication factors. In Figure 9.1 and Figure 9.2, these lift and drag polar are presented. The adaptations were introduced in RFOIL but similar results are expected from XFOIL. The graphs compare three different multiplication values: a multiplication factor of 1.0 as a reference, a multiplication factor of 2.0 and one with factor 3.0.

This sensitivity analysis already proves that increasing the friction coefficient independently may be a possible solution to model the vortex generator profile drag. The drag significantly increases with increasing multiplication factor. Since the drag increases, the lift consequently decreases. The lift curve slope decreases and the maximum lift coefficient drops. Note that the values of the multiplication factors selected in this sensitivity analysis are exaggerated but this is done to clearly show the effect of it. The magnitude of the multiplication factor will need to be determined carefully. The author expects that the multiplication factor will most probably depend on the vortex generator configuration and flow properties at the vortex generator location since these two parameters influence how much additional profile drag is added due to the presence of the vortex generator. To determine the exact relation, more work needs to be performed.

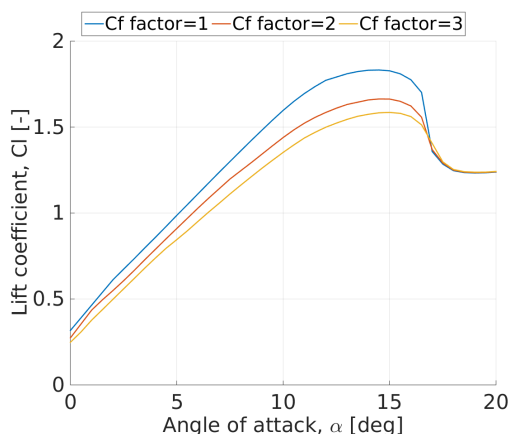


Figure 9.1: Lift polar for three different skin friction multiplication factors for the DU97W300 airfoil at a Reynolds number of $2E6$ with fixed source term.

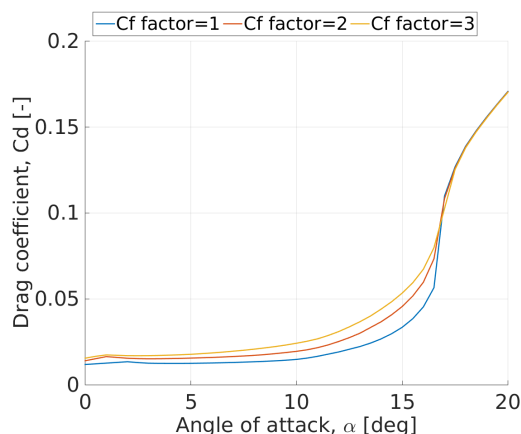


Figure 9.2: Drag polar for three different skin friction multiplication factors for the DU97W300 airfoil at a Reynolds number of $2E6$ with fixed source term.

9.3 Laminar-Turbulent Transition Model

The last recommendation regards a transition model. To make the vortex generator model more accurate in predicting the vortex generator effect on the boundary-layer, a transition model could be incorporated. The model should be able to determine if the vortex generators are capable to promote a bypass type transition at the location of the vortex generators. The question necessary to be answered is whether the height of the vortex generators relative to the boundary-layer thickness is large enough to force the flow to transition from a laminar boundary-layer to a turbulent one.

Kerho and Kramer¹ suggest in their article a possible method to define transition. A vortex generator can be seen as a form of roughness. This roughness cannot be modelled accurately using the standard transition models incorporated in XFOIL or RFOIL. Kerho and Kramer, therefore, specified a transition criteria. The vortex generator roughness based Reynolds number is determined based on the local velocity in the undisturbed boundary-layer and the height of the vortex generator. Consequently, this value is then compared to the critical Reynolds number at which transition would occur. If the roughness based Reynolds number exceeds the critical Reynolds number, it is assumed that that the current height of the vortex generator is sufficient for the vortex generator to promote a bypass transition. If this is true, transition is fixed in the boundary-layer codes at the location of the vortex generators. If not, no adaptations are made and free transition is assumed.

The method proposed by Kerho and Kramer¹ is one example to deal with this issue but it is believed

that also other methodologies could be used. Whether transition is promoted by the vortex generators or not remains an interesting topic in which still a lot of research can be done. However, the value of adding a proper transition model might not necessarily be considered as a priority. In most application, the risk of having too small vortex generators such that transition is not triggered, is relatively small.

10

Conclusion

Within this master thesis, the feasibility to model the effect of the vortex generators using the integral boundary-layer theory is analysed. Steps are made towards the development of XFOILVG and RFOILVG. This report consists of four main parts (Introduction, Methodology, Results and Discussion) of which the main conclusions are presented in this final chapter.

10.1 Part 1: Introduction

Vortex generators are often used in the wind energy industry to control the flow over the blades. They generate a vortex characterised by an initial strength just downstream of the device, the streamwise decay of the vortex strength and the vortex trajectory. The generated streamwise vortices at the free tips of the vortex generators increase the mixing between the high-energy layers in the outer part of the boundary-layer and the low energy regions near the walls. The energetic, rapidly moving air from outside is drawn into the slow-moving boundary-layer and increases so the near-wall momentum. This re-energising process can make the boundary-layer turbulent (if the vortex generator is operating in a laminar boundary-layer) which makes the boundary layer in general more able to handle steeper and larger adverse pressure gradients and is thus more resistant to flow separation than laminar ones. Vortex generators come in different shapes and sizes with as most important parameters the device geometry, size, orientation and location.

In order to assess and optimise the use of vortex generators, there is a need to accurately model the effect of these devices. Several models are already presented in literature, most of which use computational fluid dynamics. The most intuitive approach is to fully resolve the vortex generator, however, most models try to model the effect of the device without including their geometry explicitly in the computational mesh (i.e. the (j)BAY model, the vortex-source model, the statistical method and Smith's method). Although remarkable advances are made in the modelling of vortex generators using computational fluid dynamic techniques, these techniques are still very expensive and impractical to use in iterative design processes. Modelling vortex generators in a more cost and time efficient way could be achieved by using integral boundary-layer codes. One academic work written by Kerho and Kramer is found that deals with this. They suggested to model the mixing effect of the device by modifying the stress transport formulation through the rate equation based on a source term approach. Kerho and Kramer¹ remained very qualitative and gave a rather vague description of the modifications applied to XFOIL. Also, their model was calibrated for one specific case. No attempts were done to extend their approach such that the aerodynamic behaviour of different vortex generator configurations and flow conditions could be predicted. Further, the region of interest of Kerho and Kramer (i.e. airfoil choice and flow condition) were different than the one aimed for in the wind energy industry. The combination of these aspects identifies the research gap.

10.2 Part 2: Methodology

A methodology used to model the effect of vortex generators into integral boundary-layer codes (e.g. XFOIL and RFOIL) is building further on the work of Kerho and Kramer. In this master thesis research, their work is revised carefully and elaborated further.

The source term approach relies on adding an additional source term to the closure relations. This source term is added to the shear-lag equation, to account for the increase in dissipation due to the streamwise vortices shed by the vortex generators. More specifically, the source term is implemented to the equilibrium shear stress coefficient. This coefficient is the fundamental parameter of the shear-lag equation and represents the shear stress that would correspond to the value if the local boundary-layer would be in equilibrium. It is concluded that this location was favourable considering the con-

vergence speed and stability of the integral boundary-layer codes. The source term shape function is selected as such that it is mimicking the downstream decay of the vortex strength generated by the vortex generator. In contrary to what Kerho and Kramer proposed, the source term shape function was selected as such that it is first gradually developing after which it starts to exponentially decay. The source term expression is given by three variables: the source term strength, the decay rate and the location of the vortex generators. Vortex generators most often trip the flow to transition from a laminar to a turbulent boundary-layer. XFOIL and RFOIL are adapted as such that when the vortex generators are positioned before the free transition location, the flow will automatically be forced to transition at the location of the vortex generators. This is realised by using the built-in command for forced transition. The source term approach is implemented into XFOIL and RFOIL and the modifications are verified by analysing the effect of adding a source term on the boundary-layer properties. The verification process concluded that the source term approach is representing similar effects to the ones introduced by vortex generators.

To elaborate the source term approach, reference data is gathered for different airfoil/vortex generator configuration. The reference data base originates from experimental and numerical campaigns that are either performed during this thesis or adopted from external sources. As part of this thesis, a wind tunnel experiment is done led by D. Baldacchino in the Low Speed Low Turbulence wind tunnel of Delft University of Technology. In this experimental campaign, a DU97W300 airfoil equipped with different configurations of vortex generators is tested at Reynolds numbers between $1E6$ and $3E6$. The effect of varying particular configuration parameters are concluded and the three-dimensional flowfield behind vortex generators is presented. To enlarge the database and span more airfoil families and Reynolds numbers, additional data sets are adopted from studies of W.A. Timmer et al., M. Manolesos et al. and the Avatar project.

10.3 Part 3: Results

Besides the improved source term approach, the most novel part of this thesis is presented in the result section. The exact value of the source term strength and decay needs to be determined for a specific airfoil/vortex generator configuration. A calibration process is set up, such that for every measurement point, meaning for one defined vortex generator configuration installed on that particular airfoil under specifically set flow conditions, an optimal source term can be defined.

This calibration process consists of three main steps. First of all, a brute-force optimisation approach is applied to analyse the effect of the source term variables on lift and drag properties. It is concluded that multiple combinations of source term strength and decay predict the same lift and drag coefficient. It has been established that all these combinations of strength and decay constants have in common that their prescribed integral is equal. Introducing the source term integral made it possible to reduce the number of unknowns from two (strength σ_0 and decay λ) to one and thus simplify the problem. In the second step in the calibration process, the aerodynamic properties expected to be found by the airfoil codes need to be determined. This is referred to by the *target polar*. The target polar is set up by adding a correction factor to the reference data. This correction factor accounts for the slope difference existing in clean case between the codes on one hand and reference data on the other. This engineering approach assumes that the same error will be present between the reference data and the X/RFOIL data in the case without and with vortex generators. The last step combines the results of the previous two steps and identifies the optimal source term. The determination of the optimal source term is mainly based on the lift coefficient. Given the available dataset and code limitations, lift is the best suited quantity to determine the source term.

All the optimal source terms determined for specific airfoil/vortex generator configurations, are combined to define an empirical relation that relates the value of the source term to vortex generator geometry parameters and boundary-layer parameters. This is done for both XFOIL and RFOIL using a weighted multiple variable linear regression approach. The dependent variable is the source term integral and the independent variables are the non-dimensional vortex generator height and length, inflow angle, local flow velocity and momentum thickness. These parameters are selected based on the reasoning that they are directly related to the definition of circulation for a flat plate and assuming that the source term magnitude follows the amount of circulation produced. The weight matrix is set up using an error criterion that describes the goodness of the clean case predictions. The regression is consequently performed by filtering the data sets on outliers and focussing on the higher angles of attack.

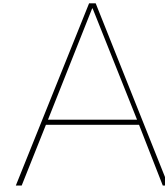
From the results, it is concluded that the source term seems to be, until a certain extent, related to the circulation produced by the vortex generator. The regression coefficients accompanying the vortex generator configuration properties follow the definition of circulation. The effect of the boundary-layer properties on the source term slightly deviates from the expectations. It is found that the source term magnitude is inversely proportional to the local flow velocity and that the sign of the coefficient corresponding to the momentum thickness is opposite for XFOIL as for RFOIL. The coefficients for XFOIL are in closer agreement with the expectations. Potential explanations are identified for this. The set of closure relations used, the error in the clean airfoil modelling, the use of internally calculated parameters and the role of the reference data and correction factor, cause an accumulation of uncertainties. These uncertainties influence the source term calibration process and make it too hopeful to fully relate the required source term to the theoretical circulation produced by the vortex generators. The source term approach still remains an engineering approach to model vortex generators.

10.4 Part 4: Discussion

The source term empirical relation is implemented into the integral boundary-layer codes XFOIL and RFOIL and the two models are validated extensively. The validation process consists of two parts. As first step in the validation process, the source term empirical relation is validated by analysing the predictions of the data sets that were used to set up the source term relation. In the second part of the validation, external reference data, adopted from literature, are used to prove the robustness of the code. The validation results are discussed and the following conclusions are drawn. XFOIL can predict the maximum lift coefficient with a certainty of 90% within an accuracy range of 7%. RFOIL slightly performs less and the maximum lift coefficient is modelled within an accuracy range of 9% for 90% of the cases. For RFOIL, it seems to be a trend that placing the vortex generators before 30% of the chord, introduces more error in the calculations. The error of the stall angle found by Xfoil and RFOIL remains within the same range as was the case for the clean airfoil. The drag coefficient is consistently under predicted since the profile drag of the vortex generators is not included into the model. Further, adding the source term to the closure relations did not introduce significant convergence problems to any of the codes.

According to the complete validation process, one may conclude that both codes are able to predict the aerodynamic performance of an airfoil equipped with vortex generators within an acceptable accuracy. Both codes are capable to address the effect of vortex generator height, length, inflow angle and chordwise position. The resulting lift polars showed a good agreement with the reference data. XFOIL, in particular, is demonstrated to be robust and able to model different airfoil families at a wide range of Reynolds numbers.

This thesis has finally led to the development of the foundations of the design tool XFOILVG and RFOILVG. Although both codes can still be improved, great steps are taken towards the modelling of vortex generators within the integral boundary-layer theory. Based on the presented results, one may conclude that the source term approach is very promising and can be elaborated further by incorporating the recommendations.



Reference Data Base

In this appendix, an overview will be given of the available data sets. It contains all necessary information about the airfoil model, vortex generator configuration and flow properties.

A.1 Wind Tunnel Experiment (Experimental data)

No.	Airfoil model		VG configuration							Flow properties		
	Airfoil	Chord length [m]	Shape	Rotation	height [mm]	length [mm]	Internal distance [mm]	External distance [mm]	Inflow angle [deg]	Position [x/c]	Reynolds number [-]	Transition
LTT01	DU97W300	0.65	Delta	Counter	5	15	17.5	35	15	0.1	2.0E6	Free
LTT02	DU97W300	0.65	Delta	Counter	5	15	17.5	35	15	0.2	2.0E6	Free
LTT03	DU97W300	0.65	Delta	Counter	5	15	17.5	35	15	0.3	2.0E6	Free
LTT04	DU97W300	0.65	Delta	Counter	5	15	17.5	35	15	0.4	2.0E6	Free
LTT05	DU97W300	0.65	Delta	Counter	5	15	17.5	35	15	0.5	2.0E6	Free
LTT06	DU97W300	0.65	Delta	Counter	10	30	35	70	15	0.2	2.0E6	Free
LTT07	DU97W300	0.65	Delta	Counter	10	30	35	70	15	0.3	2.0E6	Free
LTT08	DU97W300	0.65	Delta	Counter	10	30	35	70	15	0.4	2.0E6	Free
LTT09	DU97W300	0.65	Delta	Counter	10	30	35	70	15	0.5	2.0E6	Free
LTT10	DU97W300	0.65	Delta	Counter	5	15	17.5	35	15	0.2	1.0E6	Free
LTT11	DU97W300	0.65	Delta	Counter	5	15	17.5	35	15	0.4	1.0E6	Free
LTT12	DU97W300	0.65	Delta	Counter	10	30	35	70	15	0.2	1.0E6	Free
LTT13	DU97W300	0.65	Delta	Counter	10	30	35	70	15	0.4	1.0E6	Free
LTT14	DU97W300	0.65	Delta	Counter	5	15	17.5	35	15	0.2	3.0E6	Free
LTT15	DU97W300	0.65	Delta	Counter	5	15	17.5	50	15	0.2	2.0E6	Free
LTT16	DU97W300	0.65	Delta	Counter	5	15	17.5	35	12	0.2	2.0E6	Free
LTT17	DU97W300	0.65	Delta	Counter	5	15	17.5	35	18	0.2	2.0E6	Free
LTT18	DU97W300	0.65	Delta	Counter	5	15	17.5	35	15	0.1	2.0E6	Forced
LTT19	DU97W300	0.65	Delta	Counter	5	15	17.5	35	15	0.2	2.0E6	Forced
LTT20	DU97W300	0.65	Delta	Counter	5	15	17.5	35	15	0.3	2.0E6	Forced
LTT21	DU97W300	0.65	Delta	Counter	5	15	17.5	35	15	0.4	2.0E6	Forced
LTT22	DU97W300	0.65	Delta	Counter	5	15	17.5	35	15	0.5	2.0E6	Forced
LTT23	DU97W300	0.65	Delta	Counter	10	30	35	70	15	0.2	2.0E6	Forced
LTT24	DU97W300	0.65	Delta	Counter	10	30	35	70	15	0.3	2.0E6	Forced
LTT25	DU97W300	0.65	Delta	Counter	10	30	35	70	15	0.4	2.0E6	Forced
LTT26	DU97W300	0.65	Delta	Counter	10	30	35	70	15	0.5	2.0E6	Forced

A.2 TUD (experimental data)

No.	Airfoil model		VG configuration							Flow properties		
	Airfoil	Chord length [m]	Shape	Rotation	height [mm]	length [mm]	Internal distance [mm]	External distance [mm]	Inflow angle [deg]	Position [x/c]	Reynolds number [-]	Transition
TUD01	DU91W2250	0.6	Delta	Counter	5	17	10	35	16.4	0.2	2.0E6	Free
TUD02	DU91W2250	0.6	Delta	Counter	5	17	10	35	16.4	0.3	2.0E6	Free
TUD03	DU93W210	0.6	Delta	Counter	5	17	10	35	16.4	0.2	1.0E6	Free
TUD04	DU93W210	0.6	Delta	Counter	5	17	10	35	16.4	0.4	1.0E6	Free
TUD05	DU93W210	0.6	Delta	Counter	5	17	10	35	16.4	0.6	1.0E6	Free
TUD06	DU97W300	0.6	Delta	Counter	5	17	10	35	16.4	0.2	2.0E6	Free
TUD07	DU97W300	0.6	Delta	Counter	5	17	10	35	16.4	0.4	2.0E6	Free

A.3 AVATAR (CFD numerical data)

No.	Airfoil model		VG configuration							Flow properties		
	Airfoil	Chord length [m]	Shape	Rotation	height [mm]	length [mm]	Internal distance [mm]	External distance [mm]	Inflow angle [deg]	Position [x/c]	Reynolds number [-]	Transition
AVA01	DU331	6.06	Delta	Counter	10	30	20	50	20	0.25	1.6E7	Forced
AVA02	DU331	6.06	Delta	Counter	12	36	24	60	20	0.25	1.6E7	Forced
AVA03	DU331	6.06	Delta	Counter	15	45	30	75	20	0.25	1.6E7	Forced
AVA04	DU331	6.06	Delta	Counter	18	54	36	90	20	0.25	1.6E7	Forced
AVA05	DU331	6.06	Delta	Counter	30	90	60	150	20	0.25	1.6E7	Forced
AVA06	DU331	6.06	Delta	Counter	36	108	72	180	20	0.25	1.6E7	Forced
AVA07	DU331	6.06	Delta	Counter	60	180	120	300	20	0.25	1.6E7	Forced
AVA08	DU331	6.06	Delta	Counter	15	45	30	75	20	0.3	1.6E7	Forced
AVA09	DU331	6.06	Delta	Counter	18	54	36	90	20	0.3	1.6E7	Forced
AVA10	DU331	6.06	Delta	Counter	30	90	60	150	20	0.3	1.6E7	Forced
AVA11	DU331	6.06	Delta	Counter	36	108	72	180	20	0.3	1.6E7	Forced
AVA12	DU331	6.06	Delta	Counter	60	180	120	300	20	0.3	1.6E7	Forced
AVA13	DU331	6.06	Delta	Counter	15	45	30	75	20	0.4	1.6E7	Forced
AVA14	DU331	6.06	Delta	Counter	18	54	36	90	20	0.4	1.6E7	Forced
AVA15	DU331	6.06	Delta	Counter	30	90	60	150	20	0.4	1.6E7	Forced
AVA16	DU331	6.06	Delta	Counter	36	108	72	180	20	0.4	1.6E7	Forced
AVA17	DU331	6.06	Delta	Counter	60	180	120	300	20	0.4	1.6E7	Forced
AVA18	DU331	6.06	Delta	Counter	90	270	180	450	20	0.4	1.6E7	Forced
AVA19	FFAW3333	5.84	Delta	Counter	10	30	20	50	20	0.25	1.4E7	Forced
AVA20	FFAW3333	5.84	Delta	Counter	12	36	24	60	20	0.25	1.4E7	Forced
AVA21	FFAW3333	5.84	Delta	Counter	15	45	30	75	20	0.25	1.4E7	Forced
AVA22	FFAW3333	5.84	Delta	Counter	18	54	36	90	20	0.25	1.4E7	Forced
AVA23	FFAW3333	5.84	Delta	Counter	30	90	60	150	20	0.25	1.4E7	Forced
AVA24	FFAW3333	5.84	Delta	Counter	36	108	72	180	20	0.25	1.4E7	Forced
AVA25	FFAW3333	5.84	Delta	Counter	60	180	120	300	20	0.25	1.4E7	Forced
AVA26	FFAW3333	5.84	Delta	Counter	15	45	30	75	20	0.3	1.4E7	Forced
AVA27	FFAW3333	5.84	Delta	Counter	18	54	36	90	20	0.3	1.4E7	Forced
AVA28	FFAW3333	5.84	Delta	Counter	30	90	60	150	20	0.3	1.4E7	Forced
AVA29	FFAW3333	5.84	Delta	Counter	36	108	72	180	20	0.3	1.4E7	Forced
AVA30	FFAW3333	5.84	Delta	Counter	60	180	120	300	20	0.3	1.4E7	Forced
AVA31	FFAW3333	5.84	Delta	Counter	15	45	30	75	20	0.4	1.4E7	Forced
AVA32	FFAW3333	5.84	Delta	Counter	18	54	36	90	20	0.4	1.4E7	Forced
AVA33	FFAW3333	5.84	Delta	Counter	30	90	60	150	20	0.4	1.4E7	Forced
AVA34	FFAW3333	5.84	Delta	Counter	36	108	72	180	20	0.4	1.4E7	Forced
AVA35	FFAW3333	5.84	Delta	Counter	60	180	120	300	20	0.4	1.4E7	Forced
AVA36	FFAW3333	5.84	Delta	Counter	90	270	180	450	20	0.4	1.4E7	Forced
AVA37	FFAW3333	5.84	Delta	Counter	10	30	20	50	15	0.4	1.4E7	Forced
AVA38	FFAW3333	5.84	Delta	Counter	10	20	20	50	20	0.4	1.4E7	Forced
AVA39	FFAW3333	5.84	Delta	Counter	10	30	15	50	20	0.4	1.4E7	Forced
AVA40	FFAW3333	5.84	Delta	Counter	10	30	20	45	20	0.4	1.4E7	Forced
AVA41	FFAW3333	5.84	Delta	Counter	10	30	20	55	20	0.4	1.4E7	Forced
AVA42	FFAW3333	5.84	Delta	Counter	10	30	25	50	20	0.4	1.4E7	Forced
AVA43	FFAW3333	5.84	Delta	Counter	10	30	20	50	25	0.4	1.4E7	Forced
AVA44	DU331	6.06	Delta	Counter	10	30	20	50	15	0.4	1.6E7	Forced
AVA45	DU331	6.06	Delta	Counter	10	20	20	50	20	0.4	1.6E7	Forced
AVA46	DU331	6.06	Delta	Counter	10	30	15	50	20	0.4	1.6E7	Forced
AVA47	DU331	6.06	Delta	Counter	10	30	20	45	20	0.4	1.6E7	Forced
AVA48	DU331	6.06	Delta	Counter	10	30	20	55	20	0.4	1.6E7	Forced
AVA49	DU331	6.06	Delta	Counter	10	30	25	50	20	0.4	1.6E7	Forced
AVA50	DU331	6.06	Delta	Counter	10	30	20	50	25	0.4	1.6E7	Forced

A.4 NTUA (experimental data)

No.	Airfoil model		VG configuration							Flow properties		
	Airfoil	Chord length [m]	Shape	Rotation	height [mm]	length [mm]	Internal distance [mm]	External distance [mm]	Inflow angle [deg]	Position [x/c]	Reynolds number [-]	Transition
NTU01	NTUA18	0.6	Delta	Counter	6	18	22.2	70.2	20	0.2	8.7E5	Forced
NTU02	NTUA18	0.6	Delta	Counter	6	18	22.2	70.2	20	0.3	8.7E5	Forced

B

Influence Closure Relations on Source Term

For XFOIL and RFOIL different empirical relations were found. The reason for this was pointed out to be due to the different closure relations used in both codes. To prove that this is true and to demonstrate that the closure relations are significantly influencing what source term is selected to be the optimal, this appendix is provided.

One of the main difference between XFOIL and RFOIL is within the expression of the shear lag coefficient K_c . K_c controls how much the actual non-equilibrium flow lags behind the idealised concept. In RFOIL, the value of K_c is depending on the shape factor H . This means that K_c is thus varying depending on the boundary-layer state. For the attached flow K_c can be defined by the original Green value, namely 5.6 but for large values of H , in separated turbulent flow, it was found that a better value to adopt would be 3.65. This change is realised by introducing an equation for the shear lag equation. In XFOIL, the shear lag coefficient is assumed to be constant. K_c is kept constant at 5.6 and thus no attention is given to the state of the boundary-layer.⁸⁰

Now, the author believes that the different expressions of this parameter are one of the major reasons why for XFOIL and RFOIL different source term empirical relations are found. A sensitivity analysis will be performed on the K_c parameter by changing the value of K_c in XFOIL to 3.65. Decreasing the K_c value in XFOIL, causes the clean airfoil calculations to modify. In the linear part of the lift curve only minor differences can be recognised. The lift curve of the adapted XFOIL code, has a slightly smaller lift curve slope compared to the original curve. The major difference can be recognised in the stall angle and maximum lift coefficient. The airfoil is stalling earlier and thus consequently a lower maximum lift coefficient is achieved. Also the post-stall behaviour is less gradual compared to the original lift curve. When the drag curves of both codes are compared, similar conclusions can be drawn. Before stall, both drag curves are almost impossible to be distinguished while the new K_c equation causes the airfoil to produce more drag at high angles of attack. The comparison of the lift and drag polar are presented in Figure B.1 and Figure B.2 respectively.

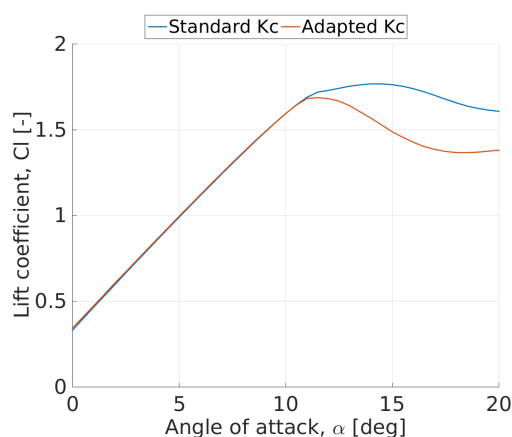


Figure B.1: Lift polar of the DU97W300 airfoil at a Reynolds number of $2E6$ with two different K_c expressions.

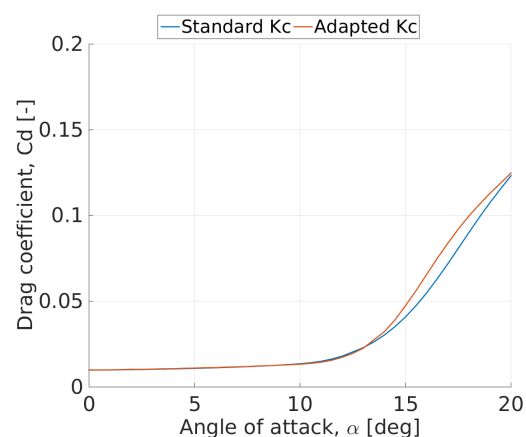


Figure B.2: Drag polar of the DU97W300 airfoil at a Reynolds number of $2E6$ with two different K_c expressions.

Now, one randomly chosen vortex generator case will be analysed in more detail. The particular case has 5mm high vortex generators installed on a DU97W300 airfoil at 20% of the chord. The length to height ratio is 3 and the inflow angle is 12° . The airfoil is put in a flow of Reynolds number $2E6$ and

reference data was obtained during an experimental campaign. For both codes, the standard XFOIL code and the one with modified K_c , the optimal source terms are determined. For every angle of attack individually, that particular source term is selected that is capable to reproduce the measurement data. Note that a correction factor was applied to the measurement data to cope with the lift curve slope difference.

In Figure B.3, the optimal source term integral is plotted against the angle of attack. Only the angles of attack in between clean case stall and VG case stall are considered. The graph consists of two lines: one for the original XFOIL code and one for the adapted code. From this graph, it is clear that the optimal source terms determined per code are different. This means that the expression of K_c significantly influences the source term calibration. Already from this graph, one may understand that XFOIL and RFOIL require different source term definitions.

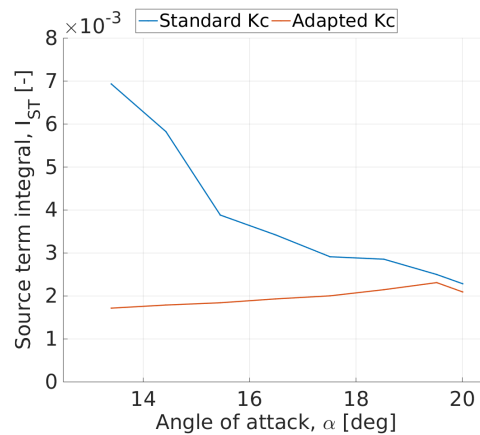
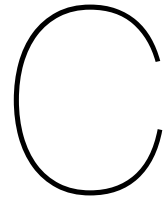


Figure B.3: Optimal source term versus the angle of attack found using XFOIL with two different K_c expressions.

On top of that, one may even recognise that the trend of the source term integral with respect to the angle of attack is now the opposite. For the original XFOIL code, the source term integral decreases with increasing angle of attack. The adapted code finds that the source term integral should increase with the angle of attack. By only adapting one parameter of the closure relations, completely different trends are found. It could thus very easily be that the trend of the source term with respect to the boundary-layer edge velocity and the momentum thickness would also oppose.

This analysis thus shows that the selected set of closure relations has a significant effect and might influence the source term empirical relation to a great extent.



Clean Airfoil Modelling

In this appendix, the lift and drag polar of five different airfoils calculated by XFOIL and RFOIL are compared with reference data. This reference data originates from wind tunnel experiments or from CFD computations. The airfoils of interest are the DU97W300, DU91W2250, DU93W210, DU331 and the FFAW3333.

C.1 DU97W300 Airfoil

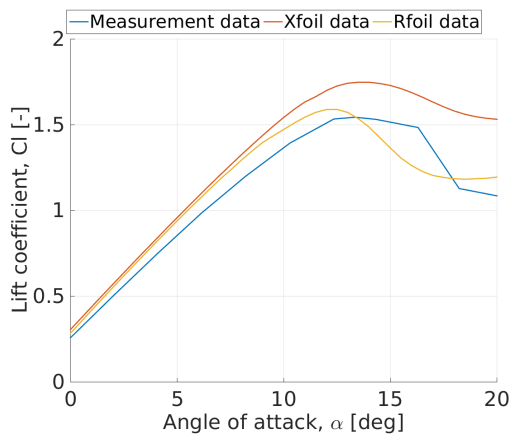


Figure C.1: Lift polar DU97W300 airfoil at $Re = 1E6$.

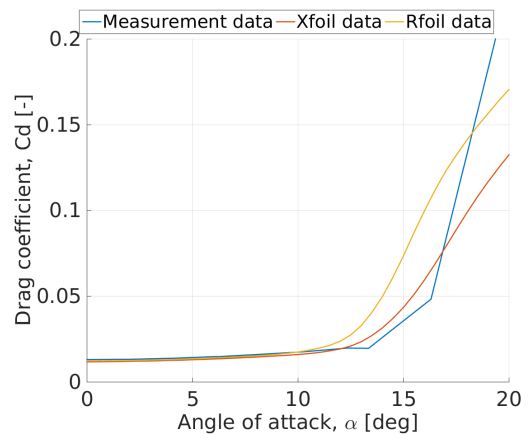


Figure C.2: Drag polar DU97W300 airfoil at $Re = 1E6$.

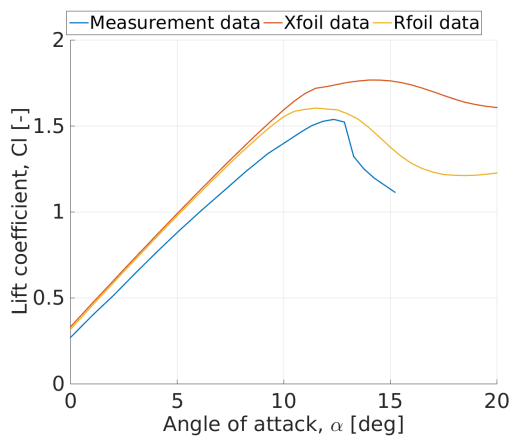


Figure C.3: Lift polar DU97W300 airfoil at $Re = 2E6$.

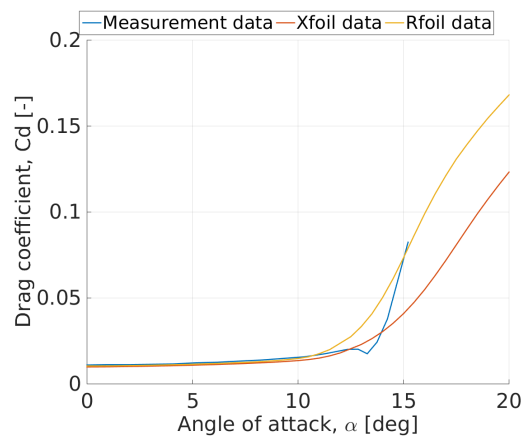
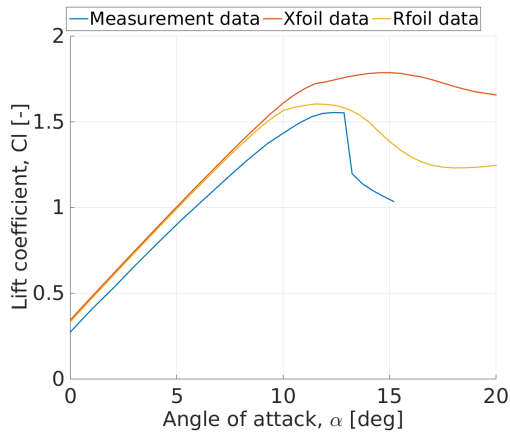
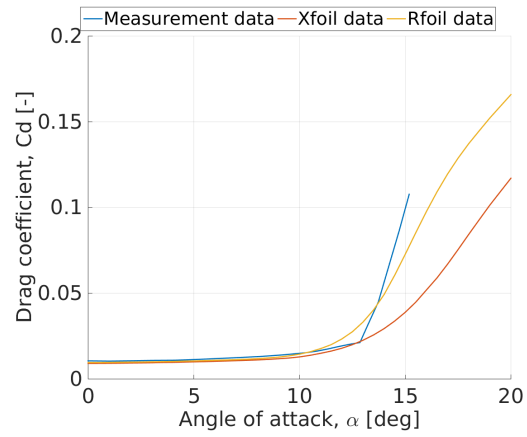
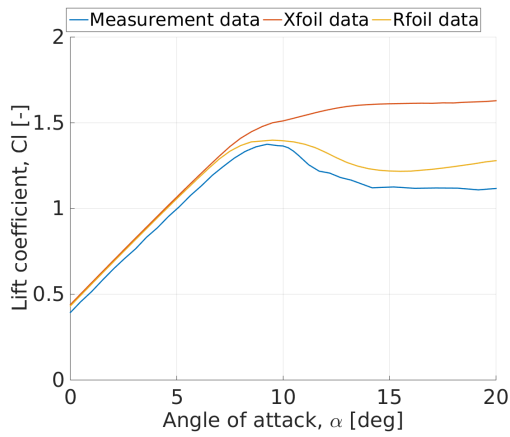
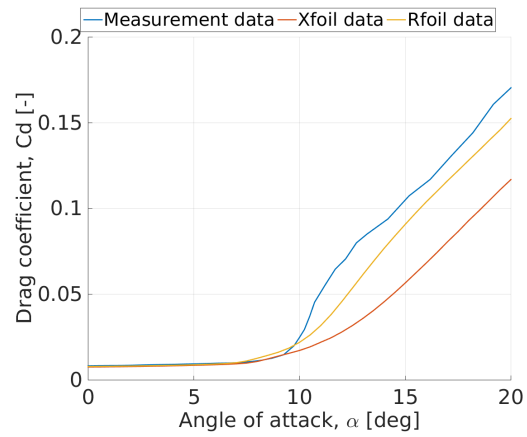


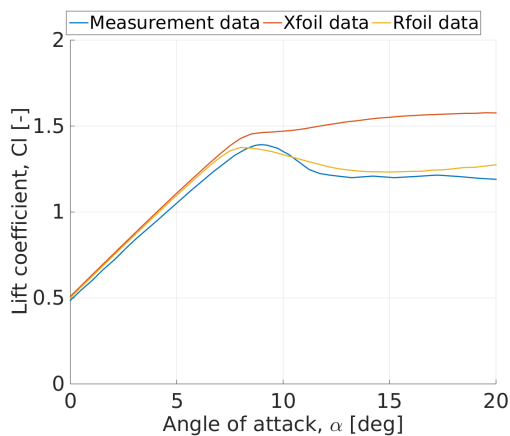
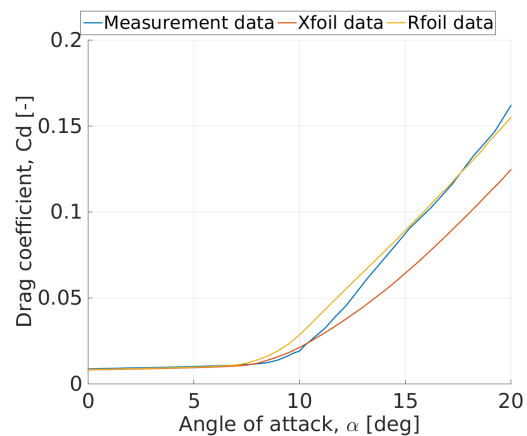
Figure C.4: Drag polar DU97W300 airfoil at $Re = 2E6$.

Figure C.5: Lift polar DU97W300 airfoil at $Re = 3E6$.Figure C.6: Drag polar DU97W300 airfoil at $Re = 3E6$.

C.2 DU91W2250 Airfoil

Figure C.7: Lift polar DU91W2250 airfoil at $Re = 2E6$.Figure C.8: Drag polar DU91W2250 airfoil at $Re = 2E6$.

C.3 DU93W210 Airfoil

Figure C.9: Lift polar DU93W210 airfoil at $Re = 1E6$.Figure C.10: Drag polar DU93W210 airfoil at $Re = 1E6$.

C.4 DU331 Airfoil

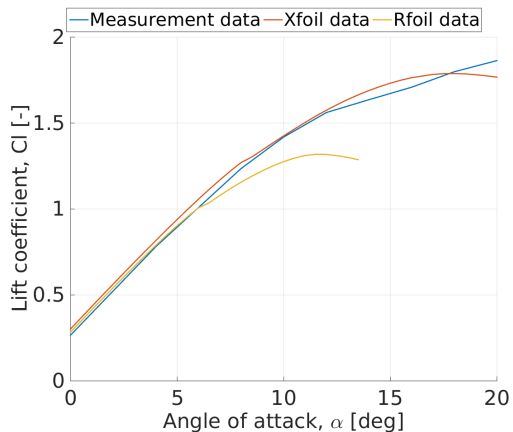


Figure C.11: Lift polar DU331 airfoil at $Re = 15.8E6$.

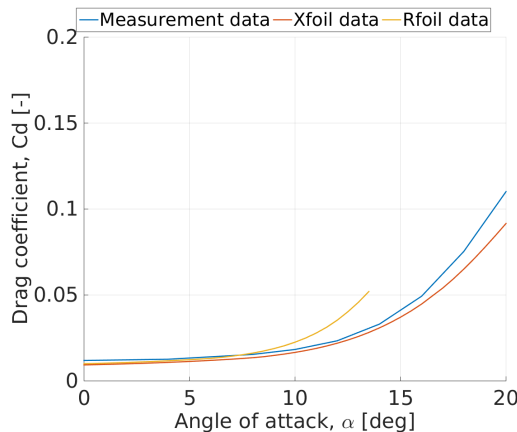


Figure C.12: Drag polar DU331 airfoil at $Re = 15.8E6$.

C.5 FFAW3333 Airfoil

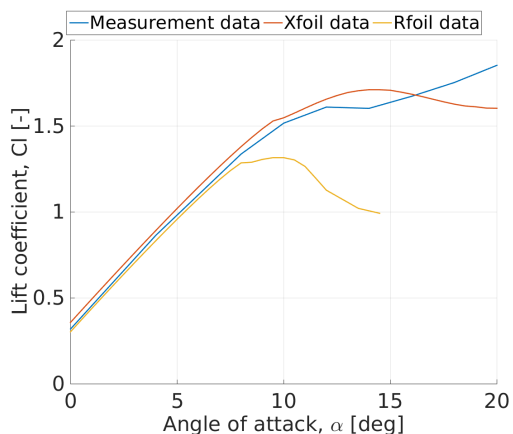


Figure C.13: Lift polar FFAW3333 airfoil at $Re = 14.0E6$.

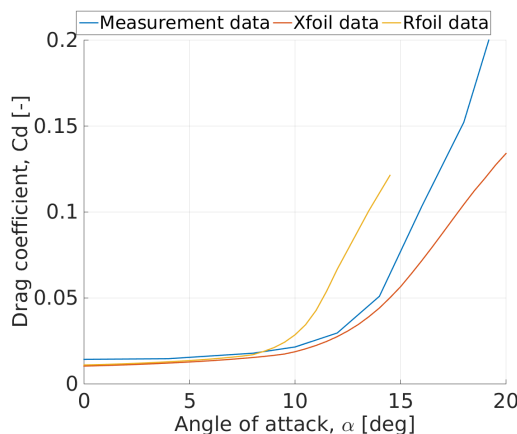


Figure C.14: Drag polar FFAW3333 airfoil at $Re = 14.0E6$.

D

Validation Cases

In this appendix, the validation cases that were already used to set up the source term empirical relation are presented. Figure D.1 and Figure D.2 plot the empirical source term integral versus the optimal source term integral. Per data set, multiple data points are presented referring to different angles of attack. Note that the closer the data points lie to the red line given by $y = x$, the better the prediction will be.

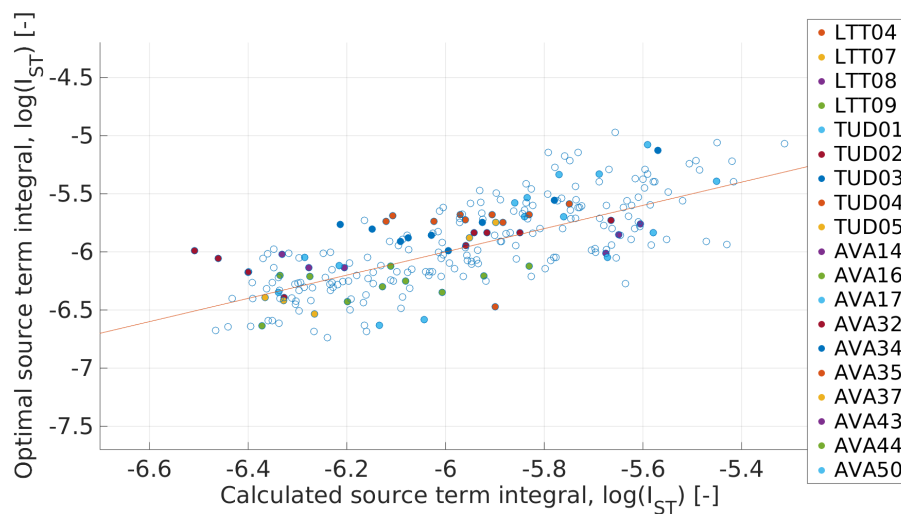


Figure D.1: Empirical source term integral plotted versus the optimal source term integral of XFOIL

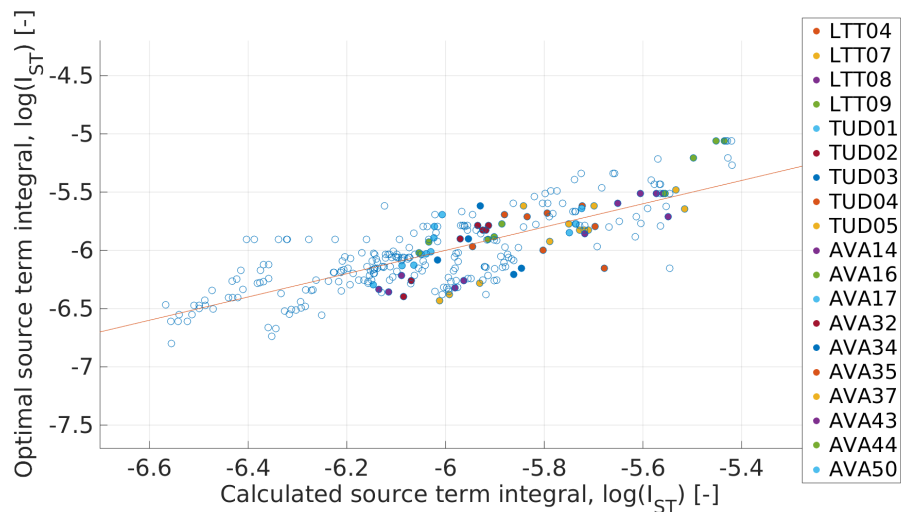


Figure D.2: Empirical source term integral plotted versus the optimal source term integral of RFOIL



Modifications to the Xfoil Code

In this appendix, the modification done into the XFOIL source code will be introduced. All subroutines in which adaptations are made will be listed below. In RFOIL, very similar adaptations are done.⁹³

```
=====
XFOILVG Version 1
Copyright (C) 2000 Mark Drela, Harold Youngren

In this version, vortex generators are incorporated
using a source term approach
Changed by Delphine De Tavernier & Daniel Baldacchino
=====
```

E.1 Subroutine VPAR

The first modification is applied to the *VPAR* subroutine that is described in the *xoper.f* code file. These modification will allow the user to activate the vortex generator option and to input the vortex generator configuration.

```
      SUBROUTINE VPAR
C-----
C      Viscous parameter change menu routine.
C-----
      INCLUDE 'XFOIL.INC'
      INCLUDE 'BLPAR.INC'
      CHARACTER*4 COMAND
      CHARACTER*128 COMARG
      REAL TURB(ISX)

C
      DIMENSION IINPUT(20)
      DIMENSION RINPUT(20)
      LOGICAL ERRORS

C
C ### BEGIN MODIFICATION: add vortex generator in write command
C
10    CONTINUE
      TURB(1) = 100.0 * EXP( -(ACRIT(1) + 8.43)/2.4 )
      TURB(2) = 100.0 * EXP( -(ACRIT(2) + 8.43)/2.4 )
      WRITE(*,1200) XSTRIP(1),
&                  XSTRIP(2),
&                  XVG(1),
&                  XVG(2),
&                  H_VG,
&                  W_VG,
&                  Beta_VG,
&                  ACRIT(1), TURB(1),
&                  ACRIT(2), TURB(2),
&                  VACCEL,
&                  WAKLEN,
&                  SCCON , DUXCON, DLCON,
&                  GACON , GBCON , CTCON,
&                  CTRCON, CTRCEX
1200  FORMAT(
& /' Xtr/c      =', F8.4, '      top      side'
& /' Xtr/c      =', F8.4, '      bottom side'
& /' Xvg/c      =', F8.4, '      top      side'
& /' Xvg/c      =', F8.4, '      bottom side'
& /' HVG/c      =', F8.4,
& /' LVG/HVG    =', F8.4,
& /' Inflow     =', F8.4,
& /' NcritT     =', F8.2, '      (', F6.3, ' % turb. level )'
```

```

& /' NcritB    =', F8.2, '    (' , F6.3, ' % turb. level )'
& /' Vacc     =', F8.4,
& /' WakeL/c  =', F8.3,
& /' Klag     =', F8.4, '    Uxwt  =', F8.2, '    Kdl  =', F8.4
& /' A        =', F8.4, '    B      =', F8.4, '    KCt  =', F8.5
& /' CtniK=, F8.4, '    CtniX=, F8.4 )
C
C ### END MODIFICATION: add vortex generator in write command
C
C=====
C---- start of user interaction loop
  500 CONTINUE
      CALL ASKC('..VPAR^',COMAND,COMARG)
C
      DO I=1, 20
          IINPUT(I) = 0
          RINPUT(I) = 0.0
      ENDDO
      NINPUT = 20
      CALL GETINT(COMARG,IINPUT,NINPUT,ERROR)
      NINPUT = 20
      CALL GETFLT(COMARG,RINPUT,NINPUT,ERROR)
C
C-----
      IF(COMAND.EQ.' ') THEN
          RETURN
C
C-----
C
C ### BEGIN MODIFICATION: add VG as possible option in VPAR
C
      ELSEIF(COMAND.EQ.'? ') THEN
          WRITE(*,1050)
1050  FORMAT(
& /' <cr>      Return to OPER menu'
& /' SHOW      Display viscous parameters'
& /' Xtr rr    Change trip positions Xtr/c'
& /' XVG rr    Include vortex generator'
& /' N        r Change critical amplification exponent Ncrit'
& /' NT       r Change Ncrit on Top'
& /' NB       r Change Ncrit on Bot'
& /' Vacc     r Change Newton solution acceleration parameter'
& /' Wake     r Change wake length/chord'
& /' INIT     BL initialization flag toggle'
& /' LAG      change lag equation constants'
& /' GB       change G-beta constants A,B'
& /' CTR      change initial transition-Ctau constants'
& /' REST     restore BL calibration to baseline')
C
C ### END MODIFICATION: add VG as possible option in VPAR
C
C-----
      ELSEIF(COMAND.EQ.'SHOW') THEN
          GO TO 10
C
C-----
      ELSEIF(COMAND.EQ.'XTR ' .OR.
& COMAND.EQ.'X ') THEN
          IF(LPACC .AND. LVISC) THEN
              WRITE(*,2100)
              GO TO 500
          ENDIF
          IF(NINPUT.GE.2) THEN
              XSTRIP(1) = RINPUT(1)
              XSTRIP(2) = RINPUT(2)
          ELSE
              CALL ASKR('Enter top      side Xtrip/c^',XSTRIP(1))
              CALL ASKR('Enter bottom side Xtrip/c^',XSTRIP(2))
          ENDIF
          LVCONV = .FALSE.
C
C-----
C
C ### BEGIN MODIFICATION: specify required VG inputs
C
      ELSEIF(COMAND.EQ.'XVG ') THEN

```

```

      IF(LPACC .AND. LVISC) THEN
        WRITE(*,2100)
        GO TO 500
      ENDIF
      IF(NINPUT.GE.4) THEN
        XVG(1) = RINPUT(1)
        XVG(2) = RINPUT(2)
        H_VG = RINPUT(3)
        W_VG= RINPUT(4)
        Beta_VG = RINPUT(5)
C
      ELSE
        CALL ASKR('VG suction side XVG/c^',XVG(1))
        CALL ASKR('VG pressure side XVG/c^',XVG(2))
        CALL ASKR('VG height H/c^', H_VG)
        CALL ASKR('VG length L/H^', W_VG)
        CALL ASKR('VG inflow angle deg^', Beta_VG)
C
C ### END MODIFICATION: specify required VG inputs
C
      ENDIF
      LVCONV = .FALSE.
C
C ### BEGIN MODIFICATION: force transition at VG location
C
      IF(XVG(1)<XSTRIP(1)) THEN
        XSTRIP(1) = XVG(1)
      ENDIF
C
      IF(XVG(2)<XSTRIP(2)) THEN
        XSTRIP(2) = XVG(2)
      ENDIF
C
C ### END MODIFICATION: force transition at VG location
C
C-----
REMARK: Part of the code is intentionally removed
C-----
      ELSE
        WRITE(*,1000) COMAND
1000  FORMAT(1X,A4,' command not recognized. Type a "?" for list')
C
      ENDIF
C
      GO TO 500
C-----
2100  FORMAT(/' * Polar is being accumulated.'
&        /' * Cannot change its parameters in midstream.')
      END ! VPAR

```

E.2 Subroutine MRCHDU

The second part of the modification is applied in the subroutine *MRCHDU* specified in the source file *xbl.f*. In this part the code marches over all chordwise positions to compute the boundary-layer properties. This is repeated until convergence is found. At every chordwise position, the source term should be computed. Similar adaptations are done in the *SETBL* and *MRCHUE* subroutine.

```

      SUBROUTINE MRCHDU
C-----
C   Marches the BLs and wake in mixed mode using
C   the current Ue and Hk. The calculated Ue
C   and Hk lie along a line quasi-normal to the
C   natural Ue-Hk characteristic line of the
C   current BL so that the Goldstein or Levy-Lees
C   singularity is never encountered. Continuous
C   checking of transition onset is performed.
C-----
      INCLUDE 'XFOIL.INC'
      INCLUDE 'XBL.INC'
      REAL VTMP(4,5), VZTMP(4)
      REAL MSQ
C

```

```

      DATA DEPS / 5.0E-6 /
C
C---- constant controlling how far Hk is allowed to deviate
C      from the specified value.
      SENSWT = 1000.0
C
      DO 2000 IS = 1, 2
C
      AMCRIT = ACRIT(IS)
C
C---- set forced transition arc length position
      CALL XIFSET(IS)
C
C---- set leading edge pressure gradient parameter  x/u du/dx
      IBL = 2
      XSI = XSSI(IBL,IS)
      UEI = UEDG(IBL,IS)
      BULE = 1.0
C
C---- old transition station
      ITROLD = ITRAN(IS)
C
      TRAN = .FALSE.
      TURB = .FALSE.
      ITRAN(IS) = IBLTE(IS)
C
C ### BEGIN MODIFICATION: initialize source term variables
C
      VGTHET = 0.0
      VGUE = 0.0
      TRZVG = 0.0
      TEMPVG = 0.0
      DECAVVG = 0.0
      STRENGTHVG = 0.0
C
C ### END MODIFICATION: initialize source term variables
C
C---- march downstream
      DO 1000 IBL=2, NBL(IS)
C
C ### BEGIN MODIFICATION: calculate source term integral with empirical relation
C
      iii = IPAN(IBL,IS)

      IF ((X(iii) > XVG(IS)) .AND. (VGTHET.EQ.0)) THEN
C Isolate BL properties at VG location
      VGTHET = THET(IBL,IS)
      VGUE = UEDG(IBL,IS)
      PARVG = W_VG*SIN(Beta_VG/180*3.141592)

C Define empirical parameters
      B_head(1) = -10.0902
      B_head(2) = 0.4945
      B_head(3) = 0.1349
      B_head(4) = -0.6141
      B_head(5) = -1.8937

C Define source term integral
      TRZVG_LOG = B_head(1)
      TRZVG_LOG = TRZVG_LOG + B_head(2)*log(H_VG)
      TRZVG_LOG = TRZVG_LOG + B_head(3)*log(PARVG)
      TRZVG_LOG = TRZVG_LOG + B_head(4)*log(VGTHET)
      TRZVG_LOG = TRZVG_LOG + B_head(5)*log(VGUE)
      TRZVG = EXP(TRZVG_LOG)
C Check for singularity
      IF ((TRZVG.LE.0.0) .OR. (TRZVG_LOG.EQ.0)) THEN
      TRZVG = 0.0
      ENDIF
C Define source term decay
      DECAVVG = 30.0
C Compute source term strength
      DO loc = IBL-1, NBL(IS)-1
      IBLL = IBL-1
C
      IF (loc.EQ.IBLL) THEN
      locA = IPAN(loc,IS)

```

```

        PARTA = 0.0
        ELSE
            locA = IPAN(loc,IS)
            PARTA = EXP(-DECAYVG*(X(locA)-XVG(IS)))*(X(locA)-XVG(IS))
        ENDIF
        locB = IPAN(loc+1,IS)
        PARTB = EXP(-DECAYVG*(X(locB)-XVG(IS)))*(X(locB)-XVG(IS))
        TEMPVG = TEMPVG+(PARTA+PARTB)*(X(locB)-X(locA))
    ENDDO
C
        STRENGTHVG = TRZVG*EXP(-1.0)*2.0/(DECAYVG*TEMPVG)
        STRENGTHVG = nint(STRENGTHVG*100000.0)*1E-5
    ENDIF
C
C ### END MODIFICATION: calculate source term strength and decay
C
C ### BEGIN MODIFICATION: calculate source term value at x location
C
C Compute value of the source term at x position
    IF (X(iii) > XVG(IS)) THEN
        XL = X(iii)-XVG(IS)
        SOURCEVG = STRENGTHVG/(EXP(-1.0)*1.0/DECAYVG)
        SOURCEVG = SOURCEVG*EXP(-DECAYVG*XL)*XL
    ELSE
        SOURCEVG = 0.0
    ENDIF
C Save source term for x position
    SVG(IBL,IS) = SOURCEVG
C
C ### END MODIFICATION: calculate source term value at x location
C
C-----
REMARK: Part of the code is intentionally removed
C-----
C
1000 CONTINUE
C
2000 CONTINUE
C
    RETURN
    END

```

E.3 Subroutine BLVAR

In the subroutine *BLVAR* prescribed in the *xbl.f* code file, the equilibrium shear stress coefficient is defined. The additional source term is added to this equation.

```

SUBROUTINE BLVAR(ITYP)
C-----
C   Calculates all secondary "2" variables from
C   the primary "2" variables X2, U2, T2, D2, S2.
C   Also calculates the sensitivities of the
C   secondary variables wrt the primary variables.
C
C   ITYP = 1 : laminar
C   ITYP = 2 : turbulent
C   ITYP = 3 : turbulent wake
C-----
    IMPLICIT REAL(M)
    INCLUDE 'XBL.INC'
C
    IF(ITYP.EQ.3) HK2 = MAX(HK2,1.00005)
    IF(ITYP.NE.3) HK2 = MAX(HK2,1.05000)
C
C---- density thickness shape parameter      ( H** )
    CALL HCT( HK2, M2, HC2, HC2_HK2, HC2_M2 )
    HC2_U2 = HC2_HK2*HK2_U2 + HC2_M2*M2_U2
    HC2_T2 = HC2_HK2*HK2_T2
    HC2_D2 = HC2_HK2*HK2_D2
    HC2_MS = HC2_HK2*HK2_MS + HC2_M2*M2_MS
C
C---- set KE thickness shape parameter from H - H* correlations

```

```

      IF(ITYP.EQ.1) THEN
        CALL HSL( HK2, RT2, M2, HS2, HS2_HK2, HS2_RT2, HS2_M2 )
      ELSE
        CALL HST( HK2, RT2, M2, HS2, HS2_HK2, HS2_RT2, HS2_M2 )
      ENDIF
C
      HS2_U2 = HS2_HK2*HK2_U2 + HS2_RT2*RT2_U2 + HS2_M2*M2_U2
      HS2_T2 = HS2_HK2*HK2_T2 + HS2_RT2*RT2_T2
      HS2_D2 = HS2_HK2*HK2_D2
      HS2_MS = HS2_HK2*HK2_MS + HS2_RT2*RT2_MS + HS2_M2*M2_MS
      HS2_RE = HS2_RT2*RT2_RE
C
C---- normalized slip velocity Us
      US2 = 0.5*HS2*( 1.0 - (HK2-1.0)/(GBCON*H2) )
      US2_HS2 = 0.5 * ( 1.0 - (HK2-1.0)/(GBCON*H2) )
      US2_HK2 = 0.5*HS2*( - 1.0 / (GBCON*H2) )
      US2_H2 = 0.5*HS2* (HK2-1.0)/(GBCON*H2**2)
C
      US2_U2 = US2_HS2*HS2_U2 + US2_HK2*HK2_U2
      US2_T2 = US2_HS2*HS2_T2 + US2_HK2*HK2_T2 + US2_H2*H2_T2
      US2_D2 = US2_HS2*HS2_D2 + US2_HK2*HK2_D2 + US2_H2*H2_D2
      US2_MS = US2_HS2*HS2_MS + US2_HK2*HK2_MS
      US2_RE = US2_HS2*HS2_RE
C
      IF(ITYP.LE.2 .AND. US2.GT.0.95) THEN
        US2 = 0.98
        US2_U2 = 0.
        US2_T2 = 0.
        US2_D2 = 0.
        US2_MS = 0.
        US2_RE = 0.
      ENDIF
C
      IF(ITYP.EQ.3 .AND. US2.GT.0.99995) THEN
        US2 = 0.99995
        US2_U2 = 0.
        US2_T2 = 0.
        US2_D2 = 0.
        US2_MS = 0.
        US2_RE = 0.
      ENDIF
C
C---- equilibrium wake layer shear coefficient (Ctau)EQ ** 1/2
C ... NEW 12 Oct 94
      GCC = 0.0
      HKC = HK2 - 1.0
      HKC_HK2 = 1.0
      HKC_RT2 = 0.0
      IF(ITYP.EQ.2) THEN
        GCC = GCCON
        HKC = HK2 - 1.0 - GCC/RT2
        HKC_HK2 = 1.0
        HKC_RT2 = GCC/RT2**2
        IF(HKC .LT. 0.01) THEN
          HKC = 0.01
          HKC_HK2 = 0.0
          HKC_RT2 = 0.0
        ENDIF
      ENDIF
C
C ### BEGIN MODIFICATION: add source term to equilibrium shear stress coefficient
C
      HKB = HK2 - 1.0
      USB = 1.0 - US2
      CQ2 =
&      SQRT( CTCON*HS2*HKB*HKC**2 / (USB*H2*HK2**2) ) + SOURCEVG
      CQ2_HS2 = CTCON *HKB*HKC**2 / (USB*H2*HK2**2) * 0.5/CQ2
      CQ2_US2 = CTCON*HS2*HKB*HKC**2 / (USB*H2*HK2**2) / USB * 0.5/CQ2
      CQ2_HK2 = CTCON*HS2 *HKC**2 / (USB*H2*HK2**2) * 0.5/CQ2
&      - CTCON*HS2*HKB*HKC**2 / (USB*H2*HK2**3) * 2.0 * 0.5/CQ2
&      + CTCON*HS2*HKB*HKC / (USB*H2*HK2**2) * 2.0 * 0.5/CQ2
&      *HKC_HK2
      CQ2_RT2 = CTCON*HS2*HKB*HKC / (USB*H2*HK2**2) * 2.0 * 0.5/CQ2
&      *HKC_RT2
      CQ2_H2 = -CTCON*HS2*HKB*HKC**2 / (USB*H2*HK2**2) / H2 * 0.5/CQ2
C

```

```
CQ2_U2 = CQ2_HS2*HS2_U2 + CQ2_US2*US2_U2 + CQ2_HK2*HK2_U2
CQ2_T2 = CQ2_HS2*HS2_T2 + CQ2_US2*US2_T2 + CQ2_HK2*HK2_T2
CQ2_D2 = CQ2_HS2*HS2_D2 + CQ2_US2*US2_D2 + CQ2_HK2*HK2_D2
CQ2_MS = CQ2_HS2*HS2_MS + CQ2_US2*US2_MS + CQ2_HK2*HK2_MS
CQ2_RE = CQ2_HS2*HS2_RE + CQ2_US2*US2_RE

C
CQ2_U2 = CQ2_U2 + CQ2_RT2*RT2_U2
CQ2_T2 = CQ2_T2 + CQ2_H2*H2_T2 + CQ2_RT2*RT2_T2
CQ2_D2 = CQ2_D2 + CQ2_H2*H2_D2
CQ2_MS = CQ2_MS + CQ2_RT2*RT2_MS
CQ2_RE = CQ2_RE + CQ2_RT2*RT2_RE

C
C ### END MODIFICATION: add source term to equilibrium shear stress coefficient
C
C-----

REMARK: Part of the code is intentionally removed

C-----

RETURN
END
```


Bibliography

- [1] KERHO, M., AND KRAMER, B. Enhanced airfoil design incorporating boundary layer mixing devices. *American Institute of Aeronautics and Astronautics*, AIAA-2003-0211 (January 2003).
- [2] ASHILL, P., FULKER, J., AND HACKETT, K. A review of recent developments in flow control. *The Aeronautical Journal*, 2977 (May 2005).
- [3] SCOTT, J. Nacelle vortex generator, December 2005. Figure based on this source, <http://www.aerospaceweb.org/question/aerodynamics/q0255.shtml> [Accessed on 29.02.2016].
- [4] KERHO, M., HUTCHERSON, S., BLACKWELDER, R., AND LIEBECK, R. Vortex generators used to control laminar separation bubbles. *Journal of Aircraft* 30, 3 (May 1993).
- [5] LIN, J. C. Review of research on low-profile vortex generators to control boundary-layer separation. *Progress in Aerospace Sciences* 38 (February 2002), 389–420.
- [6] PEARCEY, H. *Boundary layer and flow control: its principles and application*, vol. 2. Pergamon Press, 1961. Shock-induced separation and its prevention by design and boundary layer control.
- [7] BALDACCHINO, D., RAGNI, D., FERREIRA, C. S., AND VAN BUSSEL, G. J. Towards integral boundary layer modelling of vane-type vortex generators. *American Institute of Aeronautics and Astronautics*, AIAA-2015-3345 (June 2015). 45th AIAA Fluid Dynamics Conference.
- [8] BOOKER, C., ZHANG, X., AND CHERNYSHENKO, S. Large-scale vortex generation modeling. *Journal of FLuids Engineering* 133, 121201-1 (December 2011).
- [9] BANKS, C. Boundary layer parameters, 1999. Figure based on this source, <http://aerofluid.com/papers/b1/node1.html> [Accessed on 29.02.2016].
- [10] VOS, R., AND FAROKHI, S. *Introduction to transonic aerodynamics*, vol. 110 of *Fluid mechanics and its application*. Springer, 2015. Chapter 6.
- [11] WHITE, F. M. *Viscous fluid flows*, third ed. Mc Graw Hill, 2006. Chapter 4, Chapter 6.
- [12] DRELA, M. *Flight vehicle aerodynamics*. The MIT Press, 2014. Chapter 4.
- [13] DRELA, M., AND GILES, M. B. Viscous-inviscid analysis of transonic and low reynolds number airfoils. *American Institute of Aeronautics and Astronautics* 25, 10 (July 1986).
- [14] VELDHUIS, L. Manual for low speed windtunnel test ae2130-ii. Tech. rep., Delft University of Technology, October 2015.
- [15] GAD-EL-HAK, M. *Flow control: passive, active, and reactive flow management*. Cambridge University Press, 2000. Chapter 1, Chapter 8.
- [16] JOSLIN, R. D., AND MILLER, D. N. *Fundamentals and applications of modern flow control, progress in astronautics and aeronautics*, vol. 231. American Institute of Aeronautics and Astronautics, 2009. Chapter 1.
- [17] BETZ, A. *History of boundary-layer control in German*, vol. 2 of *Boundary layer and flow control*. Pergamon Press, 1961.
- [18] ACKERET, J., BETZ, A., AND SCHRENK, O. Experiments with an airfoil from which the boundary-layer is removed by suction. *National Advisory Committee for Aeronautics* (August 1926). NACA-TM-374.
- [19] SCHRENK, O. Tragfluegel mit grenzschichtabsaugung. *Luftfahrtforschung* 2 (1928), 49.
- [20] SCHRENK, O. Versuche an einim absaugflugeln. *Z. Flugtech. Motorlufts* 22 (1931), 259.
- [21] COLE, H., AND HOLLEMAN, E. Measured and predicted dynamic response characteristics of a flexible airplane to elevator control over a frequency range including three structural modes. *NACA*, TN-4147 (1958).
- [22] MCFADDEN, N. M., RATHERT, G. A., AND BRAY, R. S. The effectiveness of wing vortex generators in improving maneuvering characteristics of a swept wing airplane at transonic speeds. *NACA*, TN-3523 (1955).
- [23] LIEBECK, R. On the design of subsonic airfoils for high lift. *American Institute of Aeronautics and Astronautics* 76, 406 (1976).
- [24] CLARK, R. Evaluation of f-111 weapon bay aero-acoustic and weapon separation improvement techniques. *AFFDL*, TR-79-3003 (1979).
- [25] BECHERT, D. W., BRUSE, M., HAGE, W., VAN DER HOEVEN, J. G. T., AND HOPPE, G. Experiments on drag-reducing surfaces and their optimization with an adjustable geometry. *Journal of Fluid Mechanics* 338 (1997), 59–88.
- [26] MASKELL, E. Flow separation in three dimensions. *RAE Report*, Aero 2565 (1955).
- [27] LIGHTHILL, M. *Laminar boundary layers*, vol. 2. Clarendon Press, 1963. Chapter 2.

- [28] HUNG, C. M. Computation of navier-stokes equations for three-dimensional flow separation. *NASA Technical memorandum 102266* (December 1989).
- [29] CHANG, P. K. *Separation of flow*. Pergamon Press, 1970. Chapter 2.
- [30] ELSENAAR, A. Vortex formation and flow separation: The beauty and the beast in aerodynamics. Tech. rep., Nationaal Lucht- en Ruimtevaartlaboratorium, August 2000.
- [31] TAYLOR, H. The elimination of diffuser separation by vortex generators. Tech. rep., United Aircraft Corporation, June 1947.
- [32] SCHUBAUER, G., AND SPANGENBERG, W. Forced mixing in boundary layers. *Journal of Fluid Mechanics* 8, 1 (September 1959), 10–32.
- [33] MANOLESOS, M., AND VOUTSINAS, S. G. Experimental investigation of the flow past passive vortex generators on an airfoil experiencing three-dimensional separation. *Journal of Wind Engineering and Industrial Aerodynamics* 142 (July 2015), 130–148.
- [34] RAO, D., AND KARIYA, T. Boundary-layer submerged vortex generators for separation control – an exploratory study. *First National Fluid Dynamics Congress AIAA* (1988), 839–846.
- [35] PAULEY, W., AND EATON, J. Experimental study of the development of longitudinal vortex pairs embedded in a turbulent boundary layer. *American Institute of Aeronautics and Astronautics* 26, 7 (1988), 816–823.
- [36] TAYLOR, H. Summary report on vortex generators. Tech. rep., United Aircraft Corporation, 1950.
- [37] LIN, J. Review of research on low-profile vortex generators to control boundary-layer separation. *Progress Aerospace Science* 38, 4-5 (2002), 389–420.
- [38] WENDT, B. Parametric study of vortices shed from airfoil vortex generators. *American Institute of Aeronautics and Astronautics* 42, 11 (2004), 2185–2195.
- [39] HANSEN, M., VELTE, C., OYE, S., AND ET AL. Aerodynamically shaped vortex generators. *Wind Energy* 19, 3 (March 2015), 563–567.
- [40] NIKOLAOU, I., AND POLITIS, E. Modelling the flow around airfoils equipped with vortex generators using a modified 2d navier-stokes solver. *Journal of Solar Energy Engineering* 127, 223 (May 2005).
- [41] WENDT, B., AND REICHERT, B. The modelling of symmetric airfoil vortex generators. *American Institute of Aeronautics and Astronautics* (January 1996). 34th Aerospace Sciences Meeting and Exhibit.
- [42] PRANDTL, L. Applications of modern hydrodynamics to aeronautics. Tech. rep., Gottingen University, 1921.
- [43] ASHILL, P., FULKER, L., AND HACKETT, K. Research at dera on sub-boundary layer vortex generators (sbvgs). *American Institute of Aeronautics and Astronautics*, AIAA-2001-0887 (January 2001). 39th Aerospace Sciences Meeting and Exhibit.
- [44] ANGELE, K., AND MUHAMMAD-KLINGMANN, B. The effect of streamwise vortices on the turbulence structure of a separating boundary layer. *European Journal of Mechanics* 24 (2005), 539–554.
- [45] TRANSONIC DATA MEMORANDUM, E. Vortex generators for control of shock-induced separation, part 1 introduction and aerodynamics, 1993.
- [46] JIRASEK, A. Vortex generator model and its application to flow control. *Journal of Aircraft* 42, 6 (November 2005).
- [47] VON STILLFRIED, F., WALLIN, S., AND JOHANSSON, A. V. Evaluation of a vortex generator model in adverse pressure gradient boundary layers. *American Institute of Aeronautics and Astronautics* 49, 5 (May 2011).
- [48] BENDER, E., ANDERSON, B., AND YAGLE, P. Vortex generator modelling for navier-stokes codes. *American Society of Mechanical Engineers*, FEDSM 99-6919 (July 1999).
- [49] JIRASEK, A. A modified vortex generator model and its application to complex aerodynamic flows. *Swedish Defence Research Agency Division of Aeronautics* (2004).
- [50] LEI, Z., KE, Y., JIANZHONG, X., AND MINGMING, Z. Modeling of delta-wing type vortex generators. *Science China Technological Sciences* 54, 2 (February 2011), 277–285.
- [51] TORNBLOM, O., AND JOHANSSON, A. V. A reynolds stress closure description of separation control with vortex generators in a plane asymmetric diffuser. *AIP Physics of Fluids* 19, 11 (November 2007).
- [52] VON STILLFRIED, F. *Computational fluid-dynamics investigations of vortex generators for flow-separation control*. PhD thesis, KTH Royal Institute of Technology, May 2012.
- [53] SMITH, F. Theoretical prediction and design for vortex generators in turbulent boundary layers. *Journal of Fluid Mechanics* 270 (1994), 91–131.
- [54] MERCHANT, A. Design and analysis of supercritical airfoils with boundary layer suction. Master's thesis, Massachusetts Institute of Technology, May 1996.
- [55] FERREIRA, C. Implementation of boundary layer suction in xfoil and application of suction powered by solar cells at high performance sailplanes. Master's thesis, Delft University of Technology, 2002.

- [56] DE OLIVEIRA, G. A novel approach to wind turbine airfoil design with boundary layer suction. Master's thesis, Delft University of Technology, 2011.
- [57] DE OLIVEIRA, G., PEREIRA, R., RAGNI, D., AND KOTSONIS, M. Modeling dbd plasma actuators in integral boundary layer formulation for application in panel methods. *American Institute of Aeronautics and Astronautics*, AIAA-2015-3367 (June 2015). 46th AIAA Plasmadynamics and Lasers Conference.
- [58] SCHLICHTING, H. *Boundary-layer theory*, seventh ed. Mc Graw Hill, 1979. Chapter 1, Chapter 2.
- [59] ANDERSON, J. D. *Fundamentals of aerodynamics*, third ed. Mc Graw Hill, 2001. Chapter 15.
- [60] ANDERSON, J. D. Ludwig prandtl's boundary layer. *Physics Today* (December 2005).
- [61] RESHOTKO, E. Boundary layer stability and transition. *Clearinghouse*, AFOSR 69-2330TR (July 1969). Conference on Boundary Layer Concepts in Fluid Mechanics.
- [62] KUMAR, V. *Separation control in adverse pressure gradients using high-speed microjets*. PhD thesis, Florida State University, 2008.
- [63] HOLM, R., AND GUSTAVSSON, J. A piv study of separated flow around a 2d airfoil at high angles of attack in a low speed wind tunnel. Tech. rep., The Aeronautical Research Institute of Sweden, 1999.
- [64] SUBBARAO, P. Convection in flat plate boundary layers. Lecture Slides, IIT Delhi, Mechanical Engineering Department, December 2007. web.iitd.ac.in/~pmvs/courses/me1242/me1242-24.ppt [Accessed on 29.02.2016].
- [65] CEBECI, T., MOSINSKIS, G., AND SMITH, A. Calculation of separation points in incompressible turbulent flows. *J. Aircraft* 9, 9 (September 1972), 618–624.
- [66] BLASIUS, H. Grenzschichten in flussigkeiten mit kleiner reibung. *Z. Angew Math Phys* 56 (1908), 1–37. English translation in NACA Technical Memo 1256.
- [67] LENGANI, D., SIMONI, D., UBALDI, M., ZUNINO, P., AND BERTINI, F. Turbulent boundary layer separation control and loss evaluation of low profile vortex generators. *Experimental Thermal and Fluid Science* 35 (June 2011), 1505–1513.
- [68] ANDERSON, J. D., DEGROOTE, J., DEGREGZ, G., AND ET AL. *Computational fluid dynamics, A von Karman Institute Book*, third ed. Springer, 2009. Chapter 8.
- [69] CEBECI, T., AND COUSTEIX, J. *Modeling and computation of boundary-layer flows*, second ed. Springer, 2005. Chapter 3, Chapter 4.
- [70] KUNDU, P. K., COHEN, I. M., AND DOWLING, D. R. *Fluid mechanics*, fifth ed. Elsevier, 2012. Chapter 12.
- [71] DRELA, M. *Xfoil: An analysis and design system for low Reynolds number airfoils*, vol. 54 of *Lecture Notes in Engineering*. Springer, June 1989. Low Reynolds Number Aerodynamics: Proceedings of the Conference.
- [72] DRELA, M., AND YOUNGREN, H. Xfoil 6.9 user primer, May 2001. http://web.mit.edu/drela/Public/web/xfoil/xfoil_doc.txt [Accessed on 29.02.2016].
- [73] GARREL, A. V. Integral boundary layer methods for wind turbine aerodynamics. *ECN ECN-C-04-004* (December 2003).
- [74] BALLEUR, J. L. Strong matching method for computing transonic viscous flows including wakes and separations. *La Recherche Aeronautique* 3 (1981), 21–45. English Edition.
- [75] WHITFIELD, D., SWAFFORD, T., AND JACOCK, J. Calculation of turbulent boundary layers with separation and viscous-inviscid interaction. *American Institute of Aeronautics and Astronautics* 19, 10 (October 1981), 1315–1322.
- [76] SMITH, A., AND GAMBERONI, N. Transition, pressure gradient, and stability theory. *Douglas Aircraft Co.*, ES 26388 (1956).
- [77] STURDZA, P. *An aerodynamic design method for supersonic natural laminar flow aircraft*. PhD thesis, Stanford University, December 2003.
- [78] DRELA, M., GILES, M., AND THOMPSON, W. Newton solution of coupled euler and boundary layer equations. *Presented at the Third Symposium on Numerical and Physical Aspects of Aerodynamic Flows* (January 1985).
- [79] DRELA, M. *Two-dimensional transonic aerodynamic design and analysis using the Euler equations*. PhD thesis, Massachusetts Institute of Technology, December 1985.
- [80] VAN ROOIJ, R. Modification of the boundary layer calculation in rfoil for improved airfoil stall prediction. Tech. rep., Delft University of Technology, September 1996.
- [81] BRADSHAW, P., AND FERRISS, D. Calculation of boundary-layer development using the turbulent energy equation: compressible flow on adiabatic walls. *Journal of Fluid Mechanics* 46, 1 (1970), 83–110.
- [82] CLAUSER, F. Turbulent boundary layers in adverse pressure gradients. *Journal of Aeronautical Sciences* 21 (February 1954), 91–108.
- [83] LIBBY, P. A. *An introduction to turbulence*. Taylor and Francis, 1996.
- [84] TIMMER, W. Low turbulence tunnel (ls1). <http://www.lr.tudelft.nl/organisatie/afdelingen/aerodynamics-wind-energy-flight-performance-and-propulsion/facilities/wind-tunnel-lab/low-turbulence-tunnel-ls1/> [Accessed on 28.07.2016].

- [85] TIMMER, W., AND VAN ROOIJ, R. Summary of the delft university wind turbine dedicated airfoils. *American Society of Mechanical Engineers* 125 (November 2003).
- [86] SCHEPERS, G. Avatar: Advanced aerodynamic tools for large rotors. <http://www.eera-avatar.eu/home/> [Accessed on 27.09.2016].
- [87] SØRENSEN, N. N. Ellipsys2d/3d, March 2015. <http://www.the-numerical-wind-tunnel.dtu.dk/EllipSys> [Accessed on 18.08.2016].
- [88] MANOLESOS, M. *Experimental and computational study of three-dimensional separation and its control using passive vortex generators*. PhD thesis, National Technical University of Athens, September 2013.
- [89] BROWN, S. H. Multiple linear regression analysis: a matrix approach with MATLAB. *Alabama Journal of Mathematics* (Spring/Fall 2009).
- [90] HEIJ, C., DE BOER, P., FRANSES, P. H., KLOEK, T., AND VAN DIJK, H. K. *Econometric methods with applications in business and economics*. Oxford University Press, 2004. Chapter 3.
- [91] PECHLIVANOGLU, G. *Passive and active flow control solutions for wind turbine blades*. PhD thesis, Technical University of Berlin, February 2012.
- [92] FOUATHI, O., MEDALE, M., IMINE, O., AND IMINE, B. Design optimization of the aerodynamic passive flow control on naca 4415 airfoil using vortex generators. *European Journal of Mechanics B/Fluids* 56 (December 2015), 82–96.
- [93] PROJECTION. Cover picture. <http://www.projection.com/wp-content/uploads/2013/12/windmills.jpg> [Accessed on 01.10.2016].